UNIVERSITY OF CALIFORNIA SAN DIEGO

Control Methods for a Modal Disturbance Experiment with Structured Uncertainty

A Thesis submitted in partial satisfaction of the requirements
for the degree Master of Science

in

Engineering Sciences (Mechanical Engineering)

by

Michael Callahan

Committee in charge:

Professor Thomas Bewley, Chair
Professor Raymond de Callafon
Professor Maurício de Oliveira

2019

The Thesis of Michael Callahan as it is listed on UC San Diego Academic Records is approved, and it is acceptable in quality and form for publication on microfilm and electronically:

_____

_____

_____
Chair

University of California, San Diego

2019

DEDICATION

To my family and my friends.

TABLE OF CONTENTS

Signature Page . . . iii

Dedication . . . iv

Table of Contents . . . v

List of Figures . . . vii

List of Tables . . . x

Acknowledgements . . . xi

Abstract . . . xii
Abbreviations . . . 1
Nomenclature . . . 1

Chapter 1 Introduction . . . 2
1.1 Motivation . . . 2
1.2 Background . . . 4
1.3 A Primer on the Simulated Flight Dynamics of System . . . 7

Chapter 2 Experimental Setup and Design Environment . . . 11
2.1 Experimental Setup . . . 11
2.1.1 Data Acquisition . . . 12
2.1.2 Linear Actuators . . . 14
2.1.3 Accelerometers . . . 16
2.1.4 Force Sensors . . . 17
2.1.5 Other Hardware . . . 17
2.2 Experimental Testing Procedures . . . 18
2.2.1 Adjusting the Actuators . . . 18
2.2.2 Connecting the DAQ . . . 18
2.2.3 Simulink Realtime Environment . . . 19
2.2.4 System Identification/Parameter Estimation Testing . 20
2.2.5 Control Testing . . . 22
2.3 Simulation and Design Environment . . . 22

Chapter 3 Model . . . 25
3.1 Deriving the State Space Plant Model . . . 25
3.2 Realizing the Model . . . 30
3.2.1 Finite Element Analysis . . . 30
3.2.2 Model Results . . . 33
3.2.3 Analysis of the System Modes/States . . . 33
3.3 Uncertainty Modeling . . . 35
3.3.1 LFT Formulation and Derived Uncertainty Description 39

Chapter 4 Controls . . . 43
4.1 Building the Controller . . . 43
4.2 First Bending Mode Controller Designs . . . 50
4.2.1 Linear-Quadratic-Gaussian . . . 51
4.2.2 Linear Quadratic-Gaussian with High Frequency Rolloff 52
4.2.3 Mixed Sensitivity . . . 54
4.3 Other Control Designs . . . 58
4.3.1 Linear-Quadratic Revisited . . . 58
4.3.2 Linear-Quadratic with High Frequency Rolloff Revisited . . . 58
4.3.3 Inverted Nominal Sensitivity Weighting . . . 58
4.3.4 Uncertainty Model H_∞ Minimized Controller . . . 59
4.4 Controllers Compared to Derived Uncertainty Structures . . . 59
4.4.1 Robust Stability . . . 59
4.4.2 Robust Performance . . . 61
4.4.3 Predicted Margins . . . 61

Chapter 5 Results . . . 63
5.1 First Bending Mode Experimental Results . . . 63
5.2 Other Controller Results . . . 66

Chapter 6 Conclusion . . . 68
6.1 Summary . . . 68
6.2 Future Work and Refinements . . . 69

Appendix A Additional Figures . . . 71

Appendix B Additional Tables . . . 96

Appendix C Additional Derivations . . . 101
C.1 Matrix Formulation for Modal Uncertainty Transfer Function 101

Bibliography . . . 104

LIST OF FIGURES

Figure 1.1: Iron Bird test article (left). Iron Bird model (right). 4
Figure 1.2: Modeled pressure induced from angle of attack (left). Modal equivalent point force of angle of attack (right). [6] 7
Figure 1.3: Modeled pressure induced from aileron deflection (left). Modal equivalent point force of aileron deflection (right). [6] 8
Figure 1.4: Section-view free body diagram of system force and acceleration vectors on one wing. 9

Figure 2.1: System Block Diagram. 12
Figure 2.2: Configuration 1 (Upper-Left), 2 (Upper-Right), 3 (Middle-Left), 4 (Middle-Right), 5 (Lower-Left), and 6 (Lower-Right). 13
Figure 2.3: Overview of System. 14
Figure 2.4: Example of Least Squares Fitting Routine on Experimental Data. 15
Figure 2.5: Actuator 1 Calibration Curve (Top Left). Actuator 2 Calibration Curve (Top Right). Actuator 3 Calibration Curve (Bottom Left). Actuator 4 Calibration Curve (Bottom Right). 16
Figure 2.6: Accelerometer Output Drift Test. 17
Figure 2.7: System identification plot of measured compared to simulated for input 1 to output 1. 21
Figure 2.8: Simulink Environment (Top Level). 23
Figure 2.9: Experimental step response (left). Simulation step response (right). 24
Figure 2.10: State error from step response with high process noise covariance (left) and balanced coavariance (right). 24

Figure 3.1: CELAS element constraints located on each foot. 31
Figure 3.2: Iron Bird First Bending Asymmetric Mode FEA Solution. 32
Figure 3.3: Hankel Singular Values. 34
Figure 3.4: Generalized LFT Strucuture. 38
Figure 3.5: Block Diagram Representation of Uncertain Modal System. 38
Figure 3.6: LFT structure with single disturbance. 39
Figure 3.7: Variance in Natural Frequency with Added Mass from Experimental Data. 40
Figure 3.8: Modeled LFT Uncertainty Bode Plot. 41

Figure 4.1: Open Loop System 43
Figure 4.2: Open Loop System State Space 44
Figure 4.3: Closed Loop LQG System. 48
Figure 4.4: Closed Loop LQG System with Washout Filter (G). 49
Figure 4.5: Control Structure with High Frequency Rolloff Filter (R) and Washout Filter (G). 50
Figure 4.6: State error from white noise in measurements during simulation. . 52
Figure 4.7: Bode Response of LQG Controller. 53
Figure 4.8: Bode Response of LQG Controller with High Frequency Rolloff. . 54
Figure 4.9: Mixed Sensitivity Weighted System 55

Figure 4.10: Bode Response of Mixed Sensitivity Controller. 57

Figure 5.1: Ranges of Frequency Responses for LQG, LQG with HF Rolloff, and Mixed Sensitivity Closed Loop Systems as well as Open Loop System. 64
Figure 5.2: Change in Disturbance Gain with Respect to Open Loop System (% change in dB). 65

Figure 6.1: Frequency Response Functions of Experimental Data of Nominal System with Symmetric Sine Burst Input Compared to Model. . . 69

Figure A.1: Data Acquisition Card (Left) [37] [36] and Data Acquisition Card Breakout Board (Right). 71
Figure A.2: Linear Actuator [35]. 71
Figure A.3: Motor Amplifier (Top Left) [9]. External Power Supply (Top Right) [3]. EMI Filter (Bottom) [44]. 72
Figure A.4: Accelerometer with Evaluation Board [2] [1]. 72
Figure A.5: Signal Conditioning Module (Top Left) [39]. Voltage Breakout Unit (Top Right) [22]. Force Gauge (Bottom) [40]. 73
Figure A.6: Power Supply. 73
Figure A.7: PCI 6229 pinout from datasheet [37]. 74
Figure A.8: Simulink Realtime Model. 75
Figure A.9: Simulink Realtime Target Computer Monitor. 76
Figure A.10: Actuator 1 Inverse Calibration Curve (Top Left). Actuator 2 Inverse Calibration Curve (Top Right). Actuator 3 Inverse Calibration Curve (Bottom Left). Actuator 4 Inverse Calibration Curve (Bottom Right). 77
Figure A.11: NX Simulink Results for Nominal Configuration: (Left-to-Right, Up-to-Down) Modes 1, 2, 3, 4, 5, and 6. 78
Figure A.12: NX Simulink Results for Configuration 1: (Left-to-Right, Up-to-Down) Modes 1, 2, 3, 4, 5, and 6. 79
Figure A.13: NX Simulink Results for Configuration 2: (Left-to-Right, Up-to-Down) Modes 1, 2, 3, 4, 5, and 6. 80
Figure A.14: NX Simulink Results for Configuration 3: (Left-to-Right, Up-to-Down) Modes 1, 2, 3, 4, 5, and 6. 81
Figure A.15: NX Simulink Results for Configuration 4: (Left-to-Right, Up-to-Down) Modes 1, 2, 3, 4, 5, and 6. 82
Figure A.16: NX Simulink Results for Configuration 5: (Left-to-Right, Up-to-Down) Modes 1, 2, 3, 4, 5, and 6. 83
Figure A.17: NX Simulink Results for Configuration 6: (Left-to-Right, Up-to-Down) Modes 1, 2, 3, 4, 5, and 6. 84
Figure A.18: LFT structure with r disturbances. 85
Figure A.19: Example of Experimentally Derived Power Spectra. 86
Figure A.20: Variance in Natural Frequency with Added Mass from FEA Model. 86
Figure A.21: Complete Modal Uncertainty Structure Bode Response. 87
Figure A.22: Bode Response of Closed Loop LQG System. 88

Figure A.23: Bode Response of Closed Loop LQG with High Frequency Rolloff System. 88
Figure A.24: Bode Response of Closed Loop Mixed Sensitivity System. 89
Figure A.25: Weighted Sensitivity and Control Sensitivity Functions in Mixed Sensitivity Design. 89
Figure A.26: Bode Response with Inverse Weighting Functions for Mixed Sensitivity Design. 90
Figure A.27: Frequency Response Function from Experimental Data of Nominal System with Symmetric Sine Burst Input with Two Mode Controllers. 90
Figure A.28: Frequency Response Function from Experimental Data of Nominal System with Symmetric Sine Burst Input with Four Mode Controllers. 91
Figure A.29: Frequency Response Functions of Experimental Data of Nominal System with Asymmetric Sine Burst Input Compared to Model. . . 92
Figure A.30: Frequency Response Functions of Experimental Data of Nominal System with White Noise Input Compared to Model. 93
Figure A.31: Alternate Surface View of Disturbance Gain Maps for Each System. 94
Figure A.32: Ranges of Frequency Responses for Closed Loop and Open Loop System (Gain of Displacement). 94
Figure A.33: Alternate Surface View of Disturbance Gain Maps for Each System (Gain of Displacement). 95

LIST OF TABLES

Table 2.1: Experimentally derived natural frequencies per configuration. 22

Table 3.1: Model derived natural frequencies per configuration. 33

Table 4.1: Robust Stability and Robust Performance Comparisons for Controller Designs. 62

Table 5.1: Frequency Weighted H_∞ Norms (dB) for Two Mode Controller Designs (White Noise Results) 66
Table 5.2: Frequency Weighted H_∞ Norms (dB) for Four Mode Controller Designs (White Noise Results, Nominal Only) 67

Table B.1: List of hardware elements 96
Table B.2: DAQ Wiring Pinout 97
Table B.3: R^2 Values for Actuator 1 calibration. Individual fits and averaged fits. 97
Table B.4: R^2 Values for Actuator 2 calibration. Individual fits and averaged fits. 98
Table B.5: R^2 Values for Actuator 3 calibration. Individual fits and averaged fits. 98
Table B.6: R^2 Values for Actuator 4 calibration. Individual fits and averaged fits. 99
Table B.7: Frequency Weighted H_∞ Norms (dB) for Two Mode Controller Designs (Symmetric Sine Burst Results) 99
Table B.8: Frequency Weighted H_∞ Norms (dB) for Two Mode Controller Designs (Asymmetric Sine Burst Results) 99
Table B.9: Frequency Weighted H_∞ Norms (dB) for Four Mode Controller Designs (Symmetric Sine Burst Results, Nominal Only) 99
Table B.10: Frequency Weighted H_∞ Norms (dB) for Four Mode Controller Designs (Asymmetric Sine Burst Results, Nominal Only) 100

ACKNOWLEDGEMENTS

First, I would like to thank Professor Thomas Bewley for his guidance and support in realizing my master's project. I would not have been able to perform the work discussed within this report without the collaborative effort he facilitated between the UCSD Coordinated Robotics Laboratory and ATA Engineering. In addition, I was able to gain valuable information pertaining to model predictive control by taking his optimal estimation course.

On that note, I am extremely thankful to ATA Engineering for the aiding my efforts in this project by allowing me to intern at the company and conduct experimental research on the Iron Bird test article. I thank Mr. Andrew White for his efforts in supporting the Iron Bird project, especially in the hardware design and experimental layout, and Dr. Frank Fan for his invaluable advice pertaining to control theory as well his guidance in keeping on point with regards to project management.

I would like to thank to Dr. Clark Briggs for his guidance on the project and his efforts in developing and directing the project efforts on Iron Bird.

Thank you to the remaining committee members. I thank Professor de Callafon who offered advice in formulating uncertainty structure for robust control on this project and taught both a robust control class and a system identification class. I also thank Professor de Oliveira who offered advice on guiding the research included in this report towards a publication and taught a class on linear control theory with an emphasis on linear matrix inequality formulation.

Thank you to my colleagues in the Coordinated Robotics Laboratory for their advice and suggestions in furthering my research on this project.

Thank you to Professor William McEneaney who had me as an instructional assistant for his numerical methods course and taught an optimal control class which made use of dynamic programming principles.

Thank you to the esteemed faculty within the MAE department at UCSD.

ABSTRACT OF THE THESIS

Control Methods for a Modal Disturbance Experiment with Structured Uncertainty

by

Michael Callahan
Master of Science in Engineering Sciences (Mechanical Engineering)
University of California San Diego, 2019
Professor Thomas Bewley, Chair

The purpose of this thesis is to establish an experimental process by which a structural system may be characterized through modal analysis in an effort to develop and implement disturbance rejection control designs. Throughout this report, a structural test article representing a simplified aircraft model will be the subject of study, referred to as the "Iron Bird." This report discusses how the article was modeled using finite element analysis for the purpose of control design. Then, the report establishes a "dry" wind tunnel testing approach by utilizing readily available testing equipment and hardware as a means of testing aerodynamic control systems as opposed to requiring a wind tunnel facility for the purposes of experimental validation. Reviewing both the experimental setup and design environment, this thesis aims to establish a comprehensive account of how this system was analyzed, designed, and tested. Finally, with the inclusion of plant uncertainty this report analyzes a suite of control design approaches in order to establish methods of implementing more robust controller designs for modal disturbance rejection on this particular system.

Abbreviations

ARE Algebraic Ricatti Equation

CFD Computational Fluid Dynamics

FEA Finite Element Analysis

FEM Finite Element Model

LFT Linear Fractional Transformation

LMI Linear Matrix Inequality

LQE Linear Quadratic Estimator

LQG Linear-Quadratic-Gaussian

LQR Linear Quadratic Regulator

LTI Linear Time-Invariant

MIMO Multi-Input Multi-Output

Nomenclature

A^* The transpose of matrix A

$||\cdot||_\infty$ The $H\infty$ norm of a function

$F(A, \Delta)$ The linear fractional transformation of A with Δ in feedback

$A^\dagger$ The Moore-Penrose Pseudoinverse

Chapter 1

Introduction

We begin by taking a look at the background of robust control, modal analysis, system identification, and methods of aircraft dynamic testing. What we wish to show is the need for a lower cost solution to experimental validation of cutting edge aircraft designs, especially in the unmanned space, as an alternative to expensive wind tunnel tests. In doing so, this study provides one potential methodology for achieving such an alternative for experimental aerodynamic control systems validation.

1.1 Motivation

In regards to modern approaches to dynamic aircraft design validation, there are both simulated and experimental methods. Simulation through finite element analysis FEA and computational fluid dynamics CFD software tools provide powerful frameworks for modeling, analyzing, and validating aircraft models and designs [23] [10]. However, there is no true replacement in this regard to testing physical hardware in an experimental environment. Validating systems, components, designs, and assemblies in unison with flight tests and wind tunnel testing provide a comprehensive and invaluable study in how a real test article will perform in operating environments. This is partially due to the complexity of current and future aerodynamic problems requiring faster and better scalable hardware. In addition, hardware tests will ensure that the reliability and operability of all necessary systems are stressed at once whereas CFD and FEA studies generally confine themselves to individual subsystems [29]. To this end, it has proven useful to complement FEA and CFD methods with true hardware testing in order to provide more complete analysis. This idea of pairing simulation

with hardware validation for design optimization is a key focus of this thesis.

The Iron Bird test article was designed and manufactured by ATA Engineering for demonstrations of modal testing. In this regard, it makes a suitable piece for exploring methods for control of structures and system modes. In the case of structural control for this article, it proves important to obtain a reasonable quantification of uncertainty with regards to modal dynamics in order to obtain a control design which is suitable robust to plant variation, an objective previously explored by Briggs [7]. To this end, FEA methods provide a reasonable starting model for control design. System identification methods may be used in conjunction to establish the parameters left undeveloped within the model through a FEM.

In the field of aeronautics, many active control systems on commercial aircraft involve gust load alleviation for reducing airload stresses and improving operability [17]. When these gust loads excite the natural resonances of the system in a way which produces negative damping within the aeroelastic dynamics, flutter is produced. The phenomenon of flutter and aeroelasticity has been well studied since the mid twentieth century with the most famous example of unsteady airload induced flutter being the Tacoma Narrows Bridge collapse of 1940 [5]. In the case of aircraft, extensive flutter testing is mandatory for modern fighter jets and commercial vehicles, however two fighter jets which experienced stable limit cycle oscillations under heavy loading conditions are the F-16 and the F/A-18 [8]. Experimental research has been conducted on the F/A-18 specifically for the formulation of flutter margins for nominal and robust stability [32]. NASA's X-53 project utilized a converted F/A-18 for demonstration of their active aeroelastic wing project. Research on this specific article has been performed through dynamic modeling techniques of the aeroelastic system [11] and robust control designs for suppressing aeroelastic feedback through techniques like adaptive feedback control [49].

Unmanned aerial vehicle designs are becoming more capable, faster, and higher flying to the point where phenomena such as flutter and robust gust load alleviation techniques must be considered [45] [47] [12]. Active flutter suppression research is being performed on the X-56 due to its flexible wing stucture, opening a radical new possible avenue for future dron designs [43]. While vibration testing methods exist for making flutter predictions before flight test [18], wind-tunnel experimentation remains the natural fit for replicating the aeroelastic dynamics an aircraft will experience during flight. However, costs may run high for continued experimentation. This discourages

competition from any small startups or mid-sized aircraft design companies who may not have the same budget for continued testing. A "dry" wind tunnel testing procedure outlined in this report might allow for an alternative means of testing an aircraft design for aerodynamic performance without the potential expenses or unavailability of a wind tunnel environment. An aim of this particular methodology is towards the realization of a simulated flutter experimental methodology for lower cost testing of unstable aeroelastic conditions with readily available hardware which was initiated by Briggs for this particular Iron Bird application [6].

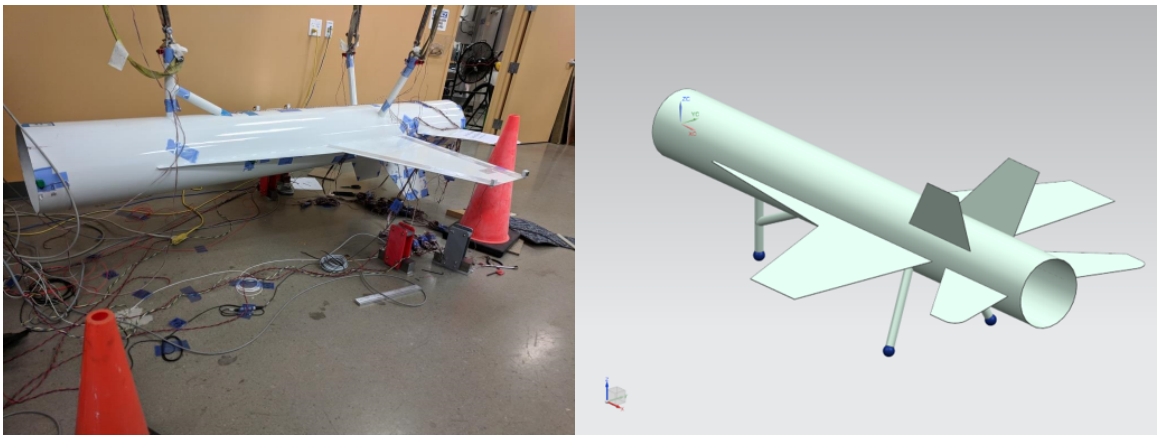

Figure 1.1: Iron Bird test article (left). Iron Bird model (right).

This thesis will not directly tie the Iron Bird test article to a flutter description, however it will utilize knowledge of robust control and uncertainty modeling to show an experimental methodology towards providing robustness in control modeling of this system against simulated periodic gust load disturbances with uncertain airloads.

The presented Iron Bird problem requires analysis of frequency responses of systems, because the performance criterion of interest is the attenuation of modal disturbances which themselves are components of frequency. The system considered in this problem leverages modal frequency based characterization for formulating a state space model. With this in mind, it proves vital to understand the derivation and implementation of standard control theory methods for optimal and robust design.

1.2 Background

Control methods involving multivariable systems have expanded greatly since the early research in what is now commonly referred to the advent of modern controls

during the 1970s. This early research indicated other methods of modeling and controlling systems using linear state space methods. When it comes to modern control theory, the field generally is divided into two separate branches: linear control theory and nonlinear control theory. For the purposes of this thesis, we will construct control models utilizing tools within linear control theory.

Modern control techniques utilize a state space representation to provide controllers leveraging state variable feedback through pole placement, linear quadratic problem formulation, and many more methods for applications usually requiring multi-input multi-output MIMO control. There are numerous pole placement algorithms which have been developed since the 1980s seeking to develop a closed loop system with prescribed dynamics [28] [21]. For the purpose of this thesis, the primary modern control design technique which will be discussed involves the formulation of a linear quadratic regulator LQR and a linear quadratic estimator LQE.

Since the early 1960s, the framing of the optimal estimator and the noise free regulator problems has been leveraged in such a way as to expose the dual nature of the problem structure [27]. This duality framework is especially powerful when paired with the principle of separation of estimation and control stating that the eigenvalues of a system is the union of the closed estimator and closed regulator systems which allows for independent design and optimization [21].

This study goes through a process of formulating a framework for deriving a Linear Quadratic Regulator LQR and Linear Quadratic Estimator LQE control model. Standard LQR control utilizes a regulator obtained by solving the Algebraic Ricatti Equation for a cost function emphasizing either error minimization or control input cost through appropriate covariance matrix assignment.The estimator may be obtained in a similar fashion by employing the concept of duality explored since the 1960s by Kalman [27]. There are numerous methods of deriving the state estimator, thus obtaining a Kalman Filter, this dual form method is the one which this project utilizes.

Modal characterization of systems is particularly useful in relating fundamental frequencies to applied control in a system, due to the linear independence of each mode. Modal analysis has existed in some form since the 1800s, and become modernized in the mid 1900s with the utilization of the fast Fourier transform and advent of computer technology [31]. By creating a state space representation around the system modes, analysis can be done on each state with some degree of linear independence

by construction of the modal coordinate space which lends itself well towards control design.

System identification for control systems has been a developing field since the late 1970s with much ground gained in the late 1980s through the mid 1990s. The theory of system identification allows for the correlation of frequency driven data and structured models, resulting in data-driven models [33]. For this particular problem, we leverage powerful tools and framework unified under Ljung's work for connecting the experimental test article's dynamic response with the framework established through finite element derived model. This thesis discusses how a series of experiments was performed on the test article with a handful of approaches in order to best characterize the system.

Robust control theory has been a topic long researched since the 1940s and modernized closer to the 1980s. The purpose of robust control theory is to reframe the Wiener-Hopf-Kalman optimal control formulation in such a way as to deal with modelling deviations and plant uncertainty [19]. For the purposes of H_∞ control, this problem focuses primarily on the methods of sensitivity minimization following the methodology of Zames [48]. In this problem formulation, a weighting is assigned to find a feedback frequency response which minimizes the H_∞ norm, $||\cdot||_\infty$, of the closed loop matrix output by leveraging state space linear fractional transformation LFT methods to produce disturbance attenuation across a greater degree of plant variance than the optimal case [14] [19]. This is a useful characterization of system performance in this case, because our aim of rejecting modal disturbances will be directly related to reduction in the system H_∞ norm due to the definition of the system's measured response as the linear superposition of all system modes [16].

On the subject of LFTs and uncertainty modeling, it is useful to consider how plant variance will affect each mode parametrically. The framework of developing LFT models allows for control design revolving around bounding structured singular values and determining measures of design, including nominal performance, robust stability, and robust performance [15] [19]. Although the system modes may be expressed independently, uncertainty introduced into the system through mass loading will parametrically affect each one under some common relation which may be linearized. A derived LFT model allows for system uncertainty to be characterized in terms of an uncertainty-driven disturbance signal. This is useful when evaluating the performance and robustness of a particular series of controllers under differing off-

nominal conditions. The end design goal for H_∞ techniques is the minimization of the H_∞ norm of the system response to disturbance inputs.

1.3 A Primer on the Simulated Flight Dynamics of System

The Iron Bird is a steel sheet metal structure approximating the profile of an aircraft. As such, this project focuses primarily on drawing some means of aerodynamic control systems validation and implementation.

With regards to the inputs and outputs of the system, the Iron Bird utilizes two pairs of linear actuators placed at different locations of the wings and four accelerometers as outputs located at the wingtips at both the leading and trailing edges.

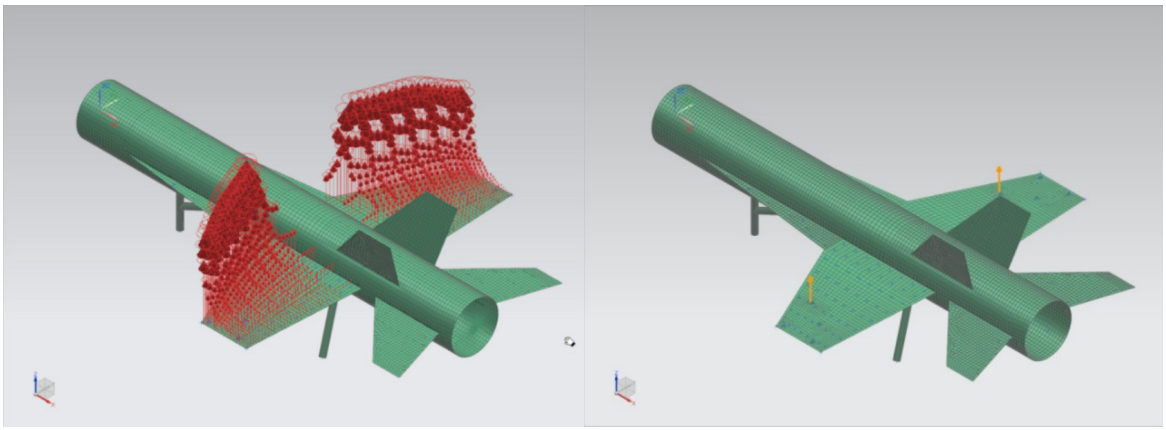

Figure 1.2: Modeled pressure induced from angle of attack (left). Modal equivalent point force of angle of attack (right). [6]

From previous modeling performed on Iron Bird [6], we apply computational fluid dynamics CFD modeling to obtain pressure distribution for shifting the angle of attack of the aircraft by a unit degree. But, we wish to represent these pressure loads with the four actuators we have in terms of hardware. In this case, we utilize the principle of a modal equivalent point force to represent the pressure distribution as an applied force vector from aileron deflection in figure 1.2. This modal equivalent force is a direct translation of the pressure induced by deflection into applied load on the wings, which consequently means that the delay from an aileron deflection signal to realized force on the wing remains unmodeled.

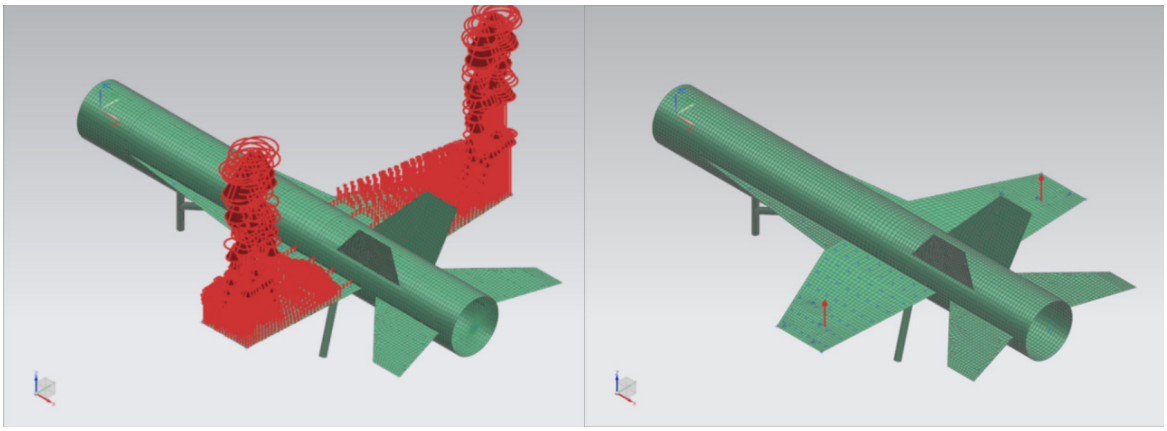

Figure 1.3: Modeled pressure induced from aileron deflection (left). Modal equivalent point force of aileron deflection (right). [6]

We also obtain a modal equivalent point force to represent the pressure distribution induced by increasing angle of attack. This is what we prescribe to our disturbance input actuators which will provide input meant to simulate gust loading conditions.

Thus, we position the linear actuators at each of these four modal equivalent points which will grant us a pair of actuators to simulate pressure loading on the wings from flight dynamics and a separate pair of actuators to simulate the induced pressure by altering the aileron deflection in figure 1.3. We now have a pair of actuators which will simulate gust loads perturbing the wings of our system and another pair acting as control surface ailerons with which we will counteract the disturbance.

In terms of constraints on the response of the actuators, there were not any physical constraints which were enforced in terms of aileron responsiveness. This means that while the actuators might be able to output $\pm 1 ft - lb$ force at frequencies exceeding $100 Hz$, this may not be the most realistic depiction of the system's aileron response. If a high performing aircraft system has an upper ceiling in terms of roll rate of $280°/s$, then the frequency response of an aileron system likely needs not be substantial after a couple of Hz. This study will assume designs vehicles which might be able to implement an aileron system able to act upon higher frequency disturbances, up to $30 Hz$ or so.

The accelerometers measure with units of in/s^2 which means it is possible to measure the wing bending dynamics given some force input from the actuators. However, we are interested in relating the measured output of the system with the individual modal components which compose the total displacement dynamics of the wing bend-

ing. For this reason, we will construct a state space dynamical model and apply a modal coordinate transformation method to obtain modal state variables.

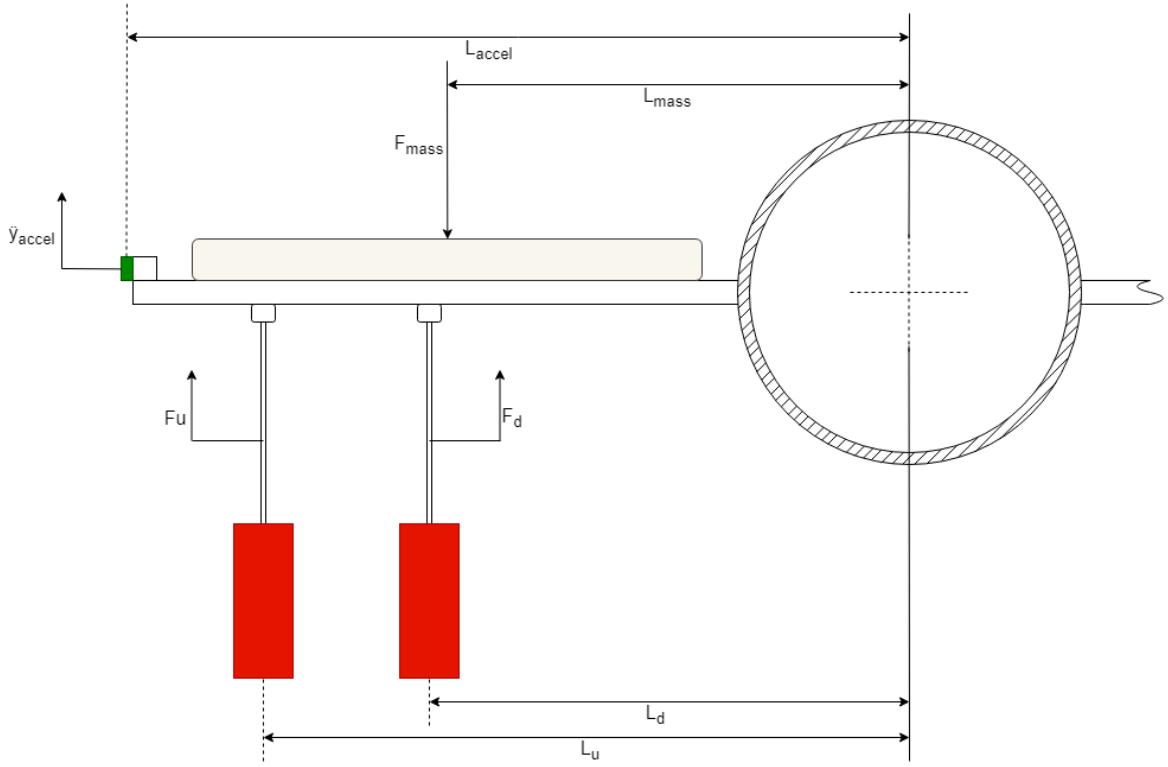

Figure 1.4: Section-view free body diagram of system force and acceleration vectors on one wing.

When we evaluate performance and begin experimental testing, we drive the disturbance actuators with different functions of frequency in order to excite the modal components of the wings. Then, we design a controller in such a way as to attenuate the modal components of the disturbance with the control actuators.

In order to represent uncertainty in the plant, sand bags were applied to the wings in various configurations. The physical interpretation of this added weight could have two interpretations. One might be the differing payload conditions on the wings perhaps due to added or depleted fuel, and another could be off-nominal airloading conditions on the wings from induced vortices due to dynamic presssure shifts at differing airspeeds. The sand bags add both weight on the wings and torque with respect to the centerline of the fuselage. These two parameters changing are important, as they will become the focus of deriving a trend with respect to varying modal parameters with each configuration.

With respect to a free body diagram of the experimental setup representing vectors of forces as well as the measured acceleration vector, there will be the force applied to the wing by the control input actuator F_u, the force applied to the wing by the disturbance actuator F_d, the y component of the accelerometer measurement $\ddot{y}_{accel}$, and the point load equivalent weight from the added sand bag mass F_{mass}. The lengths of each of these locations with respect to the fuselage centerline are given by L_u, L_d, L_{accel}, and L_{mass} respectively. The free body diagram is given in figure 1.4.

Chapter 2

Experimental Setup and Design Environment

With the state space model defined in terms of the flight dynamics and equations of motion pertaining to the wing bending modes, we now wish to discuss the experimental setup and process in more detail. We discuss the experimental setup and the methods for linearizing the system with regards to all the moving hardware elements.

2.1 Experimental Setup

The test article is a steel sheet metal structure with discrete parts which have been welded together, including a chassis, wings, tail flaps, and legs. The structure is suspended upside down from the ceiling using steel springs with known stiffness, coil windings, and wire diameter. Attached to each wing are two separate pairs of actuators. As described earlier, one pair of actuators represent the disturbance input from an equivalent pressure load while the other pair represents the equivalent force from induced pressure when deflecting aileron control surfaces [6]. In this case, each aileron acts independently of one another in order to control modal disturbances on the wings. The system also features accelerometers at each end of the wings on both the leading edges and trailing edges.

The mass loading conditions are featured in 6 unique configuration as well as the nominal zero-loading condition. A depiction of each of these configurations can be seen in figure 2.2.

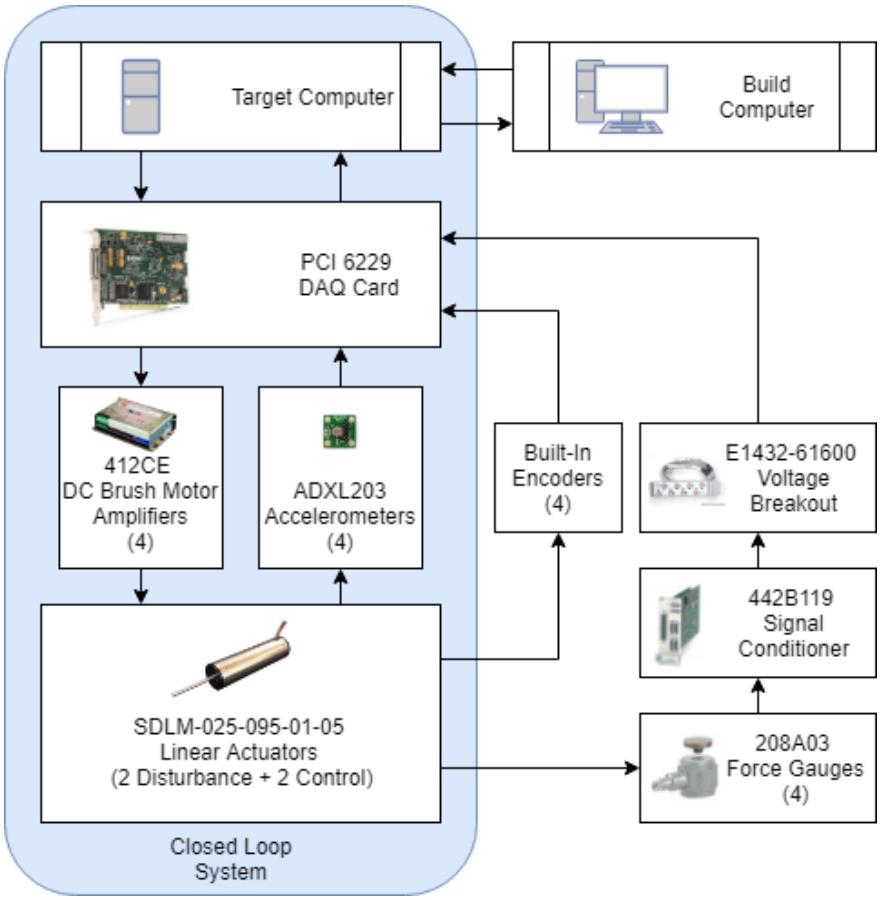

Figure 2.1: System Block Diagram.

2.1.1 Data Acquisition

The accelerometer outputs provide measurements of disturbances at the wings which can be interpreted by the implemented control system in order to provide control input and affect the resulting system dynamics. The data acquisition system (DAQ) features a National Instruments PCI 2660 card [37] [36] slotted into a machine running a Simulink Realtime operating system that interfaces directly with the NI card for I/O operability. The card itself and the breakout board can be seen in figure A.1. The structure of the control model is therefore represented within the Simulink Realtime environment, featuring block diagrams and graphical depictions of signals, components, and LTI systems [46].

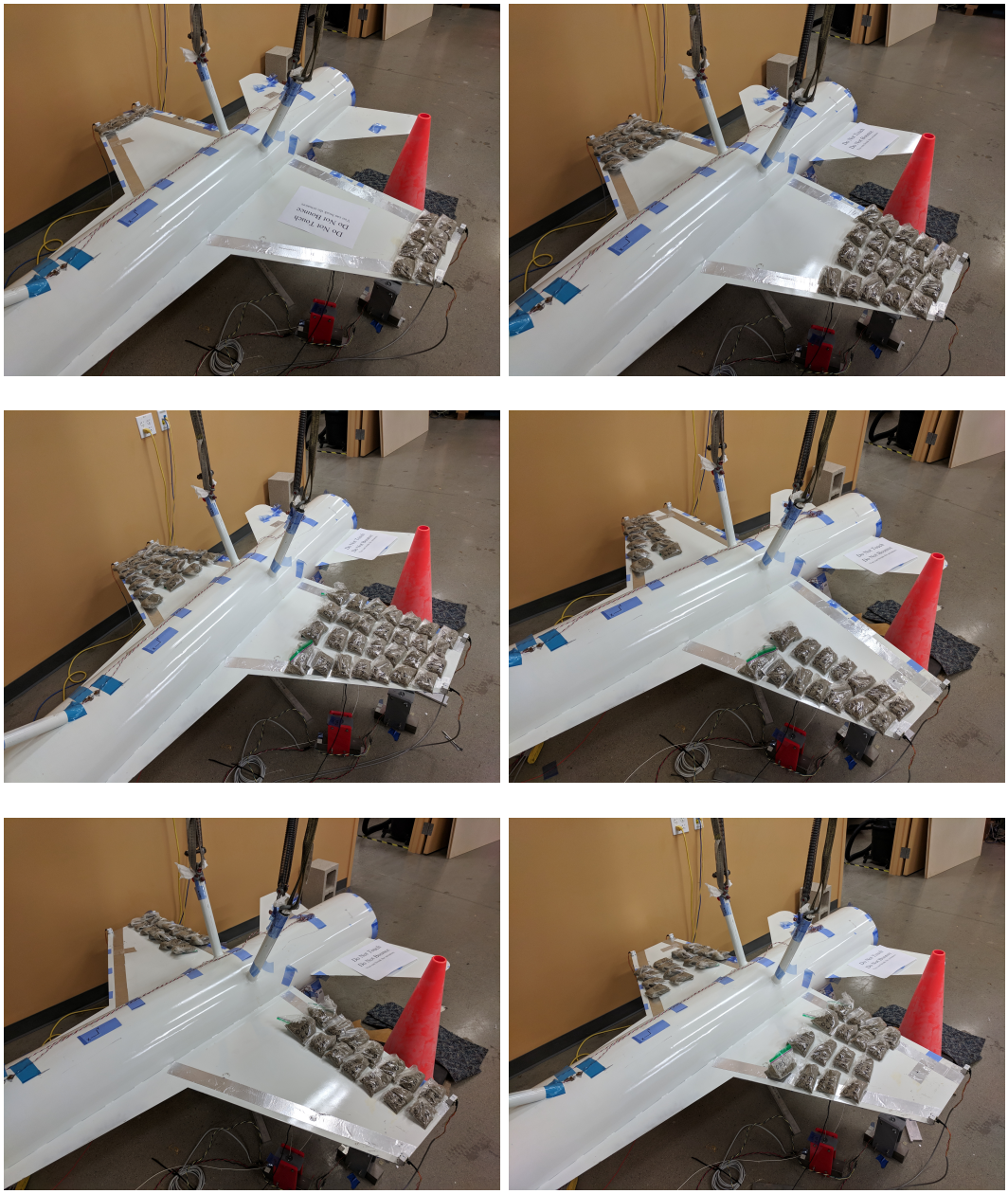

Figure 2.2: Configuration 1 (Upper-Left), 2 (Upper-Right), 3 (Middle-Left), 4 (Middle-Right), 5 (Lower-Left), and 6 (Lower-Right).

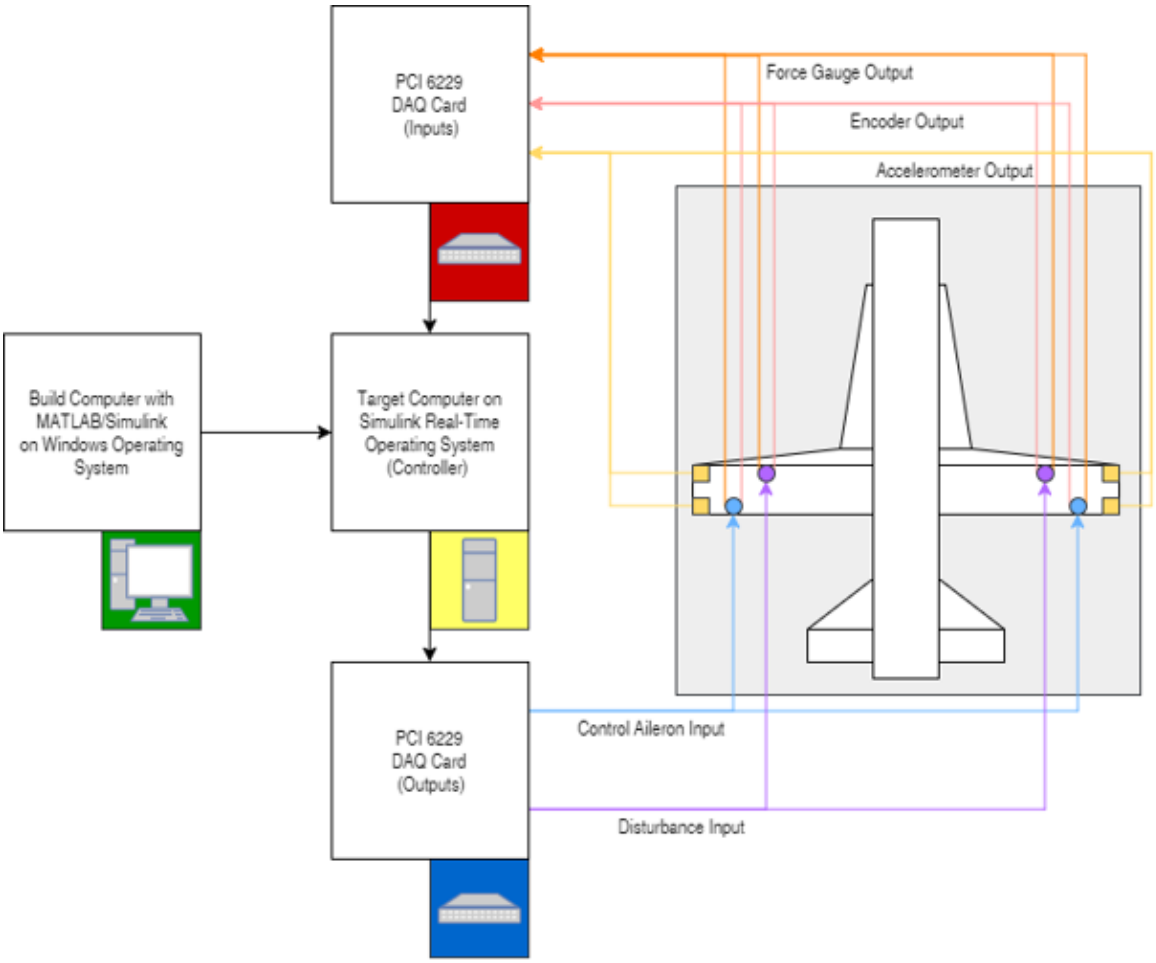

Figure 2.3: Overview of System.

2.1.2 Linear Actuators

The actuators are Moticont SDLM-025-095-01-05 linear direct drive motors [35], and a picture can be seen in figure A.2. They were calibrated using a test stand to linearize the output at low input signal to overcome the nonlinear deadzone and stiction effects present near zero drive. The lookup tables are implemented into the Simulink Realtime environment.

The actuators were calibrated on a test stand by running input signals of certain frequencies at different voltage amplitudes. The testing array included voltage amplitudes of 0.5 V, 1.0 V, 1.5 V, 2.0 V, 2.5 V, 3.0 V, 3.5 V, 4.0 V, 4.5 V, and 5.0 V running at 0 Hz (Constant Input), 1 Hz, 5 Hz, 10 Hz, 50 Hz, 75 Hz, 100 Hz, and 200 Hz. After running the tests, the output data was fitted to a sinusoidal signal using least squares regression with amplitude and phase parameters to identify the output

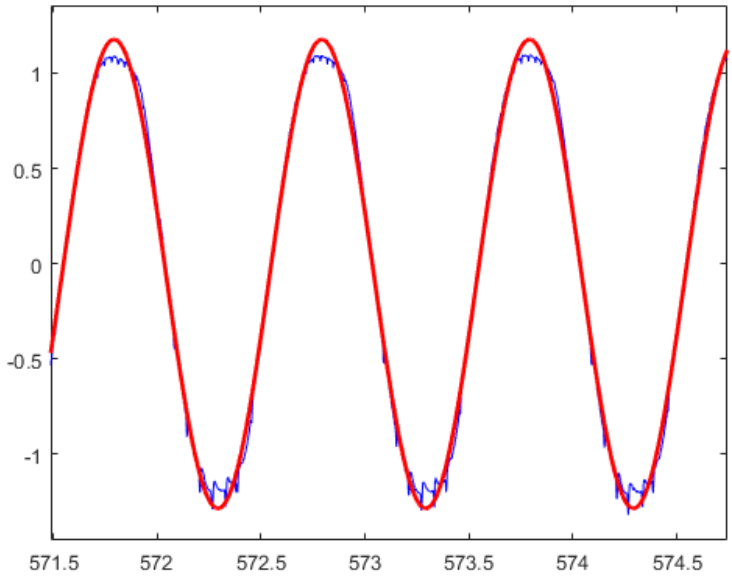

Figure 2.4: Example of Least Squares Fitting Routine on Experimental Data.

amplitude of the force sensor reading. Thus we establish a relation between the input voltage signal amplitude to the output force amplitude as a function of frequency. We notice that the actuator's output force signal has some choppiness near the peaks referencing figure 2.4, and this is likely due to slight tension to compression transition within the test stand assembly.

The derived output voltage amplitudes are plotted for each input signal frequency and input signal amplitude as seen in figure 2.5. Then the data points are averaged over each frequency to obtain a calibration curve function with first order linear interpolation between points. A lookup table is then implemented into the Simulink Realtime environment using these derived curves for each actuator. The inverse curves formed by linear interpolation are shown in figure A.10. The R^2 coefficients of determination for both the individual curves and the averaged curves over the input frequency and amplitude range for control are represented in tables B.3, B.4, B.5, and B.6. Overall, the fitted inverse calibration model fits well in the higher amplitude range and suffers at lower amplitude range primarily because the signal to noise ratio becomes unfavorable and difficult to model.

The actuators are driven by a Copley Controls Corp. 412CE DC Brush Motor Amplifier [9] which uses an Artesyn Embedded Technologies LCC600-48U-4P External Power Supply [3] and a Schaffner FN2070-12-06 AC/DC EMI Filter [44]. These can

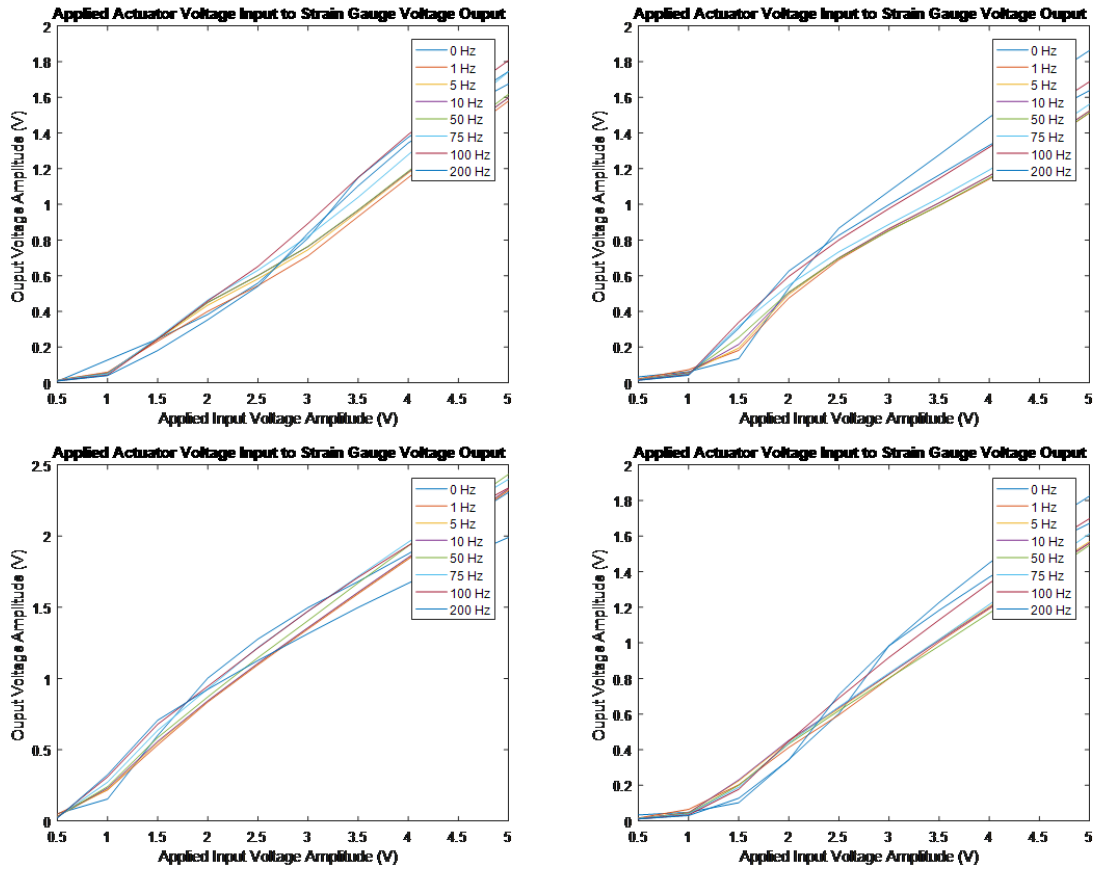

Figure 2.5: Actuator 1 Calibration Curve (Top Left). Actuator 2 Calibration Curve (Top Right). Actuator 3 Calibration Curve (Bottom Left). Actuator 4 Calibration Curve (Bottom Right).

be seen in figure A.3.

2.1.3 Accelerometers

The accelerometers are Analog Devices ADXL203 2-axis accelerometers with $\pm 1.7g$ range [2] [1], and a picture can be seen in figure A.4.

The physical connection between the accelerometer and the breakout board for the DAQ proved to be sensitive to signal compromise. Displacing a wire connected to the board slightly might lead to significant shifts in the measured output signal due to grounding issues. Thus, a need to resolve potential grounding or impedance issues arose which was solved by experimentally connecting to different inpout channels on the DAQ unit and determining the best behaving input channels. In addition, before each set of experiments, the system would be initialized and held neutrally to

determine good signal quality without drift.

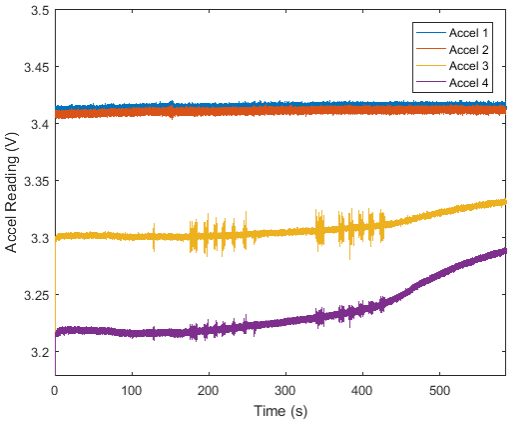

Figure 2.6: Accelerometer Output Drift Test.

A separate calibration process was initiated for the accelerometers by fixing each of them to a machined block and taking static voltage readings at 90° increments corresponding to $\pm 1g$ and neutral. Taking the static readings allowed for calibration gains to be set in the control environment.

2.1.4 Force Sensors

The force sensors present at the end of the actuator stingers are PCB 208A03 force sensor with $500lbf$ range [38] [40]. While not used in closed loop control, these sensors provided validation of the accelerometer readings. The force sensors are connected to a Hewlett Packard US35375424 E1432-61600 voltage breakout unit [22] and Vishay 2120A signal conditioning module [39]. Depictions of the force sensor and the voltage breakout and conditioner module can be viewed in figure A.5.

A separate force sensor was used on a test stand for calibration of the linear actuators. This force sensor is an Interface, Inc. WMC-5 force gauge [26].

2.1.5 Other Hardware

The system also utilizes a separate power supply for a dedicated 5V line to the DAQ system and the accelerometers. The power supply is a Power Designs, Inc. TP330 voltage generator. In addition, there was a Rigol DS1000D oscilloscope used to test and validate measured output signals of the accelerometers [41] [42]. This oscilloscope was used to calibrate each accelerometer to obtain the V/g gain coefficients.

The test fixture used to calibrate the accelerometers was a simply machined block with mounting interface for each accelerometer that allowed for separate 90^o rotation. The test stand for calibrating the linear actuators was $3D$ printed with some simple hardware including a male thread adapter allowing for a nut and washer to be fastened to one end.

2.2 Experimental Testing Procedures

Over the course of experimental testing, many different series of tests were performed on the Iron Bird article. We will review some of these tests and the necessary procedures in this section.

2.2.1 Adjusting the Actuators

In any testing involving exciting the Iron Bird, it proves necessary to align the actuators in such a way as to ensure that the rod rests mid stroke within the actuator body, this ensures the full dynamic range of each linear actuator is available, and it correlates with the state in which the actuators were calibrated. The adjustment of the stroke position was accomplished with threaded spacers which connected two separate stingers, one stinger to the force sensor attached to the Iron Bird wing and one stinger threaded into the actuator. Whenever the mass configurations were changed, the vertical position of the Iron Bird would also shift which meant the actuators needed to be readjusted for proper alignment.

Each actuator rested in a custom 3D-printed housing which could be propped up on metal plates as necessary for added height. The housing could also be adjusted for rotation in order to ensure that the stingers were in line and normal to the wing surface which is very important to preserving the mechanical transfer of force without bending during testing operation. The spacer was torqued with two separate nuts to ensure resilience to vibration without being too much of a hassle to readjust and reposition.

2.2.2 Connecting the DAQ

When wiring the DAQ, we have already discussed the wire sensitivity when connecting the accelerometers. The wires connecting to the accelerometer were shielded

in a protective sleeving. However, the mechanical connection to the DAQ proved troublesome and required care in reconnecting over each series of tests. In addition to the accelerometers, the force gauges, the motor outputs, and the encoder signals were all wired into the DAQ system. Some of the channels needed to be changed in order to separate the signals; in certain cases correlation in a strong signal could be seen with a weaker signal if the two channels featured a significant degree of crosstalk.

2.2.3 Simulink Realtime Environment

The Simulink Realtime environment was constructed much in the same way as a standard Simulink model would be built, the key difference being that there is both a build computer and a target computer. The build computer features a Windows OS environment running MATLAB r2017a. The realtime model is constructed in Simulink in the same way a normal model would be built. The the measured outputs originate from an "Analog Input" block and then the system connects the control/disturbance inputs to the "Analog Output" block for the PCI 6229 card using the built-in library. Transforming the signals in between involves implementing all necessary gains, LTI system blocks, lookup tables, filters, and mathematical operations.

From the analog output, we take the measured accelerometer voltages and transform them to proper units through the derived accelerometer gains taking units from V to in/s^2. This signal is then passed to the controller LTI block. The output of this block will be the control inputs, so these input signals need to be passed through an appropriate lookup table based on the calibration testing of each actuator. The output signal from the lookup table will then be connected to the PCI 6229 analog output block and drive the control actuators through the motor amplifier. The disturbance signal is transformed similarly using their own lookup tables. The disturbance signals are generated based on some signal formulation depending on the appropriate test, i.e. chirp, white noise, or step. These manual signal definitions for testing may also be applied to the input actuators and they were utilized during the system identification testing to formulate an experimental plant model for comparison to the FEA derive model.

The system was sampled at $500Hz$. Each control model was discretized when implemented into the Simulink Realtim control environemnt. Once the model is designed and implemented into the discrete time environment, the build computer packages the control model and sends it to the target computer which is running within a MATLAB

Simulink Realtime r2017a OS environment.

An overview of the Simulink Realtime layout can be seen in figure A.8. An example of the experimental scope layout monitored by the target computer during testing can be seen in figure A.9.

2.2.4 System Identification/Parameter Estimation Testing

In order to obtain an experimental-based model of the system for comparison to the FEA derived model, the input actuators were given individual chirp excitation signals. This meant that the frequency content for each transfer function from input to output could be obtained experimentally. With each test run, the system would be driven by a linear chirp signal. This was performed with both inputs on each configuration of the system.

In the case of the single input chirp tests, system identification transfer function estimation techniques were utilized with the MATLAB system identification toolbox and instrumental variable initialization in order to obtain experimentally derived system parameters [33] [34]. These poles and frequencies which were of interest were defined in such a way that all transfer functions shared the same denominator, i.e. only the zeroes differ between input to output. Frequency spectra analysis is also a useful tool for analyzing experimental data for comparing to the derived modes.

The primary details which were most important was the structure of the poles. More specifically, it was crucial to evaluate the change in natural frequency as a means to provide a structural uncertainty model. Therefore, the experimental chirp results were processed via the MATLAB system identification toolbox [34] for each input signal to configuration. In cases where some of the resonant modes were unclear, multiple transfer functions were derived for the separate output channels and compared in order to establish congruence in the denominator terms. The method of identification was to follow the following procedure.

1. Remove any non-zero means in the output data
2. Apply a band pass filter limiting the range for frequency to $18 rad/s$ to $180 rad/s$
3. Estimate a transfer function with 12 zeros and 12 poles utilizing instrumental variable method of initialization

4. As part of the estimation process, fit the model to the frequency range $18 rad/s$ to $180 rad/s$

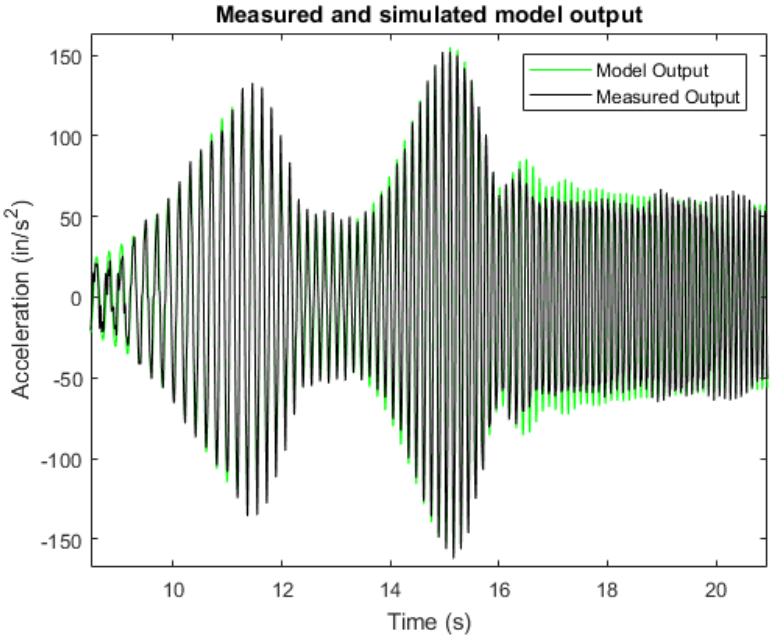

Figure 2.7: System identification plot of measured compared to simulated for input 1 to output 1.

Following this procedure along with any other necessary corrections or truncation of data allowed for data to be fit to a suite of experimentally derived models such as the nominal input 1 to output 1 model with response shown in figure 2.7. In this case, obtaining a perfect model which satisfies a certain error residual criterion is not the primary objective so much as obtaining reasonable estimates of the natural frequencies, especially as they change from configuration to configuration. In this sense, we are employing system identification tools to perform parameter fitting, because we have some defined structure for the model and wish to derive the parametric changes of frequency with the differing mass loads. This process requires a comparison of models so as to validate the derived frequencies from each one. The damping coefficients which will be used for the experimentally derived model are the same as those for the FEA based model.

Table 2.1: Experimentally derived natural frequencies per configuration.

Mode Number	Natural Frequency (ω_n) [Hz]							Damping Ratio (ζ)
	Nominal	Config 1	Config 2	Config 3	Config 4	Config 5	Config 6	
1	5.3	4.65	4.55	4.5	4.7	4.7	5	0.12
2	7.2	6.825	6.775	6.725	6.875	6.875	7.1	0.12
3	11.78	10.35	10.35	10.03	9.87	11.46	10.34	0.08
4	12.73	12.25	11.78	10.35	12.41	13.05	11.62	0.08
5	23.5	23.25	19.75	19	20.75	21	20.75	0.02
6	29	26	23.5	23.5	27	25	25	0.02

2.2.5 Control Testing

Throughout the design and experimental process, many tests were performed on the system with various control designs in place. Common tests included step responses to make sure the controller was stable, sine dwells to test how well a controller attenuates modal disturbance, chirp bursts to test the overall performance of a controller across a broader frequency spectrum, and white noise tests for the same reason.

Description of Testing Signals:

1. Symmetric Sine Burst: Both disturbance actuators are driven by the following sinusoidal signal

$$d(t) = sin(sin(t) \cdot t) \tag{2.1}$$

2. Asymmetric Sine Burst: The disturbance actuators are driven by opposing sinusoidal signals which are similar to the symmetric case but opposite

$$\begin{aligned} d_1(t) &= sin(sin(t) \cdot t) \\ d_2(t) &= sin(sin(t) \cdot (t + \pi)) \end{aligned} \tag{2.2}$$

3. White Noise: The disturbance actuators are driven by random white noise Gaussian signals with sampling time equal to the system sampling time of $0.002Hz$

$$\begin{aligned} d_1(t) &= \mathcal{N}(0, 1) \\ d_2(t) &= \mathcal{N}(0, 1) \end{aligned} \tag{2.3}$$

2.3 Simulation and Design Environment

A separate workstation was utilized for control model design and simulation. This consisted of MATLAB with Simulink.

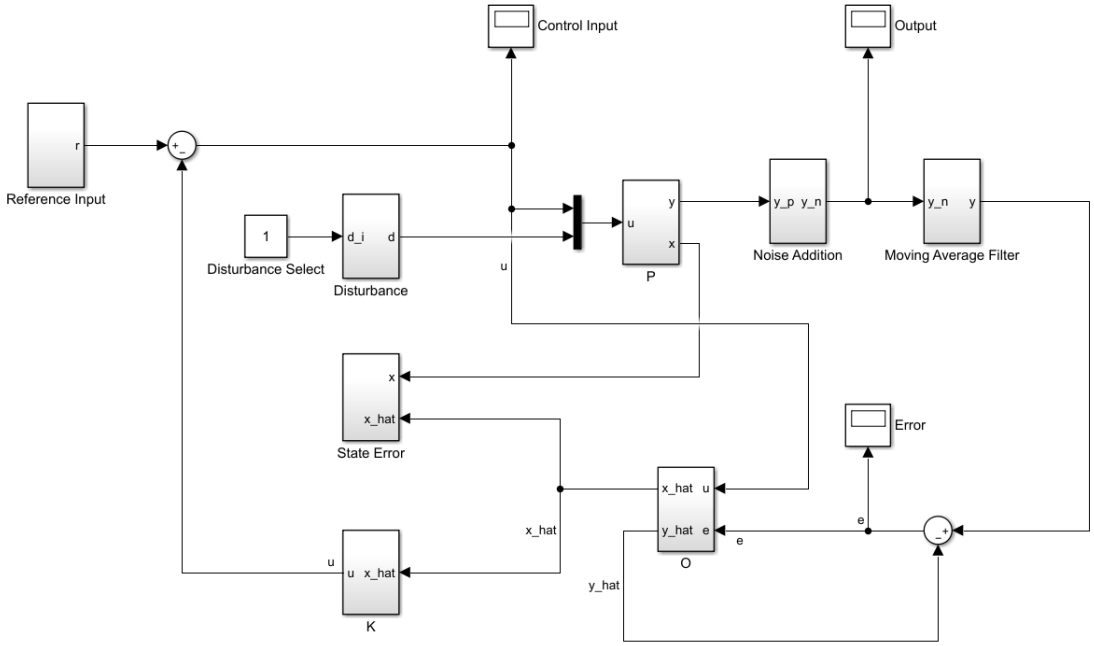

Figure 2.8: Simulink Environment (Top Level).

MATLAB scripts were developed in order to build and evaluate controllers based on standard criteria for evaluation. The project utilized the control system toolbox and the robust control toolbox for control design. A Simulink model was developed in order to implement control designs and test plant dynamics in the presence of error. An overview of the top level Simulink block diagram is seen in figure 2.8.

A simulation environment was developed in order to test lower order models against a higher order plant in the presence of noise. One of the more useful developments for creating a simulation environment was the ability to derive the approximate damping ratios of the system for each mode by comparing the experimental step response of the system against the simulated step response of the full model. By measuring the settling time and counting the number of peaks, a reasonable estimate of the system damping was obtained and implemented into subsequent models with a comparison shown in figure 2.9.

Similar methodology was used to determine an appropriate process covariance matrix. The accelerometer covariance data was expressed as a diagonal covariance matrix for the measurement data. With this and the system model, an estimator was formulated using an arbitrary weighting of the process noise covariance. A step input

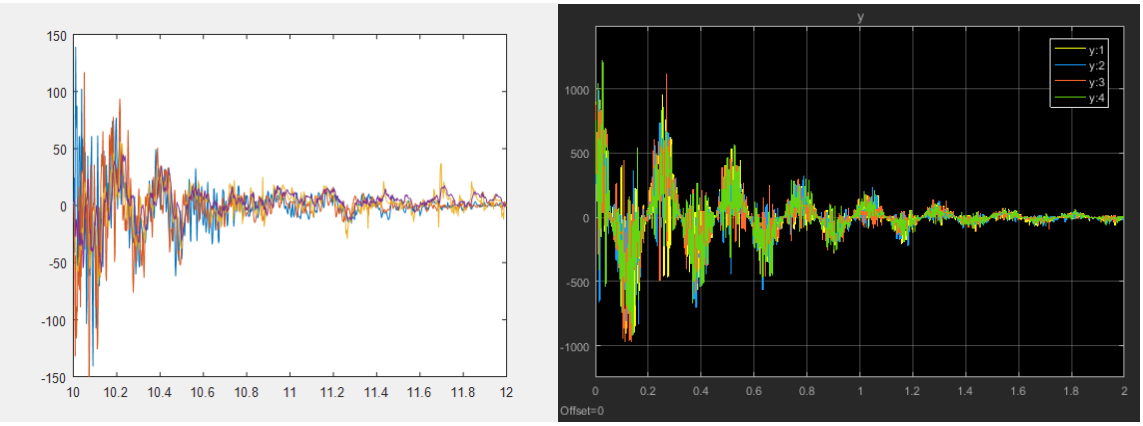

Figure 2.9: Experimental step response (left). Simulation step response (right).

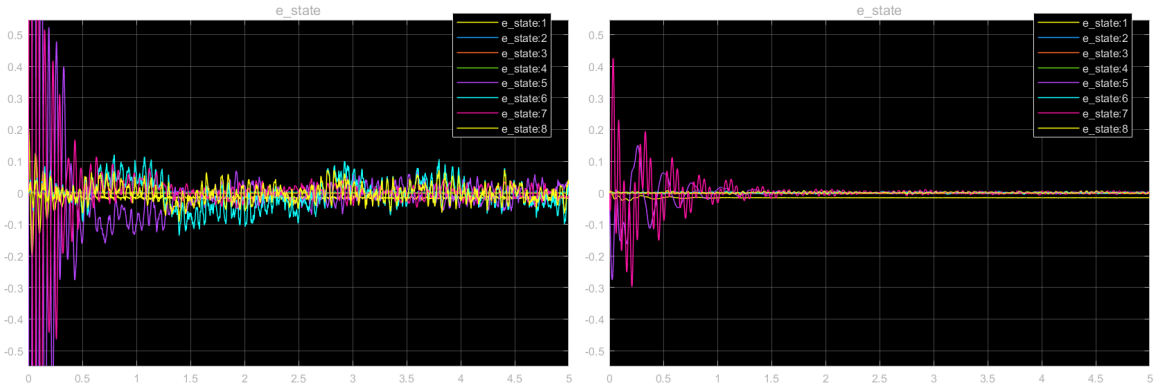

Figure 2.10: State error from step response with high process noise covariance (left) and balanced coavariance (right).

was applied to the system and the state estimator was observed and directly compared to the true states in simulation. If the process covariance was too highly weighted, the system would be too sensitive to noisy measurements, and the state error would not settle. So, it was balanced appropriately in order to obtain acceptable settling time for steady state error in the estimator as seen in figure 2.10.

Chapter 3

Model

3.1 Deriving the State Space Plant Model

To construct a plant model, the system is assumed to be a multi-degree of freedom system composed of as many points as the FEM requires. For a generalized equation of motion in multiple degrees of freedom, we will state an equation of motion then apply a modal coordinate transformation to achieve a MIMO state space model [16].

$$[M]\ddot{x} + [C]\dot{x} + [K]x = \{F\} \tag{3.1}$$

In the above equation, x is the displacement vector of each point, M represents the mass matrix of the system, C represents the damping matrix of the system, K represents the stiffness matrix of the system, and F is the set of external forces applied at each point. By expressing the equations of motion in this generalized form, it is now possible to express an eigenvalue problem for an eventual change of coordinates application to express our system in terms of modal coordinates.

$$[[K] - \lambda[M]]x = 0 \tag{3.2}$$

What is convenient for modal analysis is the fact that the eigenvalues of this solution are directly related to the natural frequencies of the harmonic modes of the system. In matrix form, the eigenvalues become a diagonal matrix of the square of the natural frequencies of each mode.

$$[\bar{\Omega}^2] = \begin{pmatrix} \bar{\omega}_{1,1}^2 & 0 & \cdots & 0 \\ 0 & \bar{\omega}_{2,2}^2 & \cdots & 0 \\ \vdots & \vdots & \ddots & \vdots \\ 0 & 0 & \cdots & \bar{\omega}_{n,n}^2 \end{pmatrix} \tag{3.3}$$

The eigenvectors corresponding to each eigenvalue can be defined.

$$[V] = \begin{pmatrix} \{v_1\} & \{v_2\} & \cdots & \{v_n\} \end{pmatrix} \tag{3.4}$$

By solving 3.2 in terms of the eigenvalues 3.3 and eigenvectors 3.4, it can be shown that each distinct mode will be independent from one another due to orthogonality which will result in completely diagonal modal mass and stiffness matrices under the correct manipulation using eigenvectors and eigenvector transposes, where the transpose is denoted in the form A^*.

$$\begin{gathered} [K][V] = [M][V][\bar{\Omega}^2] \\ [K]\{v_i\} = \lambda_i[M]\{v_i\} \\ \{v_j\}^*[K]\{v_i\} = \lambda_i\{v_j\}^*[M]\{v_i\} \\ \{v_i\}^*[K]\{v_j\} = \lambda_j\{v_i\}^*[M]\{v_j\} \\ (\lambda_i - \lambda_j)\{v_i\}^*[M]\{v_j\} = 0 \\ \{v_i\}^*[M]\{v_j\} = 0 \quad for \quad i \neq j \\ \{v_i\}^*[M]\{v_j\} = \bar{m}_{i,i} \quad for \quad i = j \\ \{v_i\}^*[K]\{v_j\} = \bar{k}_{i,i} \quad for \quad i = j \end{gathered}$$

Therefore, because non-zero values exist only when the row and column indices are equal, the modal mass and modal stiffness matrices can be defined as the following diagonal matrices.

$$[V]^*[M][V] = \bar{M} = \begin{pmatrix} \bar{m}_{1,1} & 0 & \cdots & 0 \\ 0 & \bar{m}_{2,2} & \cdots & 0 \\ \vdots & \vdots & \ddots & \vdots \\ 0 & 0 & \cdots & \bar{m}_{n,n} \end{pmatrix} = I \tag{3.5}$$

$$[V]^*[K][V] = \bar{K} = \begin{pmatrix} \bar{k}_{1,1} & 0 & \cdots & 0 \\ 0 & \bar{k}_{2,2} & \cdots & 0 \\ \vdots & \vdots & \ddots & \vdots \\ 0 & 0 & \cdots & \bar{k}_{n,n} \end{pmatrix} = [\bar{\Omega}] \tag{3.6}$$

Note that the normalized mass matrix ends up being an identify matrix, and the normalized stiffness matrix ends up being equal to the diagonal natural frequency matrix.

The Modal coordinate transformation can be performed with the following change of variables.

$$x = [V]\tilde{x} \tag{3.7}$$

Applying this change of variables and premultiplying 3.1 by $[V]^*$ leads to modal coordinate form.

$$\begin{aligned} [V]^*[M][V]\ddot{\tilde{x}} + [V]^*[C][V]\dot{\tilde{x}} + [V]^*[K][V]\tilde{x} &= [V]^*\{F\} \\ [\bar{M}]\ddot{\tilde{x}} + [\bar{C}]\dot{\tilde{x}} + [\bar{K}]\tilde{x} &= [V]^*\{F\} \end{aligned} \tag{3.8}$$

Note that $\bar{C}$ is not necessarily diagonal as it depends on how the damping is modeled. For simplicity and to draw a comparison to harmonic motion, it is best to model this relative to the natural frequency of each mode. It becomes possible to formulate a state space equation by rearranging terms and premultiplying by $[\bar{M}]^{-1}$.

$$\dot{\tilde{x}} = \begin{pmatrix} 0 & I \end{pmatrix} \begin{pmatrix} \tilde{x} \\ \dot{\tilde{x}} \end{pmatrix} \tag{3.9}$$

$$\ddot{\tilde{x}} = -[\bar{M}]^{-1}[\bar{C}]\dot{\tilde{x}} - [\bar{M}]^{-1}[\bar{K}]\tilde{x} + \Big([\bar{M}]^{-1}[V]^*\Big)\{F\}$$

$$\ddot{\tilde{x}} = \begin{pmatrix} -[\bar{M}]^{-1}[\bar{K}] & -[\bar{M}]^{-1}[\bar{C}] \end{pmatrix} \begin{pmatrix} \tilde{x} \\ \dot{\tilde{x}} \end{pmatrix} + \Big([\bar{M}]^{-1}[V]^*\Big)\{F\} \tag{3.10}$$

By combining 3.9 and 3.10, the state space matrices for A and B can be defined.

$$\begin{pmatrix} \dot{\tilde{x}} \\ \ddot{\tilde{x}} \end{pmatrix} = \begin{pmatrix} 0 & I \\ -[\bar{M}]^{-1}[\bar{K}] & -[\bar{M}]^{-1}[\bar{C}] \end{pmatrix} \begin{pmatrix} \tilde{x} \\ \dot{\tilde{x}} \end{pmatrix} + \begin{pmatrix} 0 \\ [\bar{M}]^{-1}[V]^* \end{pmatrix} \{F\} \tag{3.11}$$

Given the fact that $[\bar{M}]$ and $[\bar{K}]$ are both diagonal, the diagonal matrix of $[\bar{\Omega}^2]$ can be substituted, and to model the damping, a diagonal matrix representing the product of $2[\bar{Z}][\bar{\Omega}]$ can be used in place of $[\bar{M}]^{-1}[\bar{C}]$. For formulating B, a subset of the applied forces can be taken at the points where control inputs exist. Consider a subset of F consisting of two force values defined at the points in space where the control inputs exist on the physical article. Due to the fact that all other values of F will be zero and the fact that F is multiplied into the matrix consisting of rows of transverses of the eigenvectors, it is possible to take a subset of indices over the vector of F and over each vector of $\{u\}^T$ corresponding only to the control input locations to fully represent B.

$$[\bar{Z}] = \begin{pmatrix} \bar{\zeta}_1 & 0 & \dots & 0 \\ 0 & \bar{\zeta}_2 & & 0 \\ \vdots & & \ddots & \vdots \\ 0 & 0 & \dots & \bar{\zeta}_r \end{pmatrix}$$

$$\begin{pmatrix} \dot{\tilde{x}} \\ \ddot{\tilde{x}} \end{pmatrix} = \begin{pmatrix} 0 & I \\ -[\bar{\Omega}^2] & -2[\bar{Z}][\bar{\Omega}] \end{pmatrix} \begin{pmatrix} \tilde{x} \\ \dot{\tilde{x}} \end{pmatrix} + \begin{pmatrix} 0 \\ [\bar{M}]^{-1}[v_{in}]^* \end{pmatrix} \begin{pmatrix} F_{in} \end{pmatrix} \tag{3.12}$$

In order to define the state space matrices of C and D, a reverse change of variables needs to be applied to 3.12 using the inverse of 3.7 as shown below. This results in a mapping of the modal coordinates back to the displacement state representation by premultiplying with the appropriate set of output eigenvectors. The input matrix already features an eigenvector mapping from input force to modal force.

$$\tilde{x} = [V]^{-1}x$$
$$\dot{\tilde{x}} = [V]^{-1}\dot{x}$$
$$\ddot{\tilde{x}} = [V]^{-1}\ddot{x}$$
$$\begin{pmatrix}\dot{x}\\ \ddot{x}\end{pmatrix} = [V]\begin{pmatrix}0 & I\\ -[\bar{\Omega}^2] & -2[\bar{Z}][\bar{\Omega}]\end{pmatrix}\begin{pmatrix}\tilde{x}\\ \dot{\tilde{x}}\end{pmatrix} + [V]\begin{pmatrix}0\\ [\bar{M}]^{-1}[v_{in}]^*\end{pmatrix}\Big(F_{in}\Big)$$

Taking only the acceleration component to define the outputs at the accelerometer sensors and defining a subset where those accelerometers are located yields a further condensed state space equation for C and D.

$$\Big(\ddot{x}_{out}\Big) = \Big([v_{out}]\Big)\Big(-[\bar{\Omega}^2] \quad -2[\bar{Z}][\bar{\Omega}]\Big)\begin{pmatrix}\tilde{x}\\ \dot{\tilde{x}}\end{pmatrix} + \Big([v_{out}]\Big)\Big([\bar{M}]^{-1}[v_{in}]^*\Big)\Big(F_{in}\Big) \tag{3.13}$$

To put the state space equations together, take r modes from the set of all modal states p and express 3.12 and 3.13 with the r modal states and the r modal state derivatives which implies a total number of states equal to $2r$. Also, express m outputs for the number of accelerometers used as output signals in feedback as well as n inputs for the number of control surface inputs used in the feedback control.

$$\begin{pmatrix}\dot{\tilde{x}}_r\\ \ddot{\tilde{x}}_r\end{pmatrix} = \begin{pmatrix}0 & I\\ -[\bar{\Omega}_r^2] & -2[\bar{Z}_r][\bar{\Omega}_r]\end{pmatrix}\begin{pmatrix}\tilde{x}_r\\ \dot{\tilde{x}}_r\end{pmatrix} + \begin{pmatrix}0\\ [\bar{M}_r]^{-1}[v_n]^*\end{pmatrix}\Big([u_n]\Big)$$
$$\Big(\ddot{x}_m\Big) = \Big(-[v_m][\bar{\Omega}_r^2] \quad -2[v_m][\bar{Z}_r][\bar{\Omega}_r]\Big)\begin{pmatrix}\tilde{x}_r\\ \dot{\tilde{x}}_r\end{pmatrix} + \Big([v_m][\bar{M}_r]^{-1}[v_n]^*\Big)\Big([u_n]\Big) \tag{3.14}$$

We note in our derivation we shall redefine $\tilde{x} = x$ and $x = y$ to realize our classical state space definitions of state and output variables.

$$\dot{x} = Ax + Bu$$
$$y = Cx + Du$$
$$\begin{pmatrix}\dot{x}_r\\ \ddot{x}_r\end{pmatrix} = \begin{pmatrix}0 & I\\ -[\bar{\Omega}_r^2] & -2[\bar{Z}_r][\bar{\Omega}_r]\end{pmatrix}\begin{pmatrix}x_r\\ \dot{x}_r\end{pmatrix} + \begin{pmatrix}0\\ [\bar{M}_r]^{-1}[v_n]^*\end{pmatrix}\Big([u_n]\Big)$$
$$\Big(y_m\Big) = \Big(-[v_m][\bar{\Omega}_r^2] \quad -2[v_m][\bar{Z}_r][\bar{\Omega}_r]\Big)\begin{pmatrix}x_r\\ \dot{x}_r\end{pmatrix} + \Big([v_m][\bar{M}_r]^{-1}[v_n]^*\Big)\Big([u_n]\Big)$$

Another useful result is the relation of state to output eigenvectors and input to state eigenvectors. We are able to define them in terms of the realized state space model, and the relation simplifies due to the $[\bar{M}^{-1}] = I$. Note the use of the Moore-Penrose Pseudoinverse, with the form $A^{\dagger}$.

$$A = \begin{pmatrix} \begin{bmatrix} 0 & I \end{bmatrix} \\ A_L \end{pmatrix}$$

$$B = \begin{pmatrix} 0 \\ B_L \end{pmatrix}$$

$$V_{in} = B_L \tag{3.15}$$

$$V_{out} = C \cdot A_L^{\dagger} \tag{3.16}$$

3.2 Realizing the Model

With the derived state space framework, we now utilize FEA software to analyze a solid model of the Iron Bird structure in order to obtain the modal eigenvalue solution of the system.

3.2.1 Finite Element Analysis

The dynamical model of the Iron Bird test article was obtained through a finite element study using NX Simcenter by Siemens. The model of the Iron Bird article was converted from a solid model from previous work. With this solid model, it becomes possible to obtain a shell model of the article using midplanes with assigned thickness. Previous work performed on this test article model to provide the solid model as well as element partitions of the model based on future aerodynamical analysis to be performed on certain sections of the wings and fuselage. The previous analysis and study was discussed in the Briggs paper [6].

Starting with the model of the Iron Bird, the system was constrained using three springs at each leg using CELAS elements. Assigning correct stiffness based on the material, thickness, and winding of the springs, the model was then meshed whilst ensuring proper mesh size and geometry. In certain cases, mesh size needed to be adjusted for certain difficult features of the model. Once the model has been meshed and constrained, then applying material and feature stitching leads to a complete

FEM. There was also the addition of ballast material and weight which was included in the final models.

In addition to modeling the ballast weight for the model, each configuration featured sand bags loaded on the wings in varying positions. These configurations were all each modeled. The results of the eigenvalue analysis provided the natural frequency with each mass-loaded condition to gain a sense for how the natural frequency changes from a model perspective. The actual models of the configurations could be utilized in theory to develop a suite of models for each configuration, however for this particular project, doing so would prove futile in obtaining the desired results, because the nominal model deviates from the actual test article by a significant factor. In fact, the fully loaded condition of the test article matched closest to the nominal model but not quite, indicating a deviation which exceeds the entirety of the structured uncertainty. This means that the unloading the mass will cause the controllers to perform worse than loading the mass, an inverted trend from the expectation of the model. The results of the model can always be tuned according to parameters established with system identification methods of the test article.

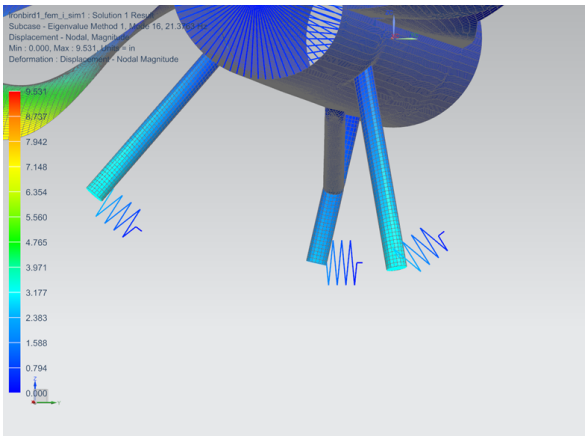

Figure 3.1: CELAS element constraints located on each foot.

The finite element modeling was performed through Siemen's NX NASTRAN with Simcenter as the postprocessor [25]. The spring elements were represented with CELAS elements in NASTRAN using the proper stiffness values attached at each foot as seen in figure 3.1. The ballast weight and wing loading weights of the system were modeled using simple attached mass elements.

SOL103 was used to solve the FEA and provide associated eigenvalue/eigenector data with generalized mass and stiffness matrices [24]. From the solution data, the

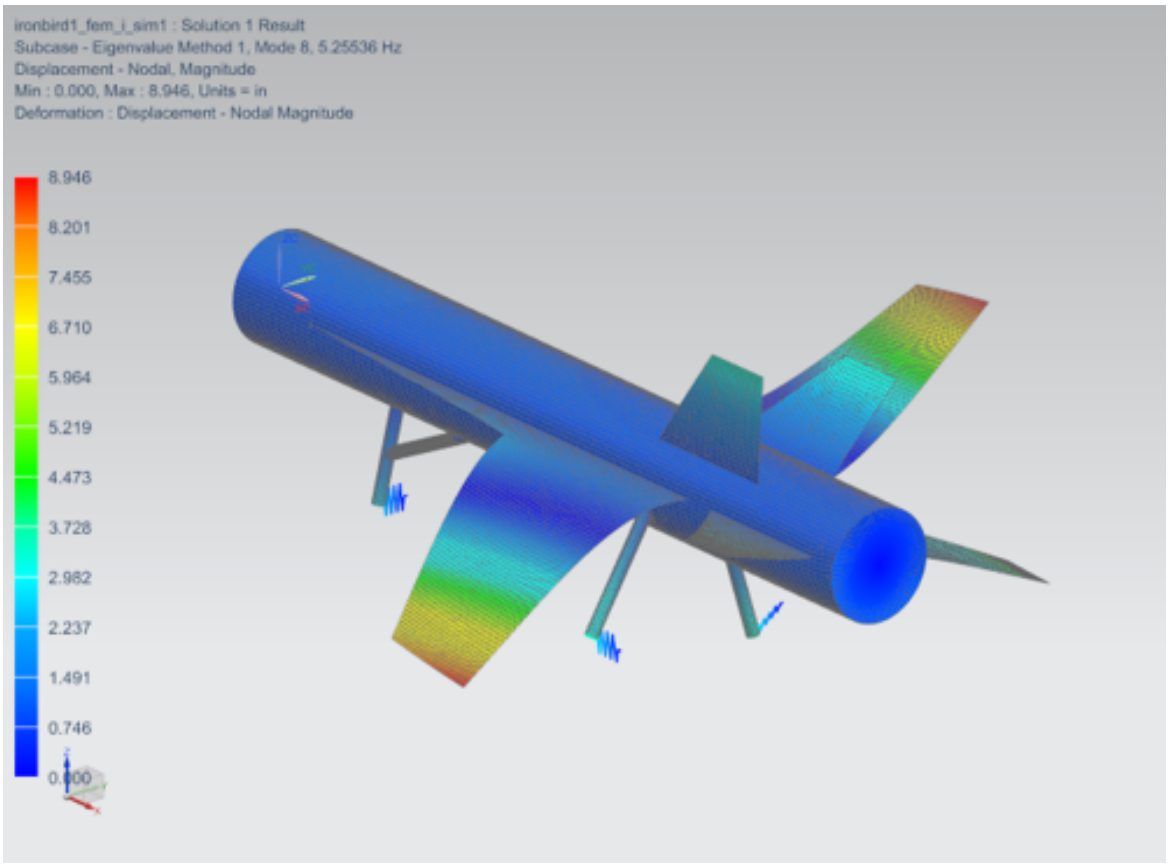

Figure 3.2: Iron Bird First Bending Asymmetric Mode FEA Solution.

rigid body modes are discarded, and the wing bending and torsional modes are included in the constructed model using IMAT functionality [4].

The damping is not derived from the FEA, but it is obtained from measuring the system response dynamics to a step input. The dynamics are tuned in simulation to obtain correlated response data. The rigid body modes are excluded from the model.

For control design, analysis, and implementation, we take the nominal condition to be zero added mass loading, and we consider a full state model with 6 total modes with two separate reduced models of 2 modes and 4 modes. These 6 wing modes are first bending symmetric, first bending asymmetric, first torsional symmetric, first torsional asymmetric, second bending symmetric, and second bending asymmetric respectively.

In any case, the finite element analysis provides eigenvalue related data which in turn provides information about the associated generalized mass matrix, generalized stiffness matrix, and generalized eigenvalue matrix. However, the analysis does not perform any sort of modeling of system damping, which is a source of considerable deviation.

Table 3.1: Model derived natural frequencies per configuration.

Mode Number	Natural Frequency (ω_n) [Hz]							Damping Ratio (ζ)
	Nominal	Config 1	Config 2	Config 3	Config 4	Config 5	Config 6	
1	3.788	2.53	2.42	2.43	2.87	2.80	3.30	0.12
2	5.25	4.15	4.14	4.09	4.15	4.37	5	0.12
3	14.67	10.42	9.33	9.40	10.95	12.10	10.88	0.08
4	14.79	10.46	9.37	9.43	11.15	12.23	10.99	0.08
5	20.26	16.71	13.59	12.20	15.66	13.93	14.49	0.02
6	21.45	16.82	14.23	13.23	15.91	14.66	15.04	0.02

3.2.2 Model Results

With the finite element data available for processing, the need to organize the data into a state space model arises. To accomplish this, the data was accessed and written into a MATLAB environment using the ATA proprietary software package called IMAT. Reading the generated .op2 results file and saving the extracted MATLAB data package to the workspace, it is simply a matter of finding the necessary data and organizing it into the state space model derivation discussed. Using this state space formulation, the A and B matrices complete the modal system of equations which can be extended indefinitely for any number of known modes. In this case, a full model of 6 modes is obtained which leads to a 12 state system. The A matrix is constructed using diagonal matrices of ones, zeros, ω_n^2s, and $2\omega_n\zeta$s. The B matrix is constructed using the associated eigenvectors for each included mode based on the location of the control input actuator stingers on the FEM. This matrix maps a force input from the actuator into a modal force equivalent that directly affects the system states.
The C matrix is constructed using the eigenvectors of the derived system modes which map modal amplitude to output force at each of the four accelerometer locations on the FEM. The D matrix is constructed using the eigenvectors of the derived modes which map the modal force values to the output forces at each of the four accelerometer locations on the FEM.

3.2.3 Analysis of the System Modes/States

We will consider the full 12 state system for the following analysis of the FEA provided model. To start with, we want to identify the controllability, observatbility, and

Hankel singular value matrices of this system and determine if this model is suitable for closed loop control.

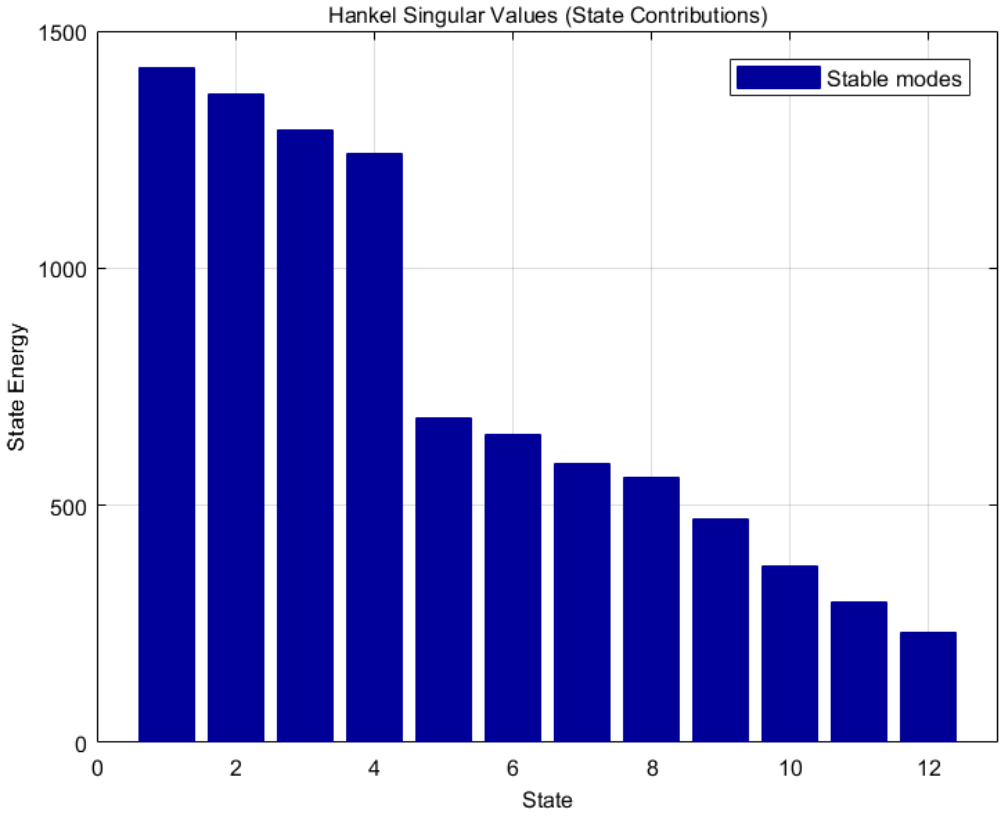

Figure 3.3: Hankel Singular Values.

Starting with the Hankel singular values, it is clear that the first four modes contribute the most to the overall input to output relation of this system. After the first four, there is a sharp dropoff followed by a steady decline. From plotting the singular values, it might be feasible to reduce this model to an eight or even four state realization. This will be done when formulating a model for control design.

Continuing, we will next calculate the controllability matrix and the observability matrices. In both cases, we find that the rank of these matrices is 11 instead of 12. This means that there is rank deficiency which indicates an unobservable and uncontrollable state. We note that the unobservable and uncontrollable mode are stable, and therefore the system is stabilizable and detectable [21].

One way to work around this unobservable/uncontrollable state is through balanced

truncation and reducing the number of states in the system. For instance, it is possible to reduce the states from 12 to 8 using a balanced truncation method of model order reduction. One key effect of this method however is that the dynamics of the system now become interlinked in the sense that the reduced modes now have dynamical properties from the higher order modes which have now been coupled with the new modes of the lower order realization. The process of model order reduction involves obtaining the ordered Hankel singular value matrix with associated eigenvectors. Then, by eliminating the eigenvalues below a certain threshold, a new set of state space matrices may be obtained which correspond to the reduced state space modes.

3.3 Uncertainty Modeling

Beginning with representing the plant in transfer function form, we obtain the following expressions for input j to output i for each mode k.

$$P_{i,j} = d_{i,j} + \sum_{k=1}^{r} \frac{b_{k,j}c_{i,k} + b_{k,j}c_{i,r+k}s}{s^2 + 2\zeta_k\omega_k + \omega_k^2}$$

These $b_{k,j}$, $c_{i,k}$, $c_{i,n+k}$, and $d_{i,j}$ terms are elements derived from the state space realization of the system. To further define these coefficients in terms of the modal components, a few more definitions will prove helpful. We utilize elements from the previously derived input and output eigenvectors with $v_{i,k} \in [\vec{v}_i] \in [V]$ and $v_{k,j} \in [\vec{v}_j]^* \in [V]^*$ respectively. Note that $[\vec{v}_i]$ will be horizontal while $[\vec{v}_j]^*$ is vertical. In addition, we define natural frequency values $\bar{\omega}_k \in \bar{\Omega}$ and mass values $\bar{m}_k \in \bar{M}$. Note that the generalized mass matrix yields values identity, so all individual mass values will be equal to 1. The damping terms follow a similar structure and are assigned based on the mode $\bar{\zeta}_k \in \bar{Z}$.

$$
\begin{aligned}
b_{k,j} &= [\bar{m}_k]^{-1}\hat{v}_{k,j} \\
c_{i,k} &= -\tilde{v}_{i,k}[\bar{\omega}_k^2] \\
c_{i,k+n} &= -2\tilde{v}_{i,k}[\bar{\zeta}_k][\bar{\omega}_k] \\
d_{i,j} &= \sum_{k=1}^{r} \tilde{v}_{i,k}[\bar{m}_k]^{-1}\hat{v}_{k,j} \\
d_{i,j,k} &= \tilde{v}_{i,k}[\bar{m}_k]^{-1}\hat{v}_{k,j}
\end{aligned}
$$

We can also express uncertainty in terms of a delta term $|\delta| \leq 1$ for each mode, noting that the maximum structured uncertainty for this plant will be determined through modeling and system identification methods for each mode. We therefore define a nominal $\bar{\omega}_k$ and express our actual frequency as $\omega_k = \bar{\omega}_k\,(1 + U_k\delta_k)$. We are also able to obtain a linearized ω_k^2 as $\omega_k^2 = \bar{\omega}_k^2\,(1 + 2U_k\delta_k)$. In this case we have represented the uncertainty coefficient for a particular mode as U_k, because we are modeling the structured uncertainty with a single δ term under the belief that all the system modes will deviate in a semi-linear fashion with respect to the physical interaction of adding mass loads to the wings. We will discuss this behavior later this chapter.

$$
\begin{aligned}
P_{i,j} &= [\vec{v}_i][\vec{v}_j]^* + \sum_{k=1}^{r} \frac{-v_{i,k}[\bar{\omega}_k^2]v_{k,j} - 2v_{i,k}[\bar{\zeta}_k][\bar{\omega}_k]v_{k,j}s}{s^2 + 2\bar{\zeta}_k\bar{\omega}_k + \bar{\omega}_k^2} \\
P_{i,j} &= \sum_{k=1}^{r} \left[\frac{v_{i,k}[s^2 + 2\bar{\zeta}_k\bar{\omega}_k s + \bar{\omega}_k^2]v_{k,j}}{s^2 + 2\bar{\zeta}_k\bar{\omega}_k + \bar{\omega}_k^2} + \frac{-v_{i,k}[\bar{\omega}_k^2]v_{k,j} - 2v_{i,k}[\bar{\zeta}_k][\bar{\omega}_k]v_{k,j}s}{s^2 + 2\bar{\zeta}_k\bar{\omega}_k + \bar{\omega}_k^2} \right] \\
P_{i,j} &= \sum_{k=1}^{r} \frac{v_{i,k}v_{k,j}s^2}{s^2 + 2\bar{\zeta}_k\bar{\omega}_k s + \bar{\omega}_k^2} \\
P_{i,j} &= \sum_{k=1}^{r} \frac{v_{i,k}v_{k,j}s^2}{s^2 + 2\bar{\zeta}_k\bar{\omega}_k s(1 + U_k\delta_k) + \bar{\omega}_k^2(1 + 2U_k\delta_k)} \\
P_{i,j} &= \sum_{k=1}^{r} \frac{v_{i,k}v_{k,j}s^2}{s^2 + 2\bar{\zeta}_k\bar{\omega}_k s + \bar{\omega}_k^2 + 2U_k(\bar{\zeta}_k\bar{\omega}_k s + \bar{\omega}_k^2)\delta_k}
\end{aligned}
\tag{3.17}
$$

From a modal coordinate perspective, each mode is independent of one another when it comes to individual contribution from input to output due to the diagonalization of normalized system matrices derived from the eigenvalue problem solution [16].

So, the modes can be isolated in this summation sequence. Denoting the plant transfer function from input j to output i through mode k, the individual modal transfer function can be expressed with three subscripts. We can obtain the components of our multivariable transfer function Q through algebraic manipulation which applies the same transformation of the Woodbury Matrix Identity to the 1×1 case.

$$
\begin{aligned}
P_{i,j,k} &= v_{i,k}\frac{\tilde{a}_{i,j,k}(s) + \tilde{b}_{i,j,k}(s)\delta_k}{\tilde{c}_k(s) + \tilde{d}_k(s)\delta_k}v_{k,j} \\
P_{i,j,k} &= v_{i,k}\tilde{a}_{i,j,k}(s)\left(\frac{1}{\tilde{c}_k(s)} - \frac{1}{\tilde{c}_k(s)}\right)\delta_k\left(\frac{1}{\tilde{d}_k(s)} + \frac{1}{\tilde{c}_k(s)}\delta_k\right)^{-1}\frac{v_{k,j}}{\tilde{c}_k(s)}... \\
&\quad + v_{i,k}\tilde{b}_{i,j,k}(s)\delta_k\left(\tilde{c}_k(s) + \tilde{d}_k(s)\delta_k\right)^{-1}v_{k,j} \\
P_{i,j,k} &= v_{i,k}\frac{\tilde{a}_{i,j,k}(s)}{\tilde{c}_k(s)}v_{k,j} + v_{i,k}\left(\tilde{b}_{i,j,k}(s) - \frac{\tilde{a}_{i,j,k}(s)\tilde{d}_k(s)}{\tilde{c}_k(s)}\right)\delta_k\left(1 + \frac{\tilde{d}_k(s)}{\tilde{c}_k(s)}\delta_k\right)^{-1}\frac{v_{k,j}}{\tilde{c}_k(s)} \\
P_{i,j,k} &= Q_{22}^{i,j,k} + \left(Q_{21}^{i,k}\right)\delta_k\left(1 + Q_{11}^{k}\delta_k\right)^{-1}Q_{12}^{k,j} \qquad (3.18)
\end{aligned}
$$

We note that $\tilde{b}_{i,j,k} = 0$ which simplifies the evaluation of Q from the listed quadrants in equation 3.18.

$$
\begin{aligned}
Q_{11}^{k} &= \frac{2U_k(\bar{\zeta}_k\bar{\omega}_k s + \bar{\omega}_k^2)}{s^2 + 2\bar{\zeta}_k\bar{\omega}_k s + \bar{\omega}_k^2} \\
Q_{12}^{i,k} &= \frac{v_{k,j}}{s^2 + 2\bar{\zeta}_k\bar{\omega}_k s + \bar{\omega}_k^2} \\
Q_{21}^{k,j} &= -\frac{v_{i,k}s^2 \cdot 2U_k(\bar{\zeta}_k\bar{\omega}_k s + \bar{\omega}_k^2)}{s^2 + 2\bar{\zeta}_k\bar{\omega}_k s + \bar{\omega}_k^2} \\
Q_{22}^{i,j,k} &= \frac{v_{i,k}v_{k,j}s^2}{s^2 + 2\bar{\zeta}_k\bar{\omega}_k s + \bar{\omega}_k^2}
\end{aligned}
$$

As discussed before regarding uncertainty structure, each individual modal frequency shifts under a somewhat common trend with respect to added weight such that a simplification can be made by assuming one δ which groups the individual modal δ_k terms under one umbrella variance term by explicitly assigning U_k coefficients to each individual transfer function. Because we have unified the modal components under a single δ term, we will assign one δ term to an identity matrix.

Expressing the total LFT in terms of two inputs, four outputs, and a single modeled mode, the structure will look like equation 3.19. The full LFT model is closed in

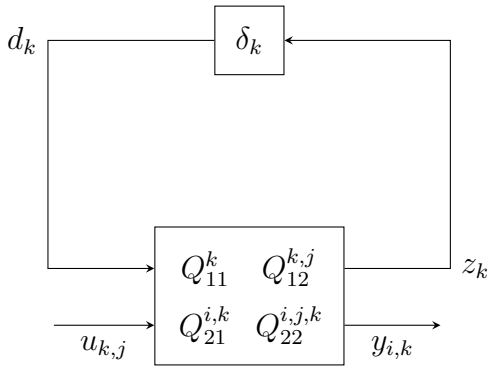

Figure 3.4: Generalized LFT Strucuture.

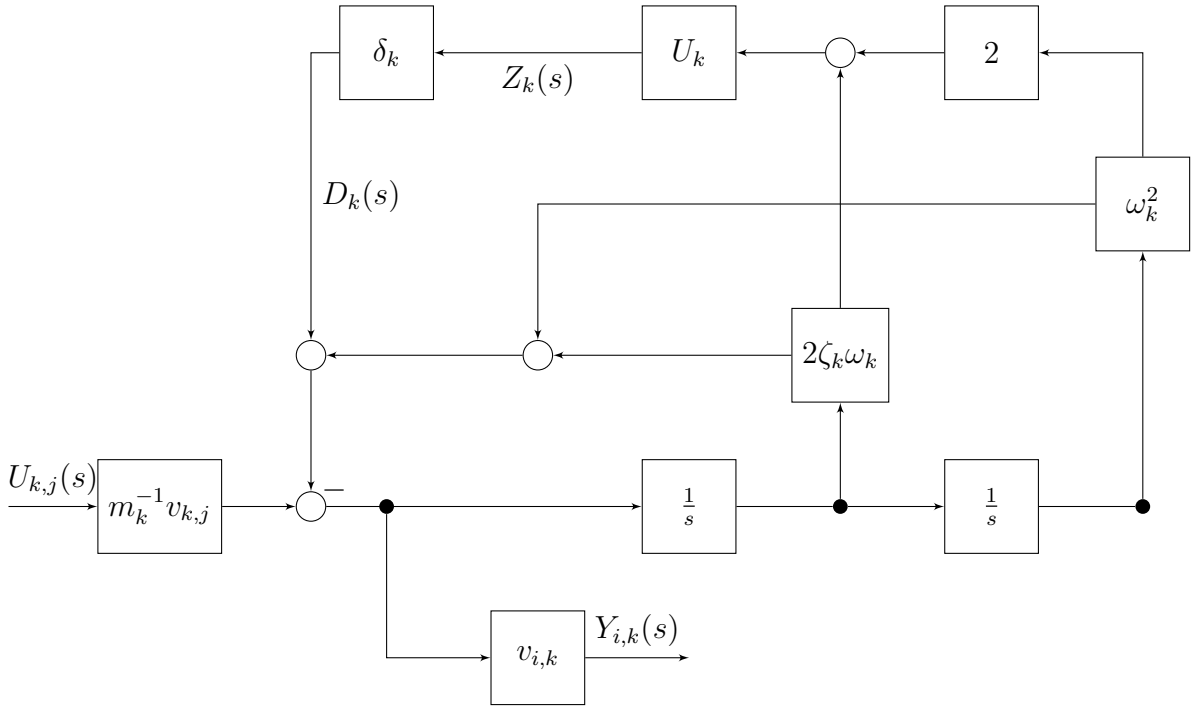

Figure 3.5: Block Diagram Representation of Uncertain Modal System.

feedback using standard notation, $F(A, \Delta)$ for closing A with Δ. In this case, $F(Q, \Delta)$ with $\Delta = \delta$ which results in the closed LFT per figure 3.6. Of course, by including additional modes, Q qill change based on the superposition of each modal contribution.

Extending the LFT to include each modal contribution as a separate signal with multiple z_k outputs and d_k inputs will look like figure A.18. In order to realize this, a diagonal structure of δ must be imposed wherein $\Delta = \delta \cdot I, \quad |\delta| \leq 1$. This diagonal structure will be utilized as the LFT structure for the purposes of comparing models and determining performance and stability robustness. We can actually formulate the Q transfer function in matrix form for all modes considered using the same manipu-

lation as before, except explicitly defining each modal component within a matrix . This derivation is left to appendix section C.1.

$$\begin{pmatrix} z_1 \\ y_1 \\ y_2 \\ y_3 \\ y_4 \end{pmatrix} = \begin{bmatrix} Q_{11}^{11} & Q_{12}^{11} & Q_{12}^{12} \\ Q_{12}^{11} & Q_{22}^{11} & Q_{22}^{12} \\ Q_{12}^{21} & Q_{22}^{21} & Q_{22}^{22} \\ Q_{12}^{31} & Q_{22}^{31} & Q_{22}^{32} \\ Q_{12}^{41} & Q_{22}^{41} & Q_{22}^{42} \end{bmatrix} \begin{pmatrix} d_1 \\ u_1 \\ u_2 \end{pmatrix} \tag{3.19}$$

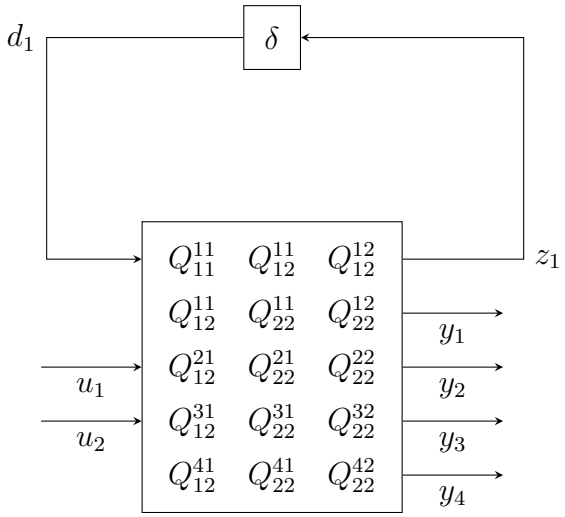

Figure 3.6: LFT structure with single disturbance.

3.3.1 LFT Formulation and Derived Uncertainty Description

For this study, we choose to measure the change in the natural frequencies of each mode with respect to the moment of the added mass in each configuration. This should yield a reasonable interpretation of structured uncertainty for each mode. We look back to the uncertainty LFT formulation in equation 3.17 and update the expression based on measured data of our system.

In this case, we denote an index i for output number, j for input number, and k for mode number. The equation is in terms of modal natural frequencies ω_k, damping ratios ζ_k, uncertainty coefficient U_k, and the correct state space coefficients from B, C, and D. The uncertainty coefficients are obtained by calculating the frequency over all the configurations and obtaining the maximum percentile change from the nominal frequency. This was done via spectral analysis of the frequency responses of the system

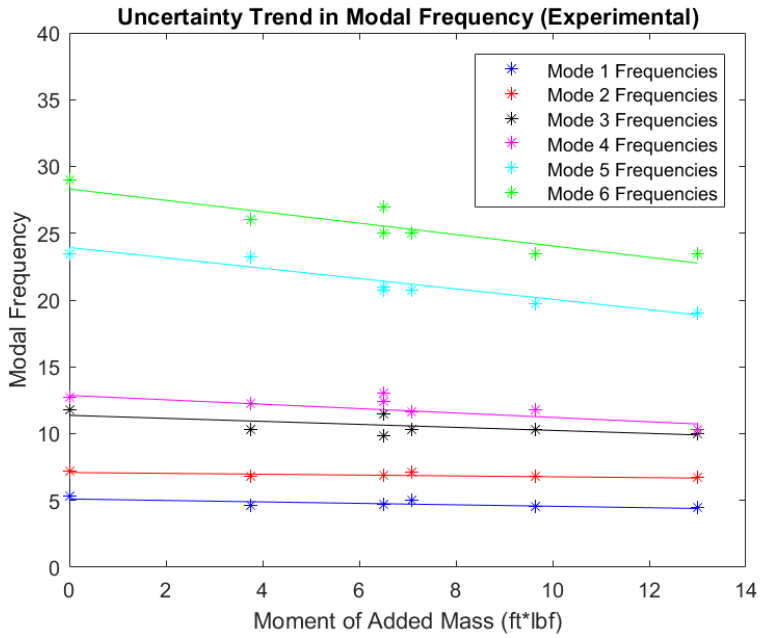

Figure 3.7: Variance in Natural Frequency with Added Mass from Experimental Data.

to chirp input signals and white noise input signals under the different mass-loading configurations. Taking all the data together, a trend was linearized with respect to increasing moment on the wing taken from the centerline of the fuselage through a least squares minimization calculation per equation 3.20.

$$\theta_k = \begin{pmatrix} a_k \\ b_k \end{pmatrix} = \begin{pmatrix} 7 & \sum_{p=0}^{6} \tau_{k,p} \\ \sum_{p=0}^{6} \tau_{k,p} & \sum_{p=0}^{6} \tau_{k,p}^2 \end{pmatrix}^{-1} \begin{pmatrix} \sum_{p=0}^{6} \omega_{k,p} \\ \sum_{p=0}^{6} \tau_{k,p}\omega_{k,p} \end{pmatrix} \tag{3.20}$$

However, the mass loadings vary between leading edge and trailing edge loading. Since the moment of the mass from the centerline of the fuselage remains the same, the loading difference will affect the torsional modes much greater than the bending modes. In this regard, we obtain only an approximation of a trend in uncertainty for all six modes with regards to a single umbrella delta term. From the experimental linear fit, we obtain values for the first six modal uncertainty coefficients. We also obtain uncertainty coefficients for the model based linear fits. The plots of these fits are shown in figure 3.7.

$$U_{exp} = [-0.1387,\ -0.0588,\ -0.1289,\ -0.1662,\ -0.2106,\ -0.1957]$$
$$U_{mod} = [-0.3483,\ -0.1897,\ -0.3633,\ -0.3591,\ -0.4094,\ -0.3945]$$

We note in the experimentally derived coefficients that we expect a maximum of 21% deviation in the modal natural frequency value whereas we might expect up to a 41% shift in modal frequency for the model derived uncertainty. For control design and validation, we will choose to compare to the experimentally derived structure.

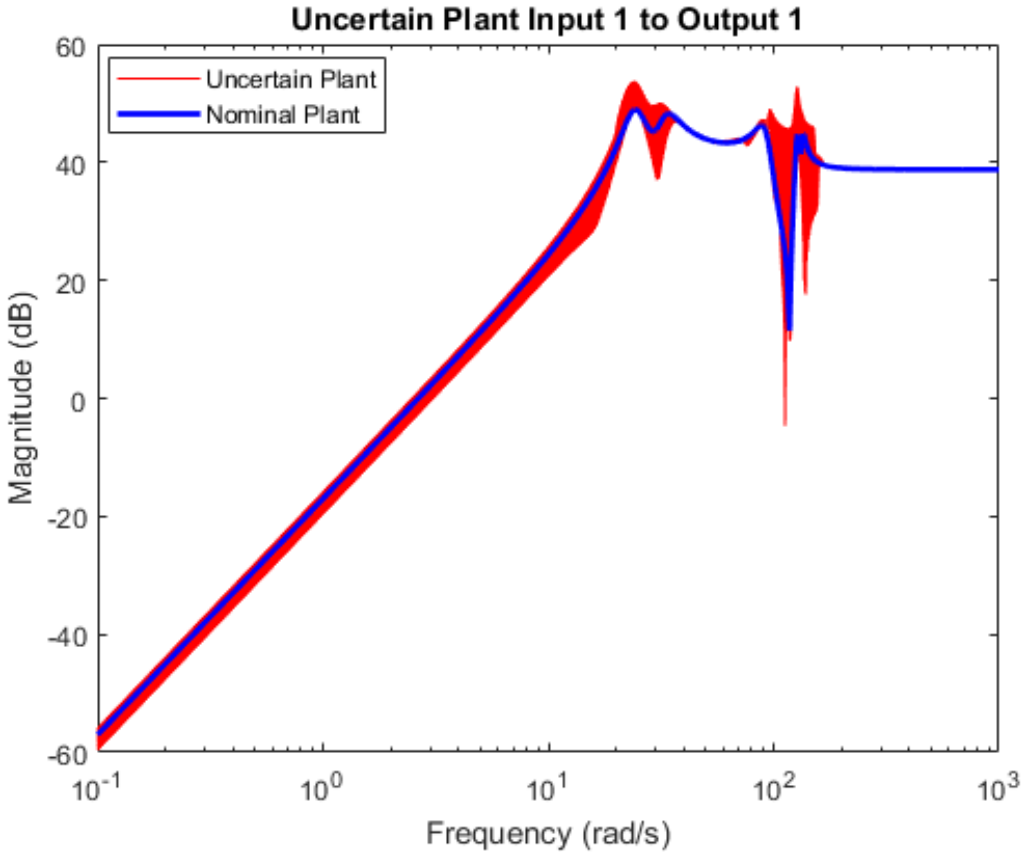

Figure 3.8: Modeled LFT Uncertainty Bode Plot.

Combining the experimentally-derived uncertainty coefficients with each of the modal damping and natural frequency terms along with the appropriate eigenvector data matching each mode to input/output allows for us to build an uncertainty model to truly test the robustness limits of our controller designs.

The modal, input, and output data is applied to equation 3.17 to obtain an extended Q matrix for use in expressing an LFT. Upon closing the LFT, the uncertainty description portrays the different mass loading conditions for each $|\delta| \leq 1$ and is shown graphically via bode plot in figure 3.8. The uncertainty description also accounts for the negative mass loading condition in which the natural frequencies of the modes begin to increase instead, thus making the model twice as conservative as necessary

in theory. However, this turned out to be beneficial due to the discrepancy between model and physical system as the experimental results will show. However, it also means that any sort of H_∞ optimized controller for this LFT model will be required to cover a broad variance in uncertainty such that the closed loop performance will be optimized over the entire spectra of shifting frequencies.

Using this new uncertainty model to assess the performance of each controller design. We intend to validate a linear quadratic design, a linear quadratic design with high frequency rolloff, and a mixed sensitivity design. If we intend to focus more on nominal performance with the linear quadratic design and more with stability robustness with the mixed sensitivity, we should obtain the best robust stability and robust performance with the mixed sensitivity design when we test the off-nominal configurations.

Chapter 4

Controls

In this chapter, we will go through the controller design process by reviewing some of the derivations from standard literature to give context for the control designs used for implementation on the Iron Bird System.

4.1 Building the Controller

For this experiment, we consider a classic control design approach by modeling the Iron Bird as an LTI system with actuator inputs producing a force on the wings and accelerometer outputs reading acceleration at the wingtips. Thus, for a simple open loop block diagram, we generalize the input to output dynamics with a plant transfer function with a block diagram representation in figure 4.1.

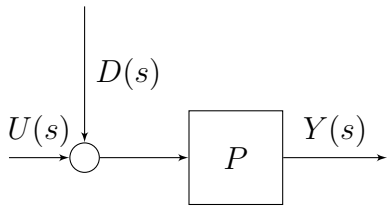

Figure 4.1: Open Loop System

By generalizing this as an LTI sytem, we can employ linear control modeling methods to derive a state space realization of the system. This is an especially important process for eventual MIMO control design with linear-quadratic related methods and linear matrix inequality problem formulations. We see in figure 4.2 a block diagram representation of the open loop process with state space A, B, C, and D matrices.

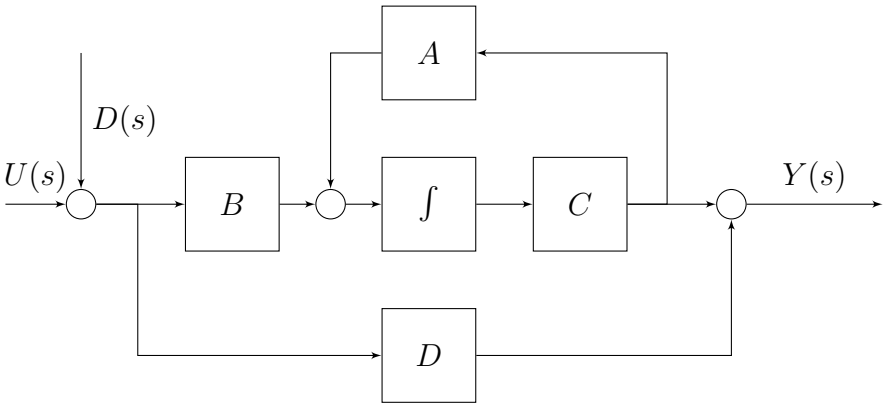

Figure 4.2: Open Loop System State Space

$$\dot{x} = Ax + Bu$$
$$y = Cx + Du$$

With a state space realization of our system, it now makes sense to employ a standard linear quadratic design methodology to derive a MIMO controller design. We accomplish this through the formulation of an infinite horizon cost function which we intend to minimize. We note that in closed loop, we define the input in terms of state feedback $u(t) = Kx(t)$.

$$\begin{aligned} J &= \int_0^\infty \left(x(t)^* Q x(t) + u(t)^* R u(t)\right) dt \\ &= \int_0^\infty x(t)^* \left(Q + K^* R K\right) x(t) dt \\ &= x_0^* X x_0 \end{aligned}$$

In this case, X represents the solution of a corresponding Lyapunov equation. By isolating the K term of the equation, one choice of K can be utilized to reduce the equation further.

$$(A+BK)^*X + X(A+BK) + Q + K^*RK = 0, \quad R > 0$$
$$A^*X + XA - XBR^{-1}B^*X + Q + (XBR^{-1} + K^*)R(R^{-1}B^*X + K) = 0$$
$$K = -R^{-1}B^*X$$

With this optimal choice of K, we obtain the Algebraic Ricatti Equation ARE for X. The result of this choice in K and X is such that $A+BK$ is Hurwitz and the cost function J is minimized.

$$A^*X + XA - XBR^{-1}B^*X + Q = 0$$

With this in mind, we satisfy all necessary conditions to solve the state feedback problem formulation in such a way to stabilize the close loop system (open loop already stable) and minimize the cost function based on two separate covariance matrices, Q and R. With this convenient problem formulation, we treat these two matrices as design parameters to adjust the expected closed loop system performance.

With our selection of Q, we can adjust the weighting placed on the associated state deviation. If we emphasize minimization of state deviation, more control authority is required to drive the system to the necessary dynamical response. Conversely, if we wish to limit the control input, perhaps to avoid saturation, then we utilize the weighting placed on R. Balancing these two will mean a tradeoff between nominal performance and control input. In the case of this system, there is no issue of ensuring stability, it comes down to the amount of added damping into the closed loop response to attenuate modal disturbance. Ideally, we would like to obtain good added damping across all modes which are included in the control model.

Now, consider the state space model with sources of noise.

$$\dot{x} = Ax + Bu + w$$
$$y = Cx + Du + v$$

We also need to determine a way to filter out the effects of noisy outputs and noise in the process associated with states. To this end, we employ a framework to develop an optimal state estimator.

$$\dot{\hat{x}} = A\hat{x} + Bu + L(y - \hat{y})$$
$$\hat{y} = C\hat{x}$$

Due to the separation principle, we can design the state feedback gain and the observer feedback gain separately then combine them afterwards taking the union of eigenvalues for the complete system.

$$eig_{sys} = eig(A + BK) \cup eig(A + LC)$$

For this estimator problem formulation, we will invoke knowledge of complementary systems and duality to reformulate the estimator problem in a similar structure to regulator problem, except using the transpose of matrix A and the transpose of matrix C in place of matrix A and matrix B respectively. For this problem, the desired result is some observer matrix L which minimizes an associated cost function in terms of the state error and the output covariance matrices.

We define the covariance for both the output noise $v(t)$ and the process noise $w(t)$. We note that the output noise and process noise are independent and uncorrelated white noise signals.

$$E(w(t)^* w(t)) = W\delta$$
$$E(v(t)^* v(t)) = V\delta$$
$$E(w(t)^* v(t)) = 0$$
$$w(y) \approx \mathcal{N}(0, W)$$
$$v(t) \approx \mathcal{N}(0, V)$$

We can define the cost function in terms of the expected value of the square of the state error. This allows us to conveniently define asystem to formulate a Lyapunov equation which we can utilize to solve for an optimal observer gain.

$$e = x - \hat{x}$$
$$z = y - \hat{y}$$
$$\dot{e} = (A + LC)e$$

We can form a cost function in similar fashion.

$$J = \int_0^\infty (e^*(t)We(t) + z^*(t)Vz(t))\, dt$$

With the new solution Y to the Lypaunov equation defined, we now express the equation and determine the optimal L to obtain an ARE.

$$\begin{aligned}(A + LC)Y + Y(A + LC)^* + W + LVL^* = 0, \quad V > 0 \\ AY + YA^* + W + LCY + YC^*L^* + LVL^* = 0 \\ L = -YC^*V^{-1} \\ AY + YA^* + W - YC^*V^{-1}CY = 0\end{aligned}$$

Now, with an optimal observer gain and an optimal regulator gain, we can formulate a state space system which includes an estimator and a state variable feedback gain.

With a linear quadratic closed loop state space system defined, we can go about testing and validating the expected closed loop dynamics from a designed model in simulation with the implementation of the final controller onto the Simulink Realtime environment which interfaces with the DAQ system of the Iron Bird. Taking the final K and L matrices, we can formulate a controller by constructing a new LTI system with the measurement outputs y as controller inputs and the system inputs u as the controller output.

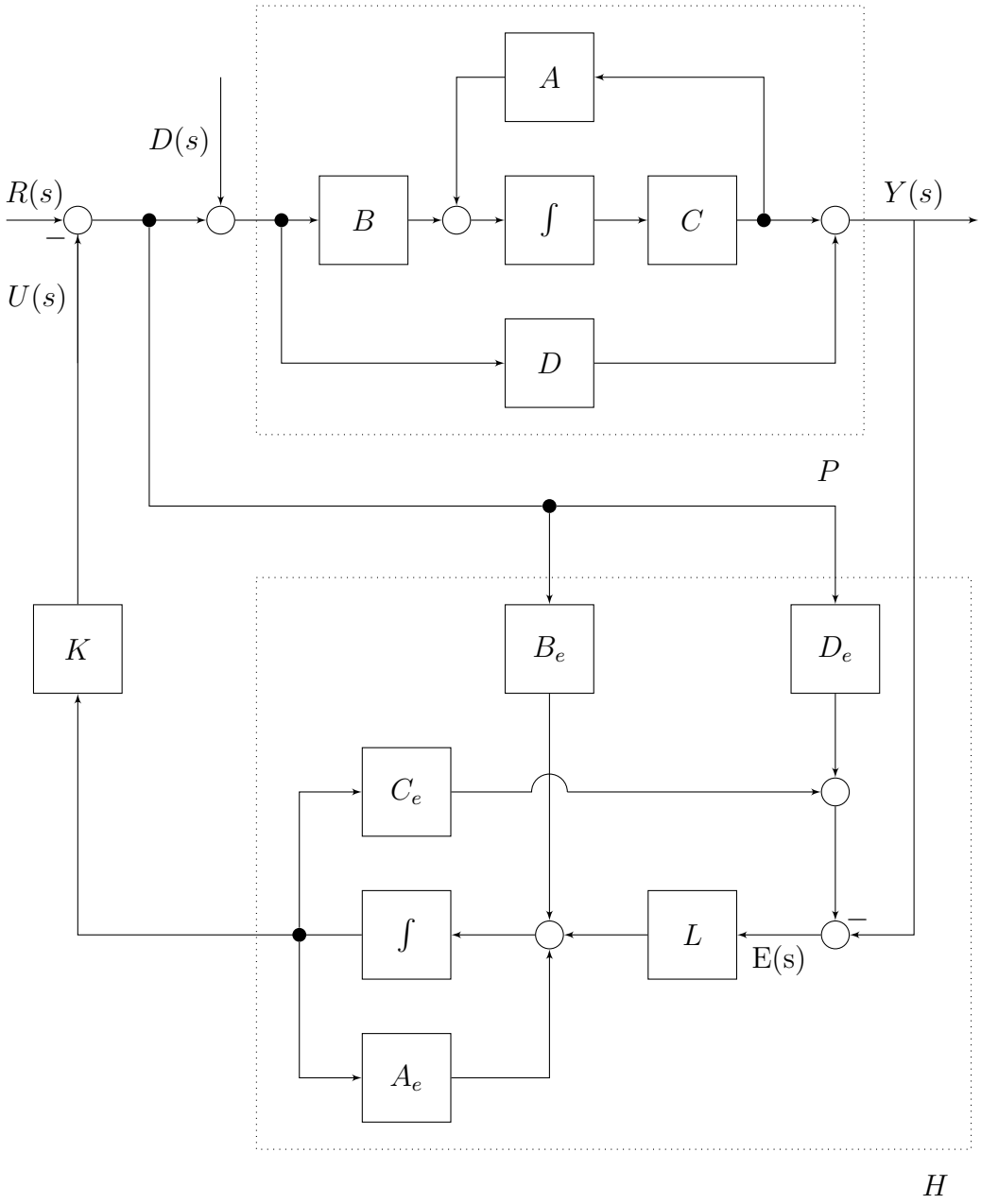

Figure 4.3: Closed Loop LQG System.

$$\dot{\hat{x}} = (A - BK - LC)\hat{x} + Ly$$
$$u = -K\hat{x}$$

We also want to ensure that this disturbance rejection controller is not affected by the aircraft dynamics during an extended maneuver where during which a pilot needs to utilize control authority. To this end, we implement a high pass filter to reject static

changes and offset drifts (like those observed from the accelerometers). This behaves as a washout filter. Note that the rigid body modes are calculated at around $1Hz$ or below, so having a cutoff frequency at around $3Hz$ will provide some separation from the rigid body effects.

$$G = \frac{s}{s+1} \tag{4.1}$$

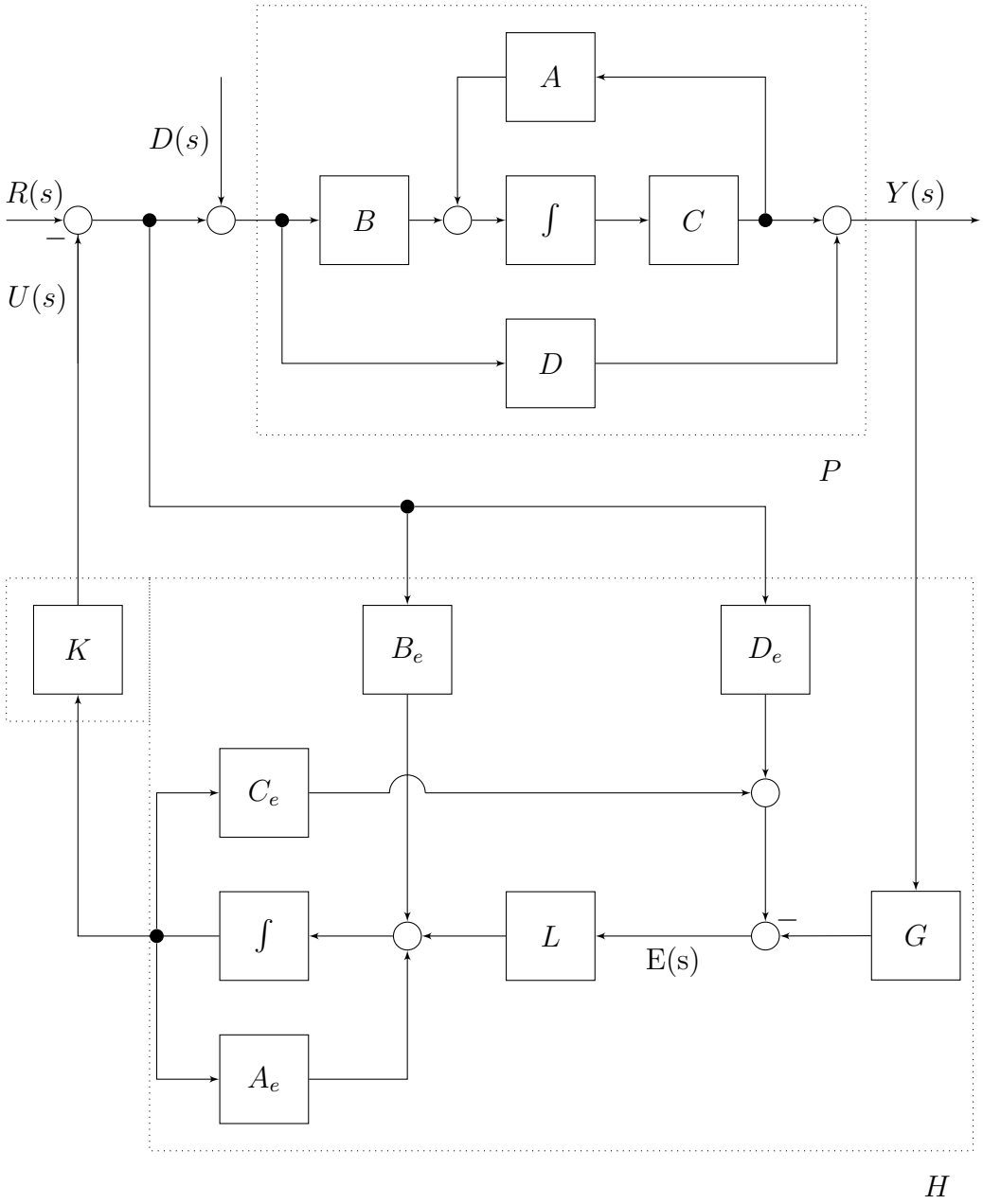

Figure 4.4: Closed Loop LQG System with Washout Filter (G).

Throughout many of these controller implementations, there arises a need to im-

plement a high frequency rolloff filter to add robustness to the high frequency modal disturbances [20]. In order to accomplish this, the high frequency rolloff filter R needs to be included within the plant of the model during the controller design process. Once the new controller is obtained $\bar{K}$, the filter R is moved from the plant and grouped with the controller to obtain the true controller K.

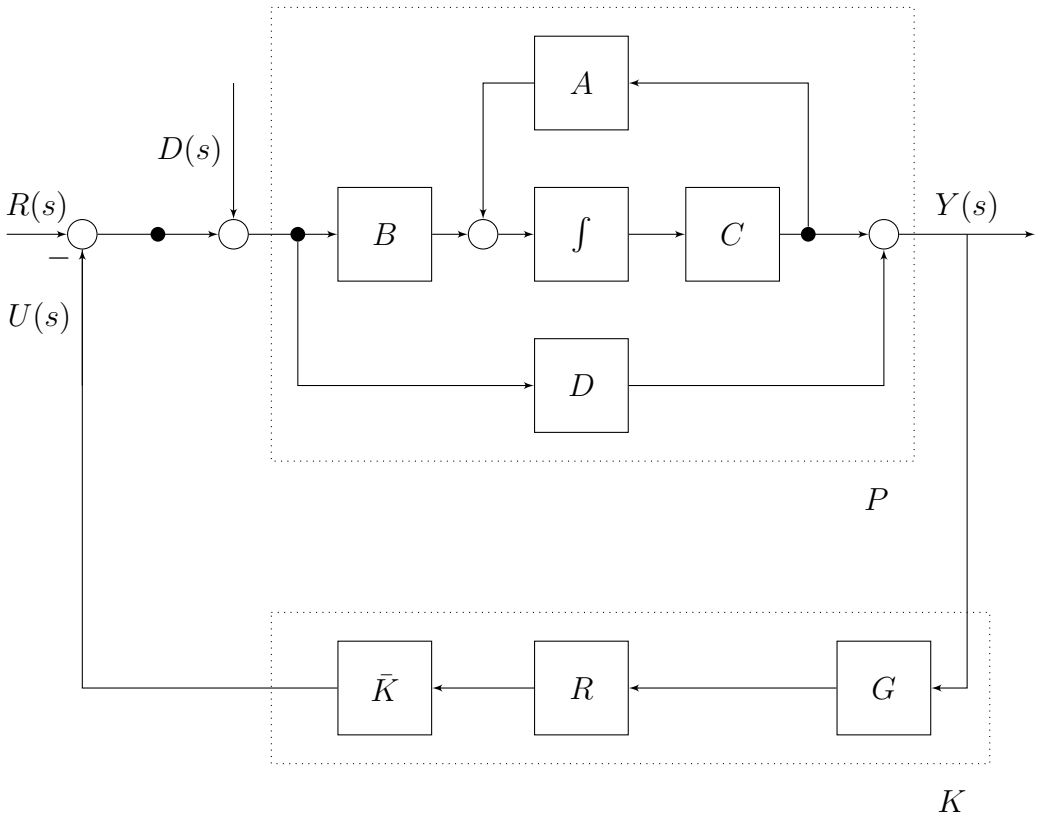

Figure 4.5: Control Structure with High Frequency Rolloff Filter (R) and Washout Filter (G).

4.2 First Bending Mode Controller Designs

For the series of experiments to follow, three controller designs were implemented and tested. These three controllers were modeled based on a truncated version of our full model consisting of the first two modes, the symmetric and the asymmetric first wing bending modes.

$$A = \begin{pmatrix} 0 & 0 & 1 & 0 \\ 0 & 0 & 0 & 1 \\ -\omega_1^2 & 0 & -2\zeta_1\omega_1 & 0 \\ 0 & -\omega_2^2 & 0 & -2\zeta_2\omega_2 \end{pmatrix} \quad B = \begin{pmatrix} 0 & 0 \\ 0 & 0 \\ v_{1,1}^{in} & v_{1,2}^{in} \\ v_{2,1}^{in} & v_{2,2}^{in} \end{pmatrix}$$

$$C = \begin{pmatrix} -v_{1,1}^{out}\omega_1^2 & -v_{1,2}^{out}\omega_2^2 & -v_{1,3}^{out}2\zeta_1\omega_1 & -v_{1,4}^{out}2\zeta_2\omega_2 \\ -v_{2,1}^{out}\omega_1^2 & -v_{2,2}^{out}\omega_2^2 & -v_{2,3}^{out}2\zeta_1\omega_1 & -v_{2,4}^{out}2\zeta_2\omega_2 \\ -v_{3,1}^{out}\omega_1^2 & -v_{3,2}^{out}\omega_2^2 & -v_{3,3}^{out}2\zeta_1\omega_1 & -v_{3,4}^{out}2\zeta_2\omega_2 \\ -v_{4,1}^{out}\omega_1^2 & -v_{4,2}^{out}\omega_2^2 & -v_{4,3}^{out}2\zeta_1\omega_1 & -v_{4,4}^{out}2\zeta_2\omega_2 \end{pmatrix} \quad D = \begin{pmatrix} \sum_{k=1}^{4} v_{1,k}^{out}v_{k,1}^{in} & \sum_{k=1}^{4} v_{1,k}^{out}v_{k,2}^{in} \\ \sum_{k=1}^{4} v_{2,k}^{out}v_{k,1}^{in} & \sum_{k=1}^{4} v_{2,k}^{out}v_{k,2}^{in} \\ \sum_{k=1}^{4} v_{3,k}^{out}v_{k,1}^{in} & \sum_{k=1}^{4} v_{3,k}^{out}v_{k,2}^{in} \\ \sum_{k=1}^{4} v_{4,k}^{out}v_{k,1}^{in} & \sum_{k=1}^{4} v_{4,k}^{out}v_{k,2}^{in} \end{pmatrix}$$

4.2.1 Linear-Quadratic-Gaussian

The first is a linear-quadratic-Gaussian (LQG) design with standard cost function formulation. The estimator is designed by first establishing the noise covariance in the system after measuring a zero input signal from each output. This covariance is then implemented into the simulation environment, and the simulated system is given a step disturbance with no control input. The response of the state estimation is then tuned accordingly using the state covariance weighting matrix until a reasonable response is found, balancing between settling time and steady state robustness to noise.
With the regulator design, we want to create something which focuses on optimal performance by balancing the state covariance to penalize deviation from zero and the control input covariance to saturate control effort only in the worst case conditions. The modal amplitude is weighted more than the modal velocity.

The regulator is balanced according to an acceptable level of control input. The idea is to maximize the control effort when the system experiences precise resonance according to its model simulation. Therefore, the input covariance is balanced against the state covariance to make sure the control effort avoids saturation to all but the worst disturbances, per the modeled modal dynamics.

$$Q = diag(25000,\ 25000,\ 10,\ 10)$$

$$R = diag(1,\ 1)$$

The estimator of this controller is designed using measured noise covariance of each accelerometer and balanced against the state covariance using simulation to get a reasonable estimator response to a disturbance input.

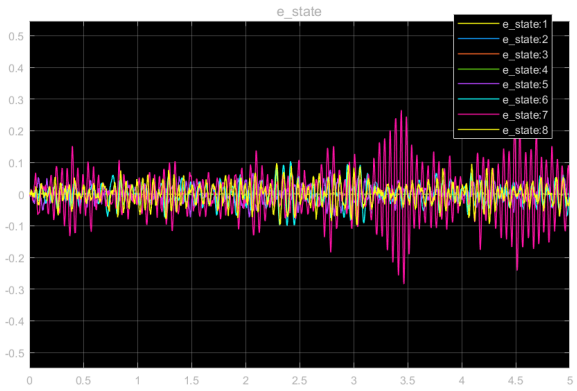

Figure 4.6: State error from white noise in measurements during simulation.

$$W = 10^{-8} \cdot diag(1,\ 1,\ 1,\ 1)$$

$$V = 10^{-3} \cdot \begin{pmatrix} 0.7110 & 0.0513 & 0.0931 & 0.0809 \\ 0.0513 & 0.5971 & 0.0125 & 0.0360 \\ 0.0931 & 0.0125 & 0.6288 & 0.0416 \\ 0.0809 & 0.0360 & 0.0416 & 0.7301 \end{pmatrix}$$

It should be noted that the noise covariance matrix is determined experimentally from sampling output noise over time, and the covariance units are based on the voltage signal rather than the in/s^2 signal. In this case, we are just balancing the two covariance matrices against one another, so they can both be scaled appropriately as needed.

Combining the estimator and the regulator into a single LQG regulator, the resulting controller attempts to achieve a rather ambitious level of damping in the system, theoretically increasing the lowest damped pole by a factor of 4. The controller is designed in continuous time then converted to discrete time using a zero order hold approximation.

Overall, this is a reasonable controller design for a nominal system, however this remains a dubious proposition in light of the higher order modes neglected.

4.2.2 Linear Quadratic-Gaussian with High Frequency Rolloff

The second design utilized the same weighting matrices of the previous LQG design, but this time a high frequency rolloff filter is implemented in an attempt to gain

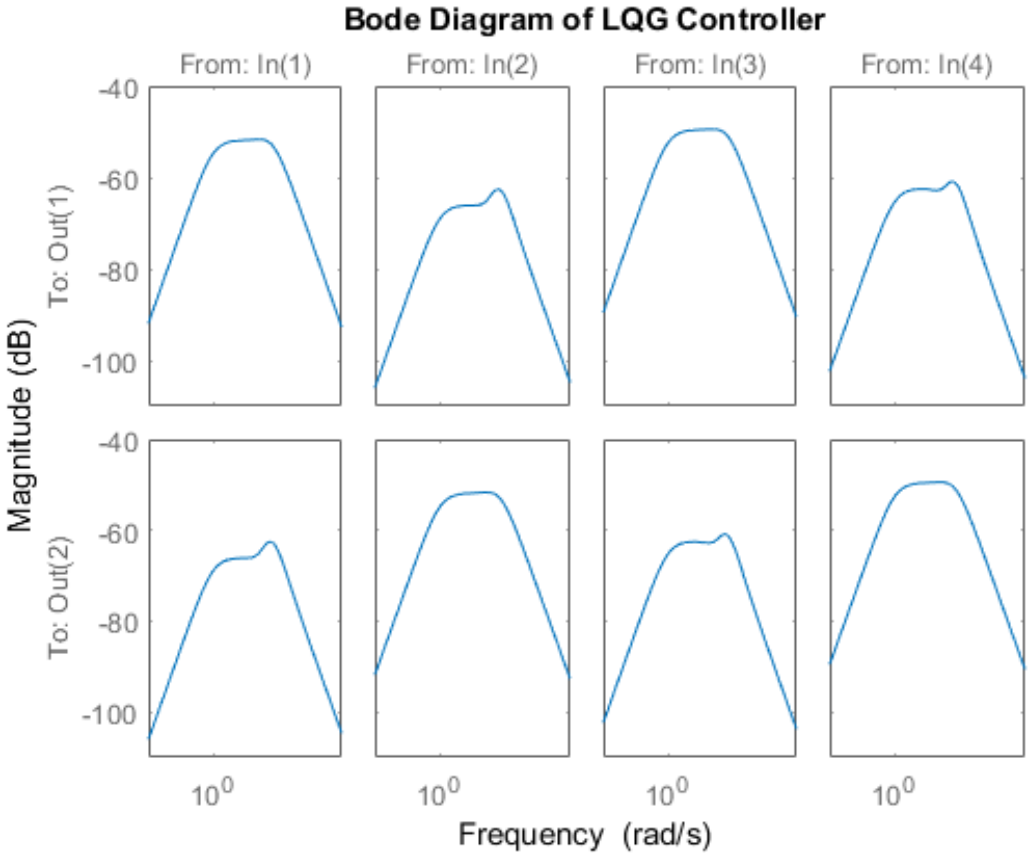

Figure 4.7: Bode Response of LQG Controller.

robustness against higher frequency disturbances from noise or higher order modes. The main idea to to control the bandwidth of the controller so as not to heighten control sensitivity near the unmodeled higher frequency dynamics of the system.

For added robustness, the next control design features the same LQG design as described previously, but this features an added high frequency rolloff filter $F = \frac{40}{s+40}$ to minimize the effects of excluded higher frequency modes on the controller performance.

Utilizing the same weighting matrices as before, the controller is rebuilt using a first order high frequency rolloff filter with 40 rad/s as the cutoff frequency. The plant is redefined to include the filter, $\bar{P} = P \cdot F$. The filter is then moved from the plant to the derived controller to obtain the final controller form, $K = \bar{K} \cdot F$. The block diagram for this design is represented in figure 4.5 with one key distinction being that $\bar{K}$ encompasses the combined regulator and estimator controller.

The filtered LQG controller (LQGF) is able to achieve these design goals with some degree of success. Observing the resulting lowest damped pole, the closed loop

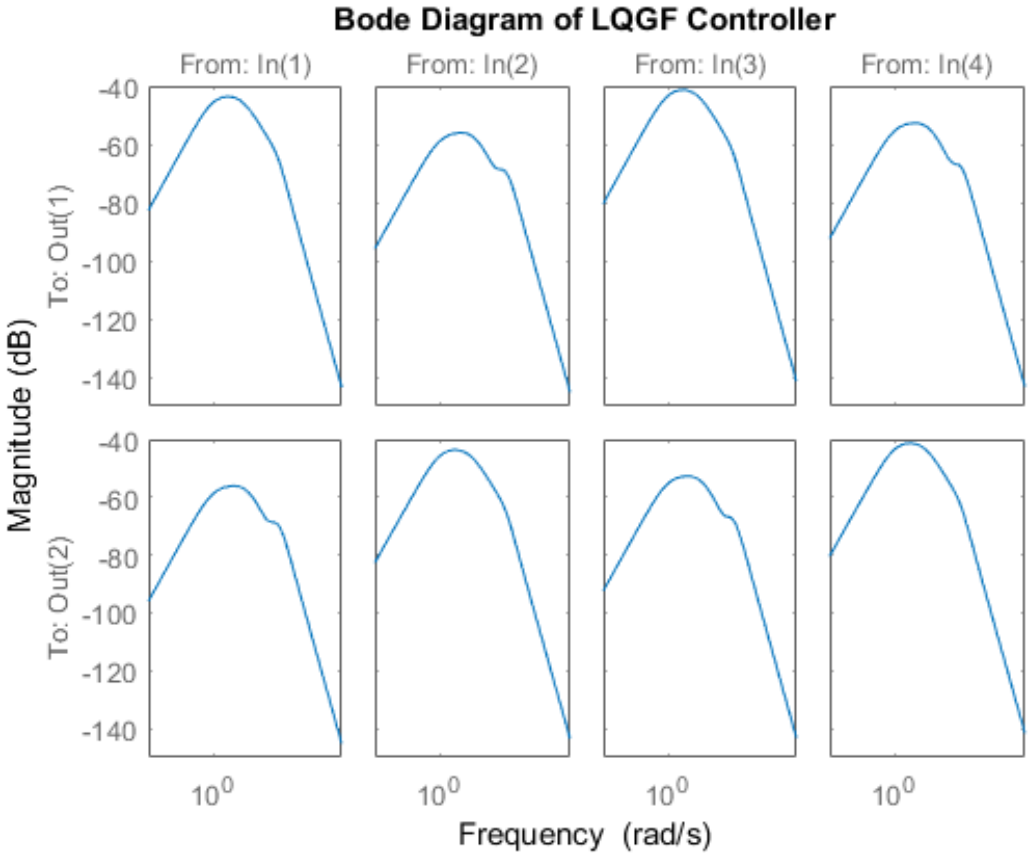

Figure 4.8: Bode Response of LQG Controller with High Frequency Rolloff.

LQGF system actually attempts an even more highly damped system than that of the LQG closed loop system. However, we note that the controller drops off sensitivity at higher frequencies thus achieving the aim of our design. With knowledge that higher modes exist, we hope that this rolloff will add robustness in our design over the initial LQG controller.

4.2.3 Mixed Sensitivity

The third controller utilizes a mixed sensitivity control design approach [30] in which frequency dependent weighting functions are selected in order to strategize tradeoffs in sensitivity to error, control sensitivity, and robustness in the system. With this approach, the reduced plant is simple enough to implement an inverse weighting matrix, W_0, which heightens sensitivity in the frequency band containing the two modeled modes. A fourth order weighting function is used which acts as an inverted band stop filter. Utilizing this weighting function, the next step is to determine how

best to weight the system's sensitivity to nominal performance using W_1. For this implementation, it is simpler to leave this as an identity matrix and balance W_0 against W_2. With the final weighting function, the aim is to balance the control sensitivity of the system. Therefore, this weighting matrix is adjusted against W_0 such that the H_∞ norm of the weighted system sensitivity and weighted control sensitivity remains below 1. The aim of these weightings is to obtain a closed loop system which displays decent margins in terms of robust stability and robust performance. We note that in the design phase of this controller, we are comparing to truncated version of the model so we cannot guarantee the same levels or robust stability and performance on the higher order model or real system.

The weighting functions are applied to the plant in such a way to formulate a linear fractional transformation matrix, Q. This formulation features two control inputs, u, and two disturbance inputs, w. The formulation also features four measurement outputs, y, a weighted input signal, e_1, and a weighted output signal, e_2.

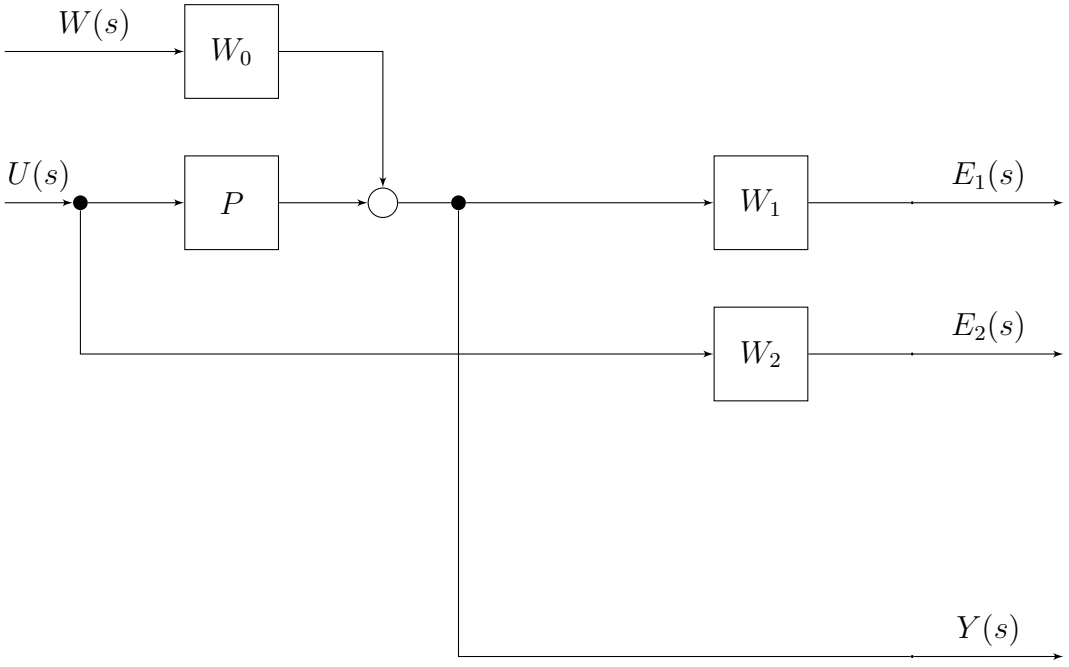

Figure 4.9: Mixed Sensitivity Weighted System

We should hopefully expect increased robustness from this mixed sensitivity design over the initial LQG design and maybe over the LQGF design as well.

We now begin to formulate the LFT problem formulation by structuring an extended Q matrix which we will close using a Δ structure.

$$Q = \begin{pmatrix} W_1 W_0 & W_1 P \\ 0 & W_2 \\ W_0 & P \end{pmatrix}$$

Thus, the optimal controller may be calculated by minimizing the $H\infty$ norm of the closed loop performance criterion after forming the LFT with Q using $-K$ in feedback following the standard $F(A, \Delta)$ notation.

$$||F(Q, -K)||_\infty = \left|\left| \begin{matrix} W_1(1+PK)^{-1}W_0 \\ W_2K(1+PK)^{-1}W_0 \end{matrix} \right|\right|_\infty$$

For this design, W_0 is a frequency dependent weighting matrix which acts as an inverse band stop filter along the frequency interval containing the first two modes. W_1 is kept as identity, and W_2 is an inverted low pass filter to increase control effort penalty on higher frequency ranges.

$$\begin{aligned} W_0 &= \frac{0.65s^2 + 26s + 65}{s^2 + 100s + 100} \cdot I \\ W_1 &= I \\ W_2 &= \frac{1000s + 1000}{s + 1000} \end{aligned}$$

The desired controller K_{MS} is obtained through a linear matrix inequality formulation involving the state space realization of the derived LFT. The optimization problem can be expressed through the minimization of the H_∞ norm of the performance weights.

$$\begin{aligned} K_{MS} &= \inf_K ||F(Q, -K)||_\infty \\ F(Q, -K) &= \begin{bmatrix} \tilde{A} & \tilde{B} \\ \tilde{C} & \tilde{D} \end{bmatrix} \end{aligned}$$

By the bounded real lemma [19], we can show that $||F(Q, -K)||_\infty < \gamma$ and $\tilde{A}$ is Hurwitz if $\exists X = X^*$ which satisfies an ARE. We can construct the ARE problem as an LMI minimization problem, because the goal is to achieve $\inf_\gamma \{||F(Q, -K)||_\infty < \gamma\}$.

$$\begin{bmatrix} X\tilde{A} + \tilde{A}X^* & X\tilde{B} & \tilde{C}^* \\ \tilde{B}^*X & -\gamma I & \tilde{D}^* \\ \tilde{C} & \tilde{D} & -\gamma I \end{bmatrix} < 0, \quad X > 0$$

Once we formulate this controller optimization problem, we modify it to include the washout and high frequency rolloff filters in the design.

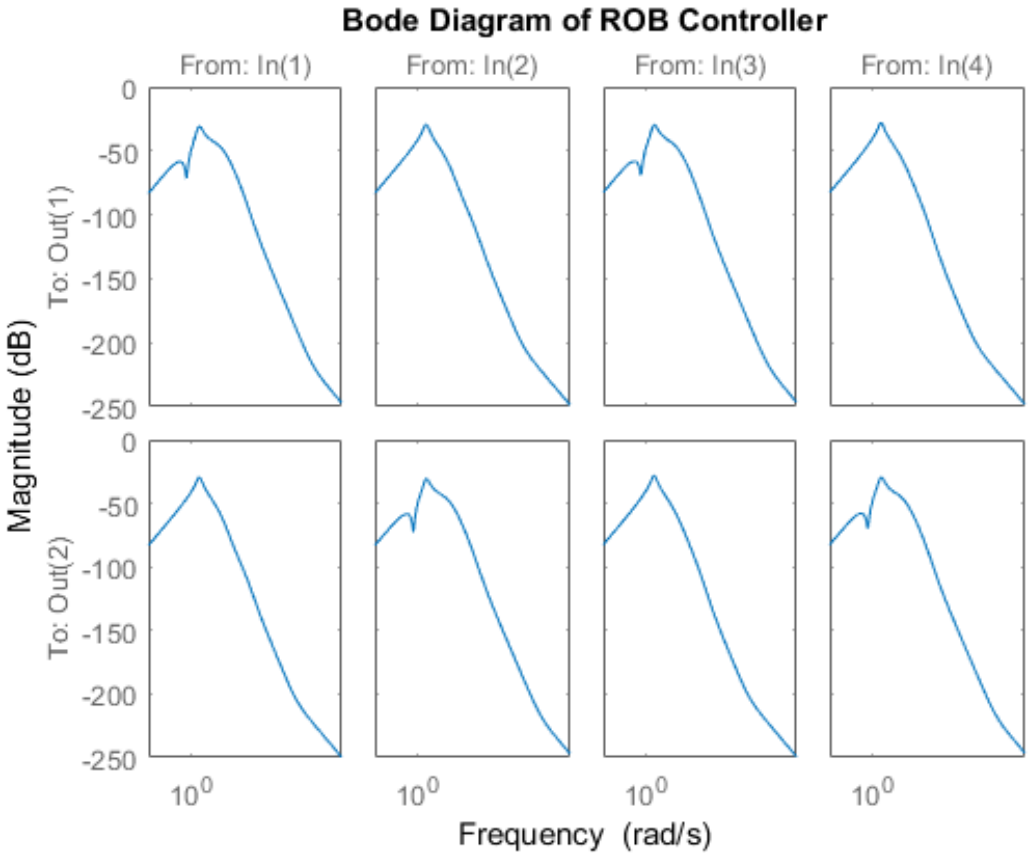

Figure 4.10: Bode Response of Mixed Sensitivity Controller.

For this experiment, we obtain a controller which yields a $\gamma < 0.65$. The controller response acts in a very narrow band of frequency correlating to the specified modal frequency range as seen in figure 4.10. Thus, the controller does not adversely impact the higher frequency modes due to a more confined sensitivity region, especially compared to the initial LQG design.

4.3 Other Control Designs

With knowledge of the system from experimental testing and an understanding that an LQR formulation will likely need to be rather conservative in light of the uncertainty description, we can re-formulate a linear-quadratic controller with a regulator design that will prove more robust. Then, we can take this nominal sensitivity function from the closed loop of the linear-quadratic design and pose this as an inverse weighting function to achieve a new frequency weighted H_∞ minimized design.

4.3.1 Linear-Quadratic Revisited

We start by including the second pair of modes into our model for control design. Thus, we are now modeling the first symmetric and asymmetric wing bending modes and the first symmetric and asymmetric torsional modes, bringing our control model up to 4 modes, or 8 states.

Then, we adjust the weighting matrices of Q and R so as to balance robustness with nominal performance. By reframing the optimization problem to balance robustness with performance in a linear-quadratic sense, we are able to tune the controller to achieve similar qualities found in the previous mixed sensitivity design. We keep the washout filter included in all designs to follow.

4.3.2 Linear-Quadratic with High Frequency Rolloff Revisited

Utilizing the design framework as before, we now add a high frequency rolloff filter, except we adjust the rolloff frequency to a higher value so as to not interfere with the desired range of frequency for control implementation. The filter itself will now have the form $F = \frac{140}{s+140}$ with cutoff frequency at $140 rad/s$.

4.3.3 Inverted Nominal Sensitivity Weighting

We now reformulate the mixed sensitivity design problem, except we utilize the sensitivity function of new linear-quadratic closed loop design for our 4 mode model as our primary inverted dynamics weighting. Therefore, we define the sensitivity function of the closed loop linear-quadratic design as S_{LQ} and choose our weightings appropriately. We note that we adjust certain weightings in order to obtain an appropriate

singular value bound with $\gamma < 0.65$.

$$W_0 = S_{LQ}^{-1} \cdot I$$
$$W_1 = I$$
$$W_2 = \frac{1000s + 1000}{s + 1000}$$

We walk through the same design procedure as before including the updated high frequency rolloff filter and obtain a new controller.

4.3.4 Uncertainty Model H_∞ Minimized Controller

Another control model worht considering is that of the H_∞ norm-minimized design for the derived uncertainty description framed through an LFT. From before, we obtain an uncertainty description and for Q based on the modal, input, and output components of the individual transfer functions with uncertainty introduced per equation 3.18. We formulate an H_∞ minimization LMI problem and optimize over γ. The controller is developed with high frequency rolloff as well of the form $F = \frac{180}{s+180}$ with a cutoff frequency of $180 rad/s$.

4.4 Controllers Compared to Derived Uncertainty Structures

When we calculate robust stability and robust performance margins with respect to two separate uncertainty structures, we impose certain criterion for evaluation. In the case of the first test, we consider a plant with multiplicative uncertainty amounting to 20%. We then calculate the robust stability margins for all closed loop control systems. Then, we also consider the previously derived uncertainty structure where the individual modes are assigned uncertainty and perform the same calculations. We note that the modal uncertainty structure will be harder to satisfy than the simple multiplicative uncertainty structure.

4.4.1 Robust Stability

For multiplicative robust uncertainty, we have a criterion we can check which will guarantee robust stability [13]. We define $\hat{W}_2 = 0.2$.

$$\left|\left|\frac{PK}{1+PK}\hat{W}_2\right|\right|_\infty < 1$$

For robust stability of our derived structure, we consider each plant transfer function $P \in \mathcal{P}$ and check the internal stability of each plant when connected to each controller in feedback by numerical iteration. We can check to what extent each controller provides internal stability for the uncertainty structure driving the set of plant transfer functions $\mathcal{P}$. That is, we will check what percentage of the modeled perturbation δ will destabilize a particular controller and quantify our robust stability margin in this way. The structure of the plant uncertainty does not exactly follow additive, multiplicative, or any other standard model, so obtaining a intuitive condition for stability is messy due to the way in which the δ perturbation enters the modal system.

$$\begin{aligned} M_{11} &= F(Q,K) \\ \mu_\delta(M_{11}) &= \frac{1}{\inf_{\delta\in\Delta} ||\delta||_\infty \quad for\, which \quad det(I - M_{11}(s)\delta) = 0} \\ \delta_{min} &= \frac{1}{\mu_\delta(M_{11}(j\omega))} \forall\omega \end{aligned}$$

Using the above formulation for the structured singular value, it becomes possible to formulate an LMI problem to determine the minimum δ value. This can be done numerically as well, especially with a single parameter that affects the overall structure of this system's plant.

The multiplicative uncertainty structure with 20% uncertainty is a benchmark which many of the control designs are able to achieve, however the modal natural frequency derived uncertainty structure proves tougher to satisfy. We hope that the expected margins from the modal uncertainty structure correlates with experimentally derived performance. Note that the H_∞ minimized Q controller performs notably worse than nearly all other controllers with the exception of the 2 mode LQG controller without high frequency rolloff. This is an important result, because it highlights the numerical difficulty in posing an H_∞ LMI formulation as the order of the system increases and more modal disturbances need to be minimized. This is especially true when the controller now has to account for a considerable dynamic range of uncertainty.

4.4.2 Robust Performance

For testing performance robustness on our multiplicative uncertainty model, there is a convenient criterion by which robust performance may be guaranteed [13]. In this case, we define $\hat{W}_1 = \frac{1}{\sup_\omega ||\mathcal{P}||_\infty}$. We are most interested in finding stable, robust controllers which are able to provide some level of modal attenuation across all tested frequency range and uncertainty conditions, so we are evaluating performance based on the worst case condition of our uncertain plant structure.

$$\left|\left|\left|\frac{1}{1+PK}\hat{W}_1\right| + \left|\frac{PK}{1+PK}\hat{W}_2\right|\right|\right|_\infty < 1$$

To test robust performance for our derived modal uncertainty structure, we use the supremum of the H_∞ norm over all the uncertainty range and frequency. Thus our criterion is directly comparing closed loop performance to open loop performance.

$$\sup_\omega \left|\left|\frac{\mathcal{P}}{1+\mathcal{P}K}\right|\right|_\infty < \sup_\omega ||\mathcal{P}||_\infty$$

The main reason behind this criterion is that the intention of these controller designs is to provide added modal damping in a robust manner over all the uncertainty. So, if we can guarantee that the closed loop system is no worse and only better over the entire frequency range and the entire uncertainty range, then we have achieved our goal. Note that in order to test this performance robustness on the modal uncertainty structure, a term was truncated to ensure the system is proper. The truncation involved eliminating the $2U_k\bar{\zeta}_k\bar{\omega}_k s$ term from the $\tilde{d}_k$ term as its propagation leads to improper transfer functions formed in the $Q_{21}^{i,j,k}$ terms.

4.4.3 Predicted Margins

What we find from the performance robustness tests are that the control designs cannot keep the maximum closed loop singular value below that of the maximum open loop singular value. In this regard, we have not been able to successfully develop a robust controller guaranteed to provide added damping over all the uncertainty in the system. What we can evaluate however is how well each controller performs relative to these indicators. In other words, we should expect the LQG controller to not provide robustness at all (the system is considered unstable with simply the full plant model

Table 4.1: Robust Stability and Robust Performance Comparisons for Controller Designs.

Controller	Reduced Model 20% Mult Unc		Full Unc Model	
	Rob Stab	Rob Perf	Rob Stab	Rob Perf
LQG	102%	60.8%	0%	0%
LQGF	648%	591%	68.8%	14.6%
Mix Sens	609%	594%	100%	41.6%
LQG Full	1000%	964%	89.1%	20.7%
LQGF Full	1080%	967%	112%	19.5%
Inv Sens	279%	226%	102%	73.5%
Q min H_∞	0	0	1.65%	0.919%

in closed loop). We should expect the LQG controller with high frequency rolloff to perform better in terms of robustness and the mixed sensitivity design better still. When looking at the 4 mode controllers, we should expect the LQG with rolloff to do the best in terms of stability, however interestingly enough the inverted sensitivity controller appears to indicate a much better robust performance margin than the rest even if it fails to ensure complete robust performance. The numerical results have been tabulated in table 4.1. These margins represent the percentage of a unit of δ uncertainty allowed into the system before either robust criterion fails.

In conclusion, we expect the controllers with high frequency rolloff to be much more robust than those without it. We also expect the mixed sensitivity design to perform with slightly better robustness than the LQGF design for the 2 mode controllers. However, we do not expect the inverted sensitivity design to perform with better robustness than the LQGF design for the 4 mode controllers. We do not expect the direct H_∞ minimized controller to perform particularly well at all, as it provides much lower margins than most of the other designs.

Chapter 5

Results

After performing all experiments, a certain trend may be observed with the first bending mode controllers. This trend may be extended to higher order systems, but there are complications which arise with the implementation of such a controller.

5.1 First Bending Mode Experimental Results

The series of first bending mode controllers, described in the experimental setup and testing chapter, yield results which support the notion that the more robust designs will perform better at higher system variance from the modeled nominal condition.

All the experimental testing data has been processed with a low pass filter using a moving average smoothing. This process helps to create a more continuous distribution in frequency content that is less noisy from each bin to bin.

From figure 5.1, the frequency responses of each closed loop system and the open loop system are plotted across all configurations within the frequency range of all modeled system modes. This yields a graphical interpretation of how each controller does relative to the open loop of the plant. It also shows how much variance exists at certain frequencies based on the uncertainty for all of the closed loop systems. The gain of the system's frequency response is also represented in terms of displacement per figure A.32.

The weighted H_∞ norms of the closed loop systems were determined with filter weighting to isolate certain frequency ranges. The resulting H_∞ norms are tabulated for each testing method.

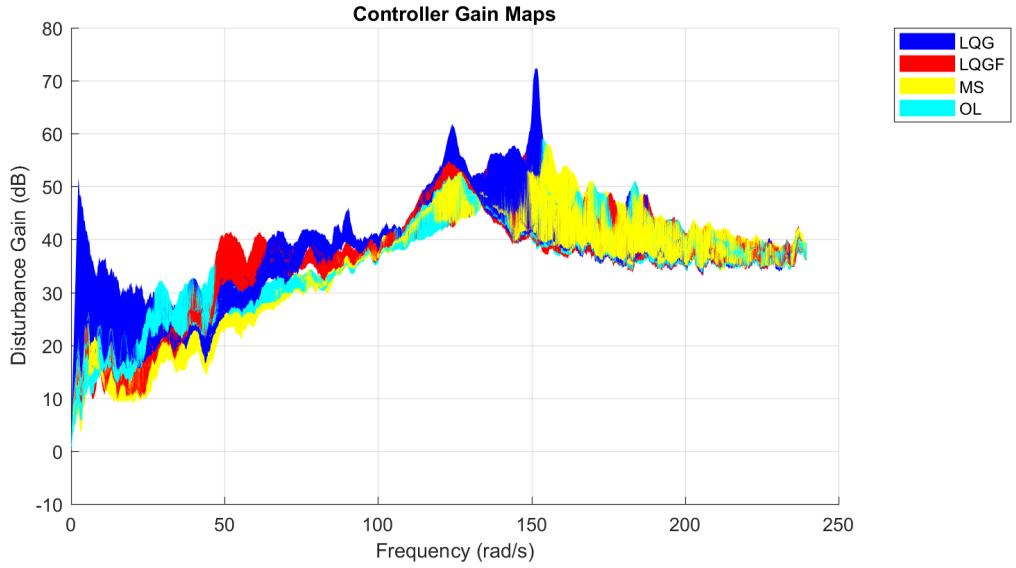

Figure 5.1: Ranges of Frequency Responses for LQG, LQG with HF Rolloff, and Mixed Sensitivity Closed Loop Systems as well as Open Loop System.

Referencing figure 5.2, this figure was developed by calculating the maximum and the minimum values of each frequency response for each open loop and closed loop system then plotting the percent gain increase or decrease over the open loop value each closed loop system achieved. This can be seen as a measure of relative improvement or degradation of attenuating disturbance input gain. Note that these plots are not in units of dB themselves, because a relative calculation was made between the closed loop frequency response and the open loop frequency response.

Note that each controller also behaves worse in the lower frequencies which roughly correspond to the rigid body modes, especially the LQG controller. This could be a sign that the washout filter did not perform as expected in the closed loop experimental system, because part of its primary function was to ensure the controllers are not sensitive to the lower frequency disturbances.

Tables 5.1, B.8, and B.7 show that the three controllers each perform noticeably worse as the added mass to the wings decreases, which is contrary to the initial hypothesis. In fact, this is the opposite trend, and that is due to the significant difference between the natural frequency produced by the finite element study and that derived from system identification testing. The experimental frequencies would place the maximum loaded condition as closest to the nominal frequency of the model. Therefore, while this trend is the opposite of the desired result, it still confirms that closed

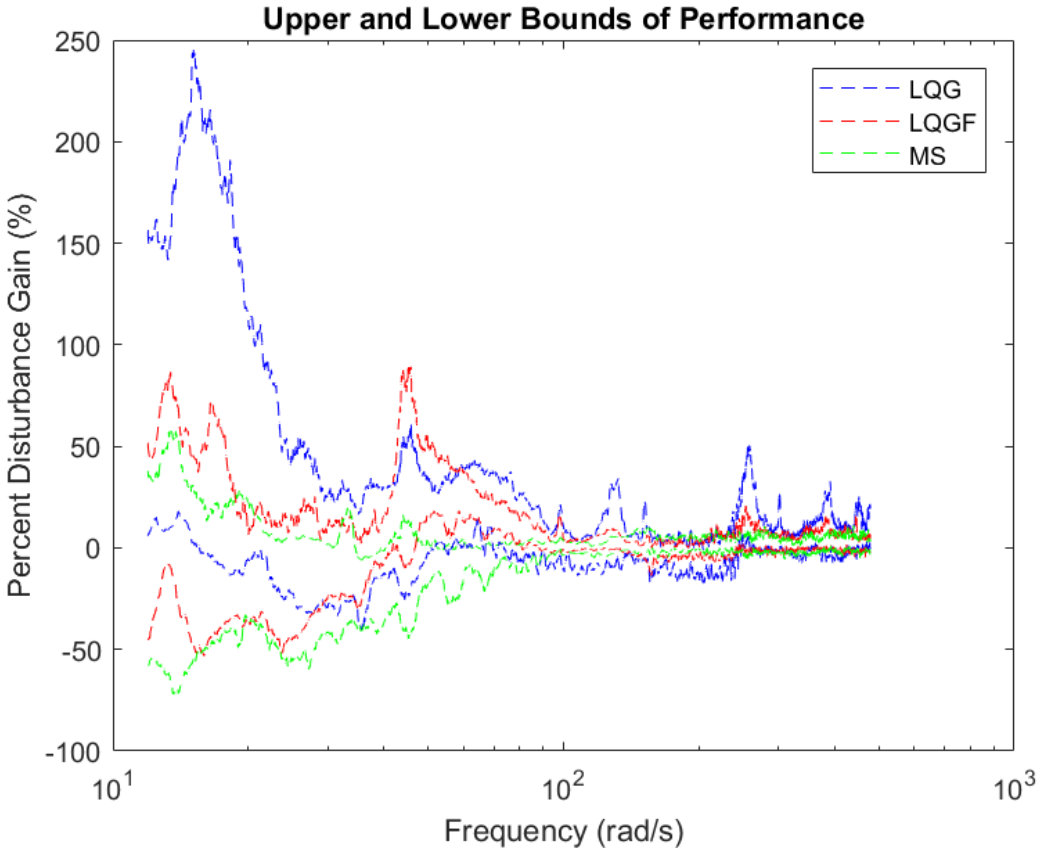

Figure 5.2: Change in Disturbance Gain with Respect to Open Loop System (% change in dB).

loop system performance will generally degrade with increasing system uncertainty.We should therefore expect the higher weighted conditions to produce better performance than that of the lower weighted conditions, meaning the "nominal" mass loading of no wieght added represents the extreme condition relative to the expected frequencies of the model.

The tables show that the controllers perform the best in the frequency region which contains the modeled natural frequency values of the first two modes. This is an expected outcome. Another trend is the degradation of performance in closed loop as the system's natural frequencies deviate more from the modeled values. We note that the LQG controller and the LQG controller with high frequency rolloff display a trend that would suggest shifting the resonant peak rather than cancelling it.

Unfortunately, the controllers did not do well in the higher weighted frequency

Table 5.1: Frequency Weighted H_∞ Norms (dB) for Two Mode Controller Designs (White Noise Results)

	2-6Hz				2-16Hz				2-35Hz			
CFG	OL	LQG	LQGF	MS	OL	LQG	LQGF	MS	OL	LQG	LQGF	MS
0	46.69	47.77	47.63	47.37	46.69	47.77	47.63	47.37	54.12	65.60	56.62	56.71
1	42.53	42.23	42.18	42.19	42.53	45.13	44.12	42.19	55.14	58.48	56.87	55.56
2	36.94	35.97	36.77	35.13	42.76	44.62	43.90	42.96	49.45	54.88	51.98	50.87
3	34.62	34.73	34.07	33.60	44.22	45.35	44.77	44.24	57.46	66.65	60.71	59.53
4	36.19	40.00	36.40	36.41	41.21	44.39	42.15	41.12	51.22	58.78	53.37	52.24
5	44.28	40.96	44.14	39.94	44.28	45.35	44.14	41.78	53.69	57.17	56.31	55.48
6	39.90	40.91	39.14	39.18	41.86	43.31	44.01	42.37	51.54	62.41	52.44	52.43

region and displayed poor attenuation of higher frequency disturbance even in configurations closer to the modeled freqeuncy. This does bring up an interesting contradiction to what our robust margins would have predicted. Of course, we modeled the system uncertainty to account for up to 20% variance in natural frequency values when the difference between the model and experimental frequency values themselves are already 35% or more in some cases. To this end, while the correlation between robust margin and experimental results does not line up perfectly, there are at least some trends in performance worth highlighting. The mixed sensitivity design was overall the most robust of these three with poor performance in the high range but not substantially worse than the other controllers. The LQGF certainly proved itsef more robust than the LQG controller, and the high frequency rolloff filter proves vital in desig for this structural control model study.

5.2 Other Controller Results

From the first bending mode experiments, it is clear that the closed loop system displays behavior and performance that is in line with expectations and theory surrounding stability robustness and model uncertainty. The challenge now of creating a robust and effective four mode controller will utilize all knowledge known of the system. Therefore, implementing knowledge from our system identification and other experimentation, an eight state, four mode LQG controller is derived which is weighted to balance a reasonable expectation of control input to modal disturbance rejection. This means saturating the controller only when the disturbance frequency reaches one of the two torsional mode values as well as contributing additional damping amounting to 0.13 or so total.

Table 5.2: Frequency Weighted H_∞ Norms (dB) for Four Mode Controller Designs (White Noise Results, Nominal Only)

	2-6Hz				2-16Hz				2-35Hz			
CFG	OL	LQG	LQGF	MS	OL	LQG	LQGF	MS	OL	LQG	LQGF	MS
0	46.69	47.05	47.05	48.05	46.69	47.05	47.05	48.05	54.12	54.43	55.32	52.92

The end results show that the standard LQG controller fares better than the one with the additional high frequency rolloff filter implemented. The LQG design also does better at attenuating low frequency rejection in comparison to the robust inverted sensitivity function design. However, the inverted sensitivity function design appears to fare better at overall maximal rejection, because it manages to attenuate the higher modes better which have considerably more impact on the system than the lower frequency modes. It is the only controller which managed better performance at the zero loading condition through the high frequency weighted H_∞ norm in table 5.2.

This result demonstrates the limitations of controller bandwidth allocation. The LQG design has a lower frequency focus which means the two low frequency modes are fairly well attenuated, but the higher two modes are not as well attenuated. The opposite is true with the inverted sensitivity design, because in that case, the controller is much more sensitive to the higher frequency modes. This comes at the cost of performance with the lower frequency modes. The symmetric and asymmetric sine burst results can be seen in tables B.9 and B.10.

Chapter 6

Conclusion

6.1 Summary

To summarize what was accomplished with this thesis project, we considered the structural test article called Iron Bird and performed structural analysis via FEA software in order to obtain an LTI state space model with which to conduct control design to attenuate system modes of the wings. In order to complete this model and to supplement the controller designs, the structural article itself was tested using system identification techniques to obtain experimental parameters involving the damping coefficients, noise covariance, and frequency values. With a derived model and experiemntal system, various control designs with differing levels of robustness were implemented and tested on the structural article with differing mass loadings on the wings which provided system uncertainty. The results were tabulated and analyzed for each control design tested.

Overall, a discrepancy between model and article prevent the results from correlating exactly to expected results which can be observed per figure 6.1 (also in figures A.29 and A.30). In the experimentally derived natural frequencies, values deviated from their modeled counterparts by up to 35% which is considerable in light of the structured uncertainty accounting for up to 20%. Despite the inconsistencies, there is still a trend of performance degradation and instability as the test article's natural frequency drifted further from the modeled nominal natural frequency value.

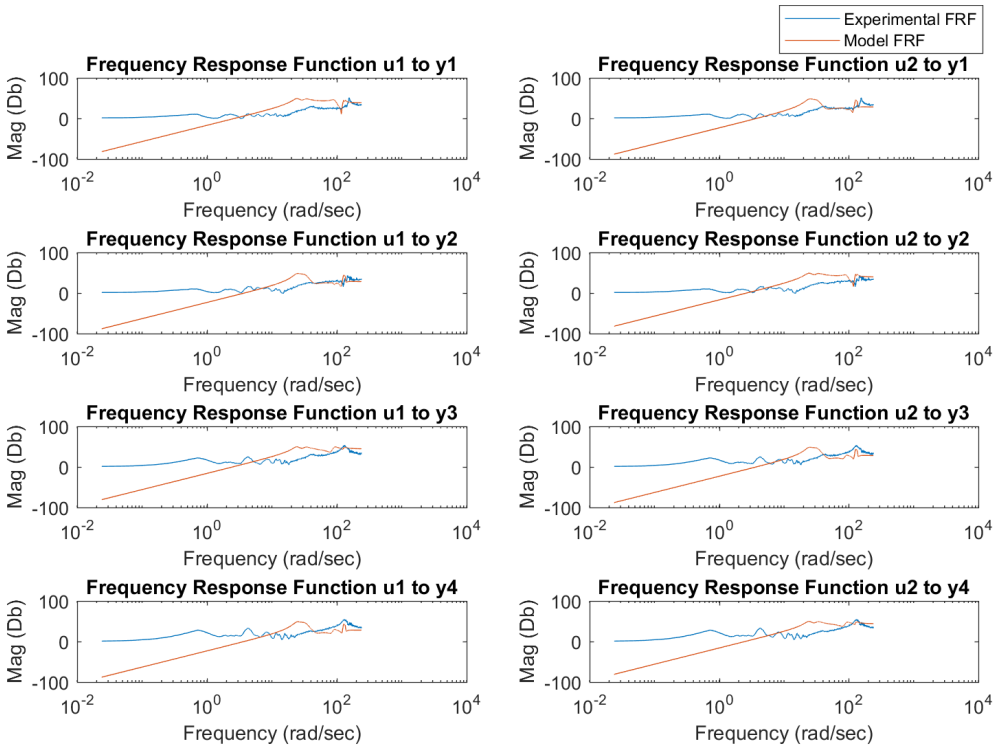

Figure 6.1: Frequency Response Functions of Experimental Data of Nominal System with Symmetric Sine Burst Input Compared to Model.

6.2 Future Work and Refinements

This study employed a simplistic FEA study methodology and does not incorporate any advanced methods of modal analysis. For future improvements, it would make sense to leverage the the full expertise of an industry leader in the field such as ATA Engineering for improving the upfront modeling of the system. One suggestion which discussed during analysis was the incorporation of superelements in the FEM. Further refinement in modeling technique would lead to a more accurate initial model which would hopefully correlate closer with the test article. Another consideration is modeling the change in dynamics when the test article is grounded by the connection of the linear actuators. This constrains free body motion and adds some degree of damping to the wing bending. Gaining a more accurate sense of this effect would lead to a better development of an upfront FEA.

The experimental data most notable shows the effects of the closed loop control with lower order control models. The higher order controllers received minimal ex-

perimental testing, so it remains uncertain exactly how well all of these higher order designs would perform under each uncertainty configuration.

While balanced truncation model order reduction methods were examined, there was minimal formal testing of the balanced truncation derived controllers. The truncation featured in this study amounted to truncation of the derived modes, rather than reducing higher modes to a lower order, and this was done in part to preserve the physical interpretation of each state without requiring a similarity transformation.

The subject of flutter was discussed in the first chapter, and this would be the primary subject of future study for this experimental based approach to "dry" wind tunnel testing. By refining the disturbance inputs to simulate the aeroelastic dynamics of negative damping, results from this experiment on uncertainty could better be applied to deriving control models for rejecting flutter. This would require a model of the aeroelastic conditions in which flutter occur which was studied previously [6]. Applying robust control formulations in the context of the flutter problem would lead to a new experimental methodology for flutter based control design. In the future, one would hope that future drone technology allows for lower costs to entry for aircraft design in a way that revolutionizes how active flutter suppression systems are developed. In this regard, the Iron Bird platform might serve as a model for carrying out lower cost simulated aeroelastic dynamic experiments on future designs.

Appendix A

Additional Figures

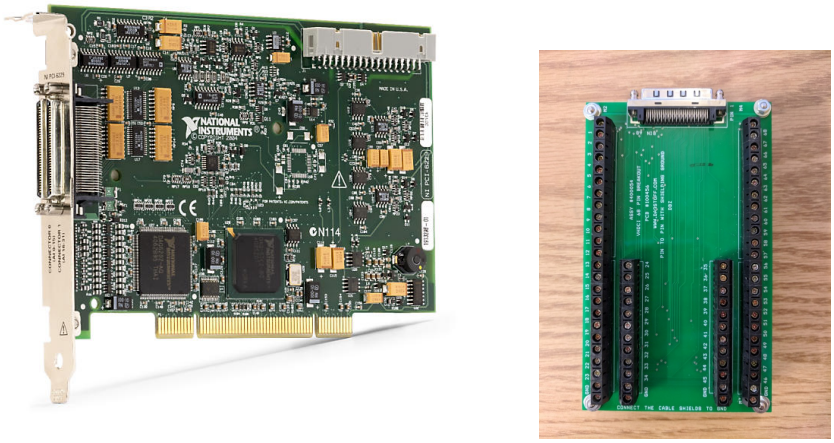

Figure A.1: Data Acquisition Card (Left) [37] [36] and Data Acquisition Card Breakout Board (Right).

Figure A.2: Linear Actuator [35].

Figure A.3: Motor Amplifier (Top Left) [9]. External Power Supply (Top Right) [3]. EMI Filter (Bottom) [44].

Figure A.4: Accelerometer with Evaluation Board [2] [1].

Figure A.5: Signal Conditioning Module (Top Left) [39]. Voltage Breakout Unit (Top Right) [22]. Force Gauge (Bottom) [40].

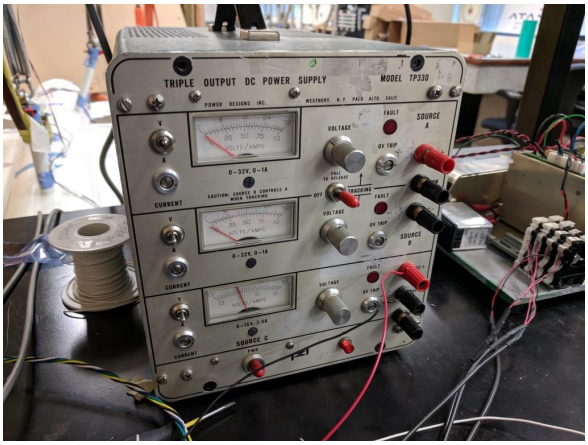

Figure A.6: Power Supply.

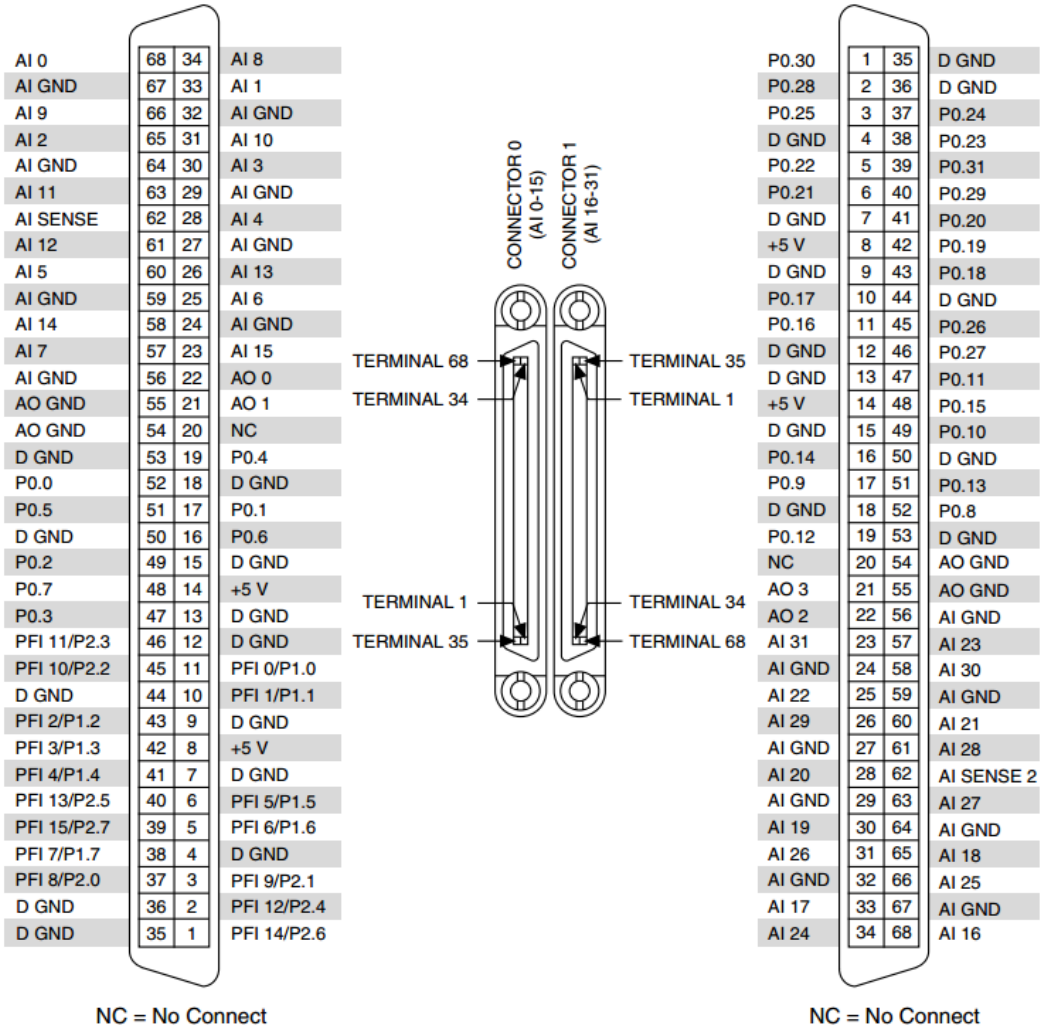

Figure A.7: PCI 6229 pinout from datasheet [37].

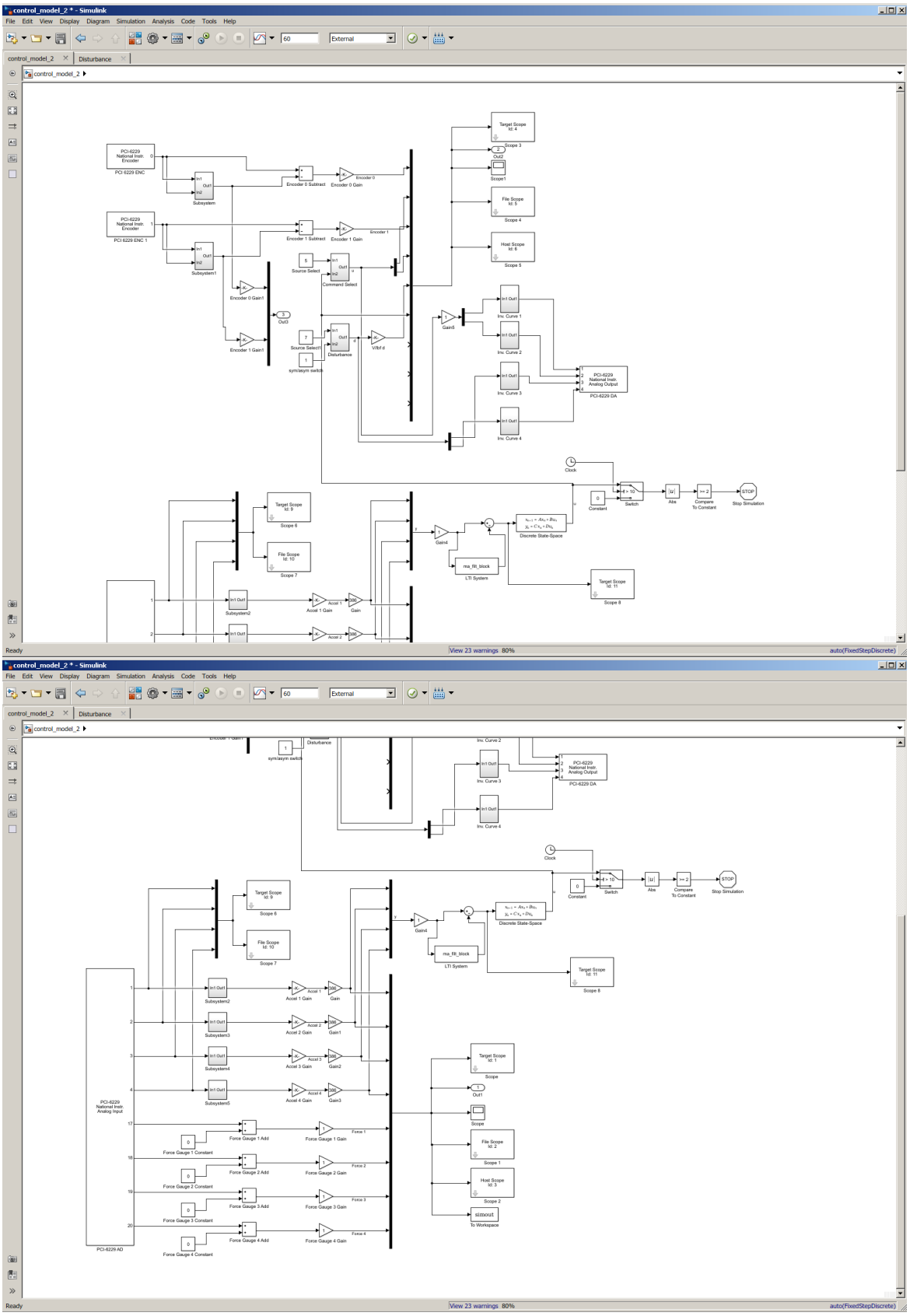

Figure A.8: Simulink Realtime Model.

Figure A.9: Simulink Realtime Target Computer Monitor.

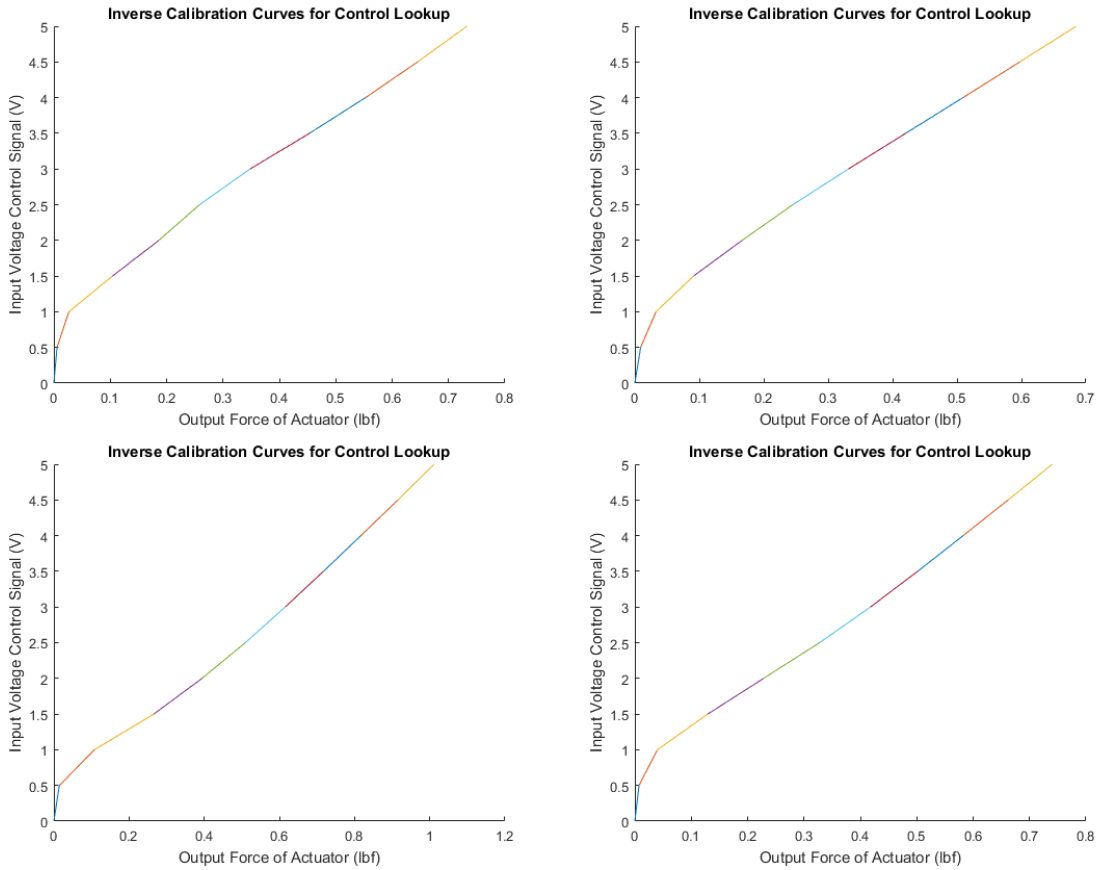

Figure A.10: Actuator 1 Inverse Calibration Curve (Top Left). Actuator 2 Inverse Calibration Curve (Top Right). Actuator 3 Inverse Calibration Curve (Bottom Left). Actuator 4 Inverse Calibration Curve (Bottom Right).

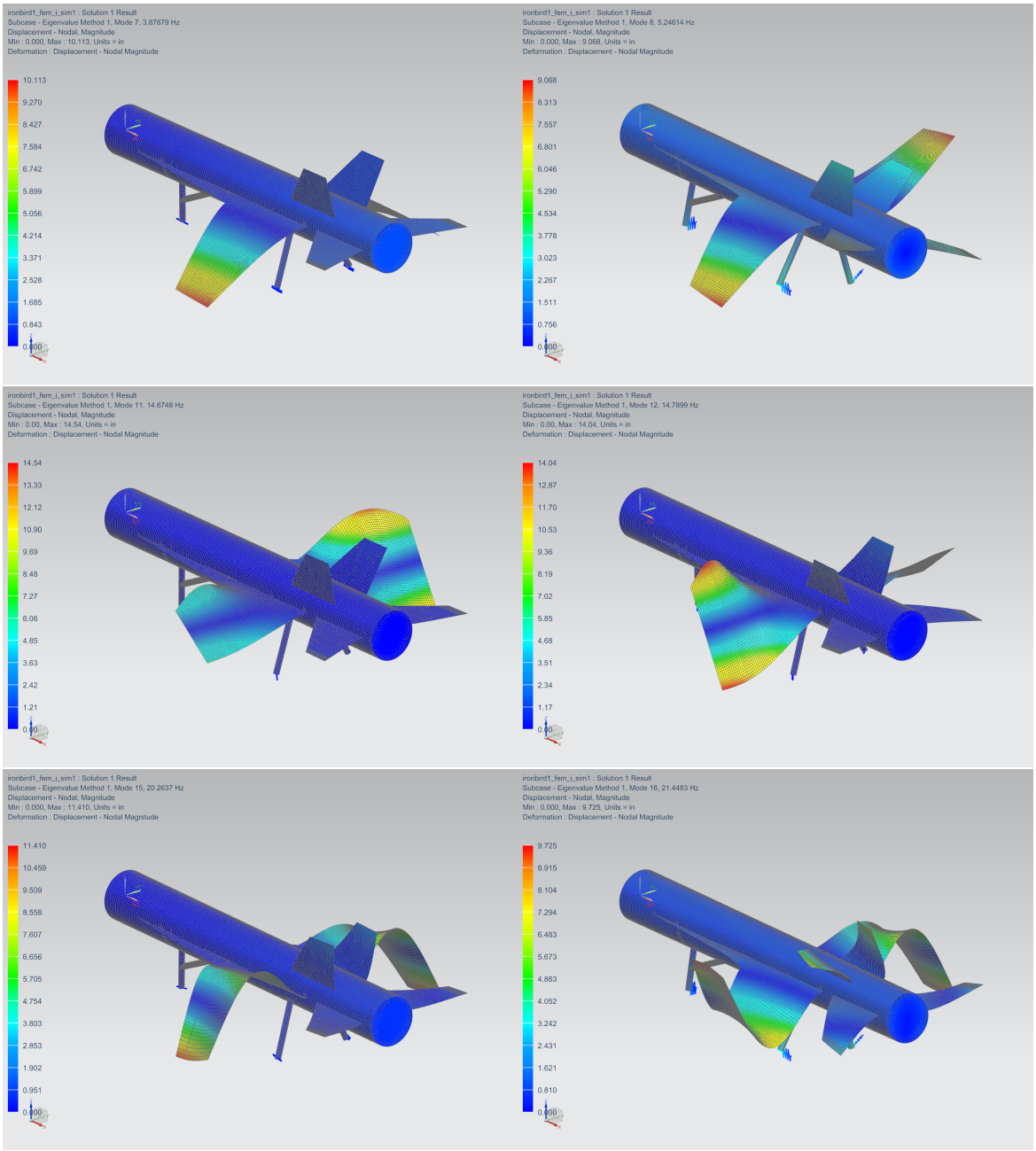

Figure A.11: NX Simulink Results for Nominal Configuration: (Left-to-Right, Up-to-Down) Modes 1, 2, 3, 4, 5, and 6.

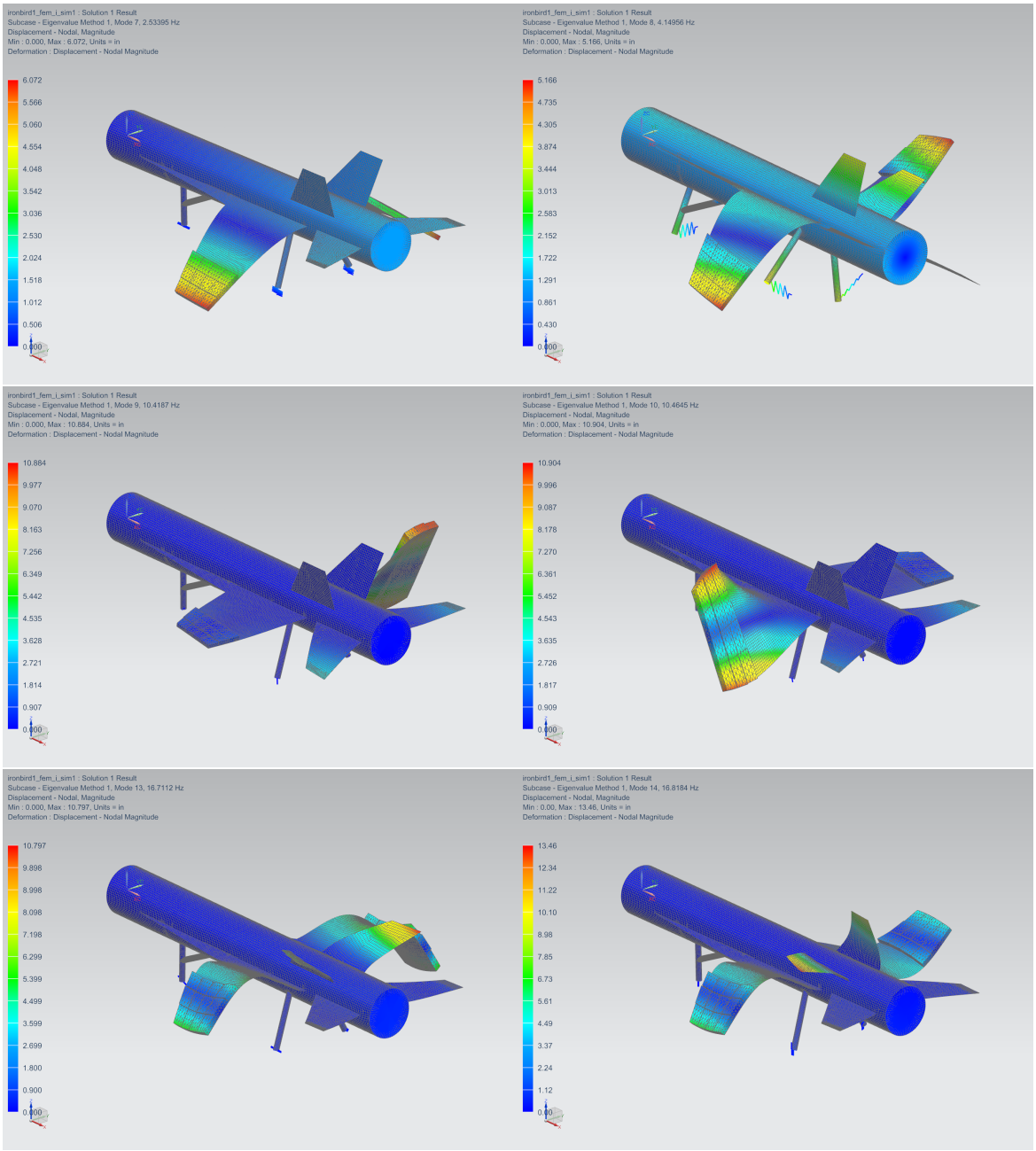

Figure A.12: NX Simulink Results for Configuration 1: (Left-to-Right, Up-to-Down) Modes 1, 2, 3, 4, 5, and 6.

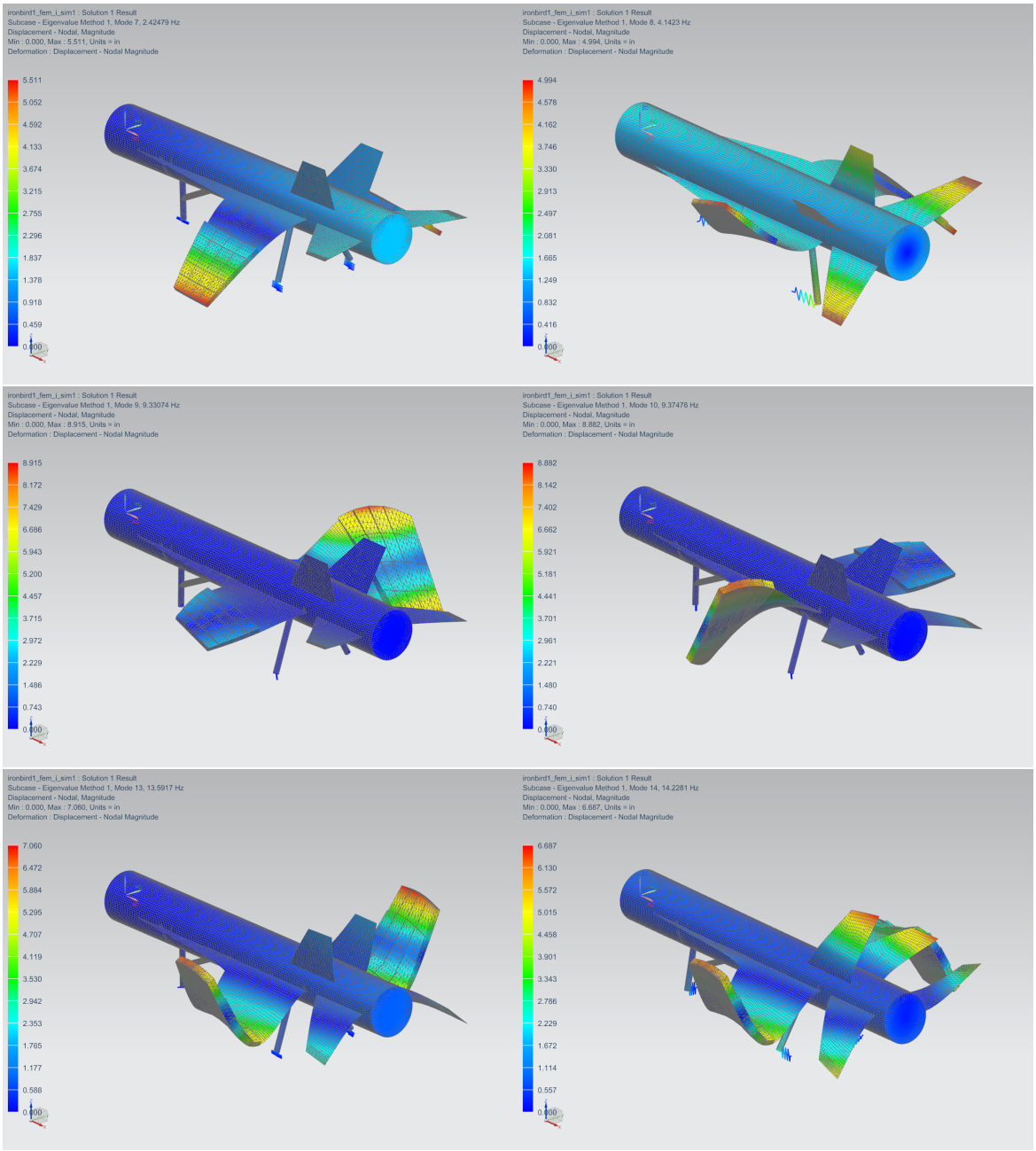

Figure A.13: NX Simulink Results for Configuration 2: (Left-to-Right, Up-to-Down) Modes 1, 2, 3, 4, 5, and 6.

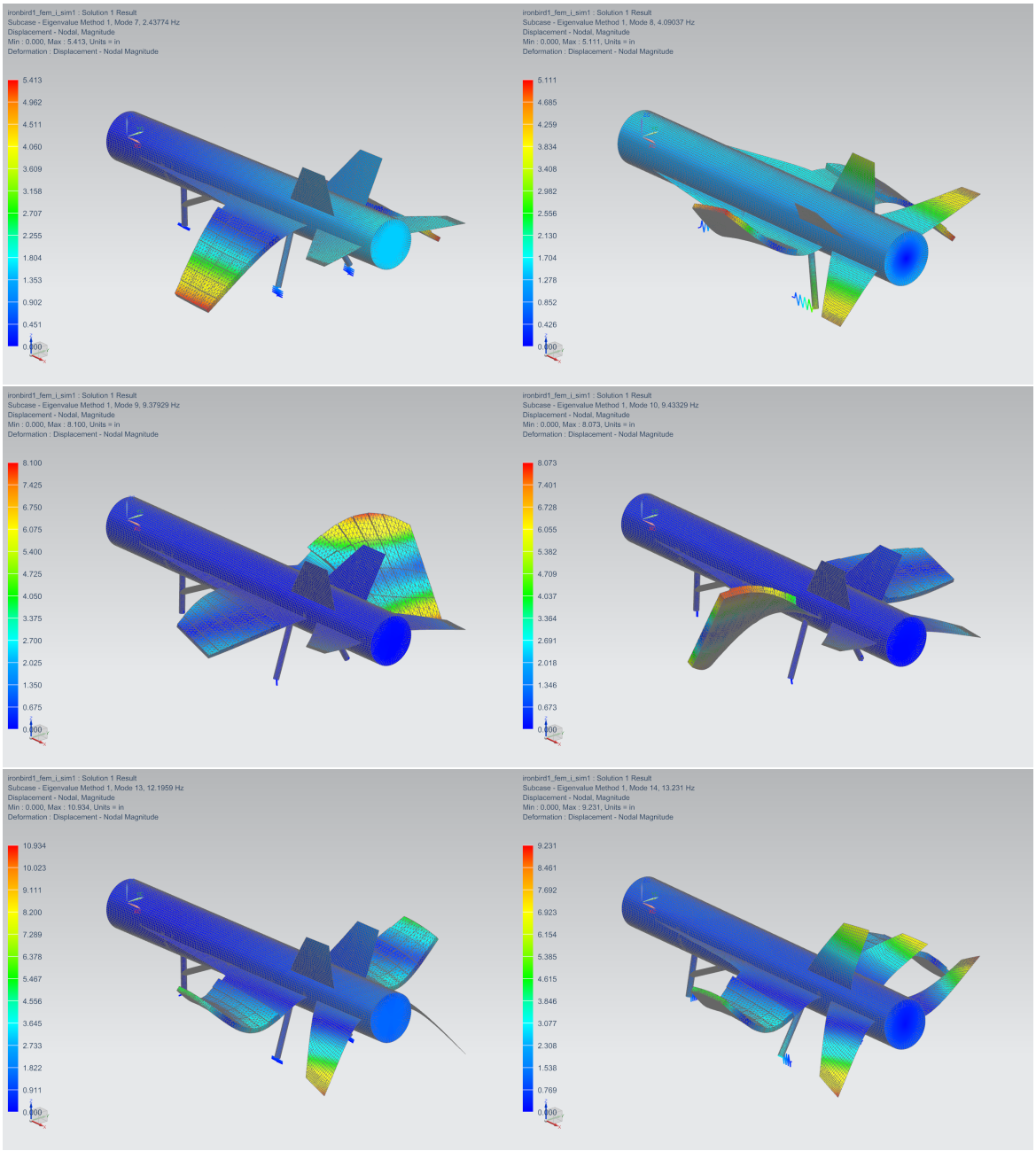

Figure A.14: NX Simulink Results for Configuration 3: (Left-to-Right, Up-to-Down) Modes 1, 2, 3, 4, 5, and 6.

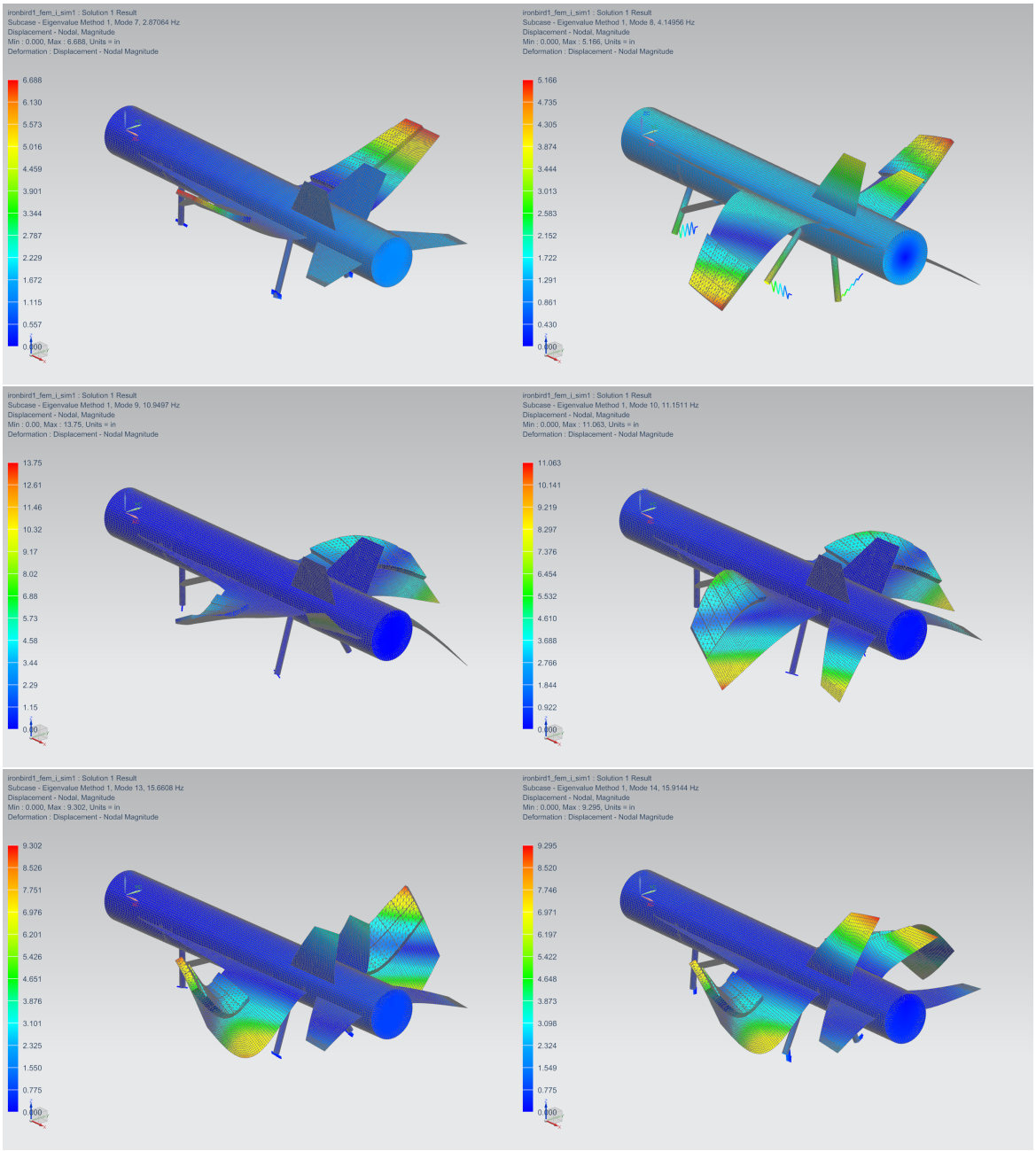

Figure A.15: NX Simulink Results for Configuration 4: (Left-to-Right, Up-to-Down) Modes 1, 2, 3, 4, 5, and 6.

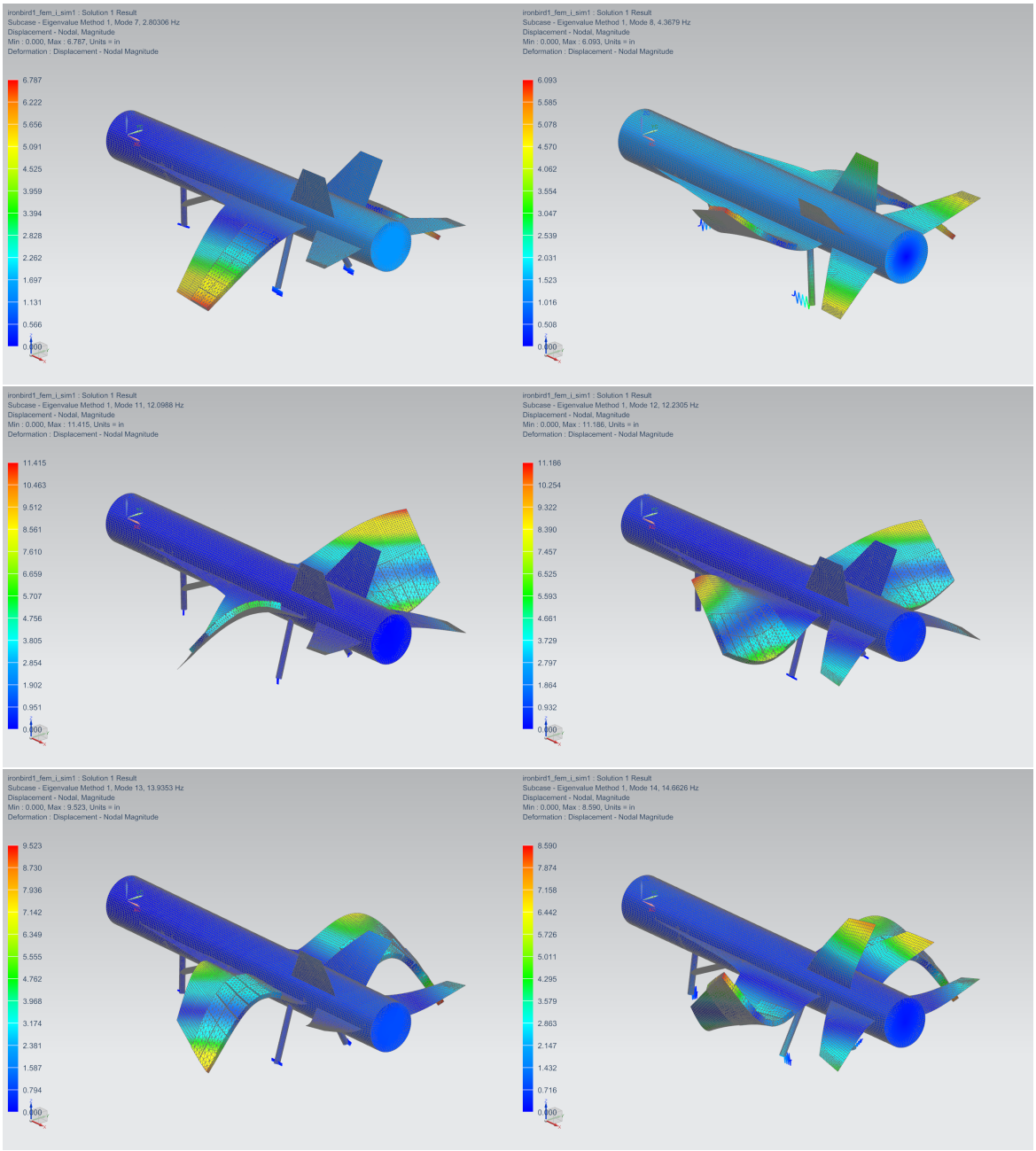

Figure A.16: NX Simulink Results for Configuration 5: (Left-to-Right, Up-to-Down) Modes 1, 2, 3, 4, 5, and 6.

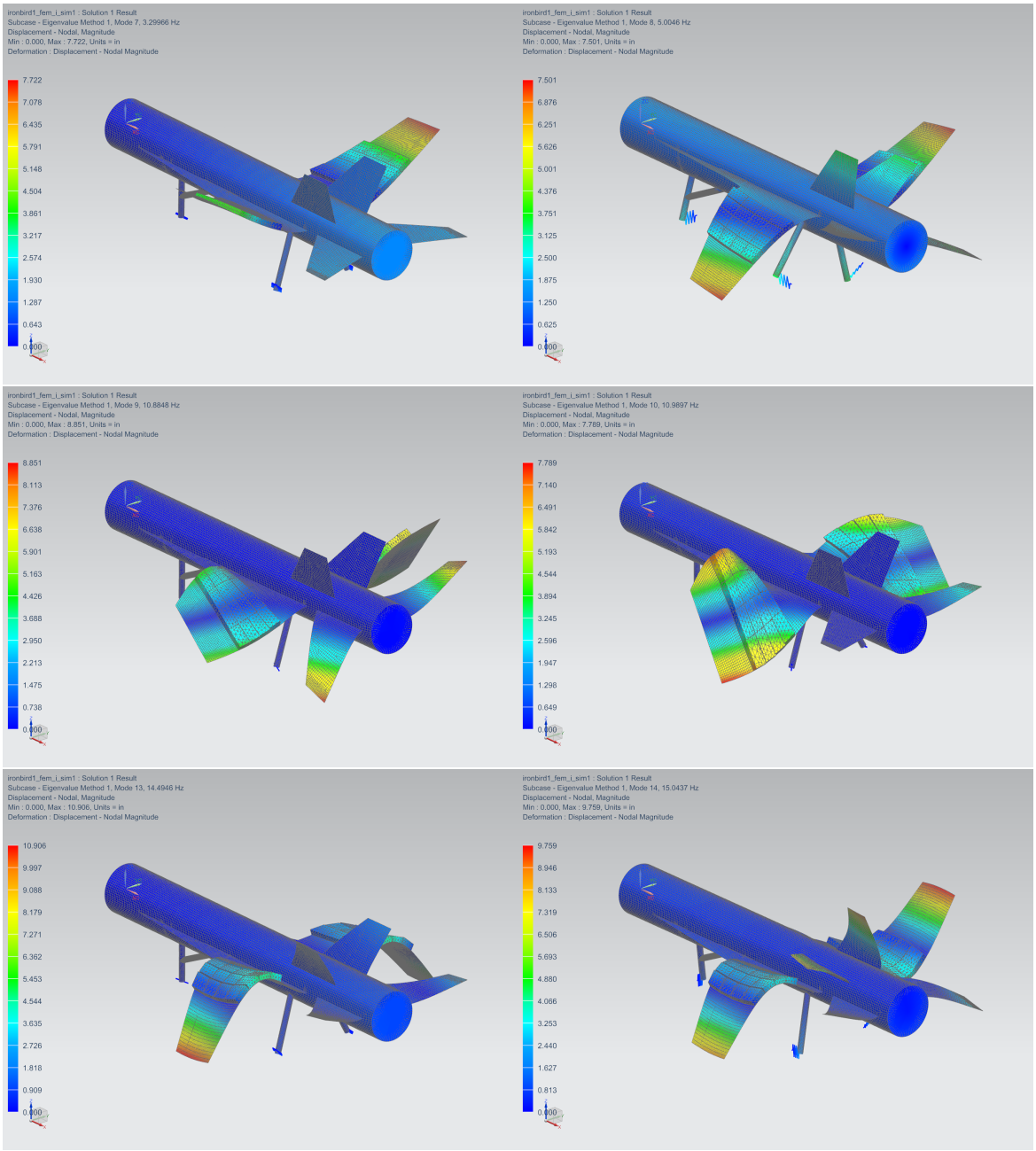

Figure A.17: NX Simulink Results for Configuration 6: (Left-to-Right, Up-to-Down) Modes 1, 2, 3, 4, 5, and 6.

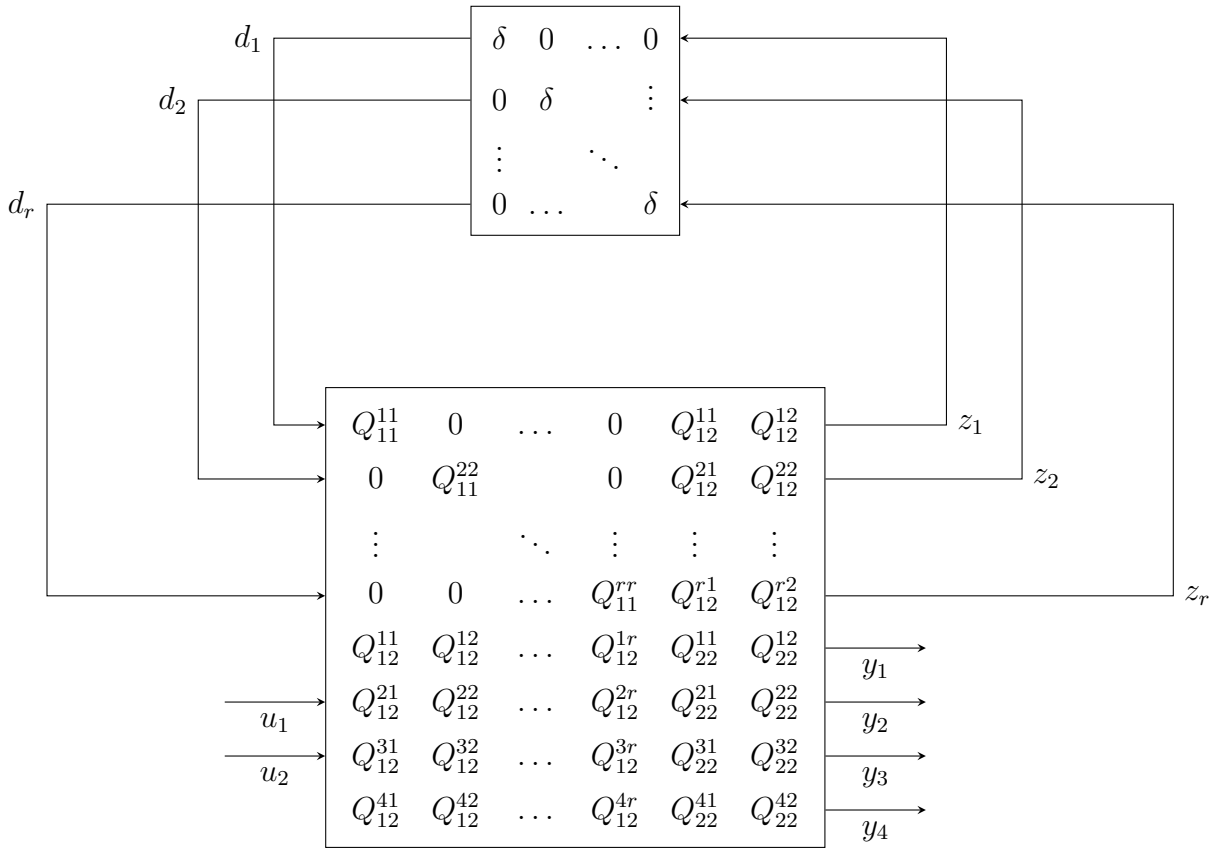

Figure A.18: LFT structure with r disturbances.

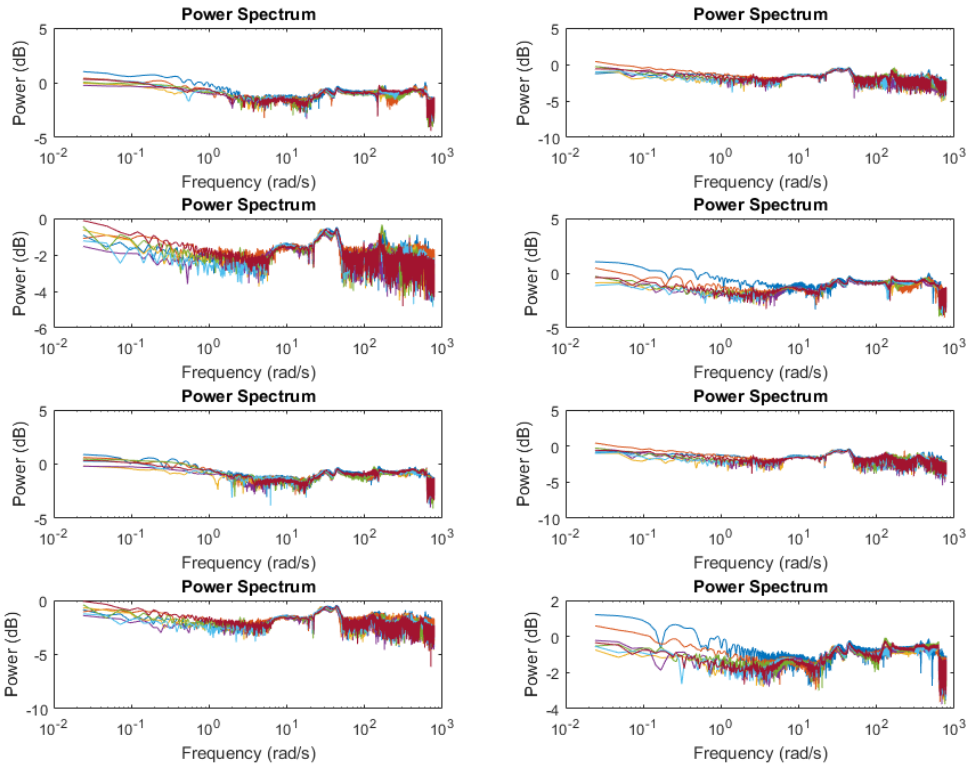

Figure A.19: Example of Experimentally Derived Power Spectra.

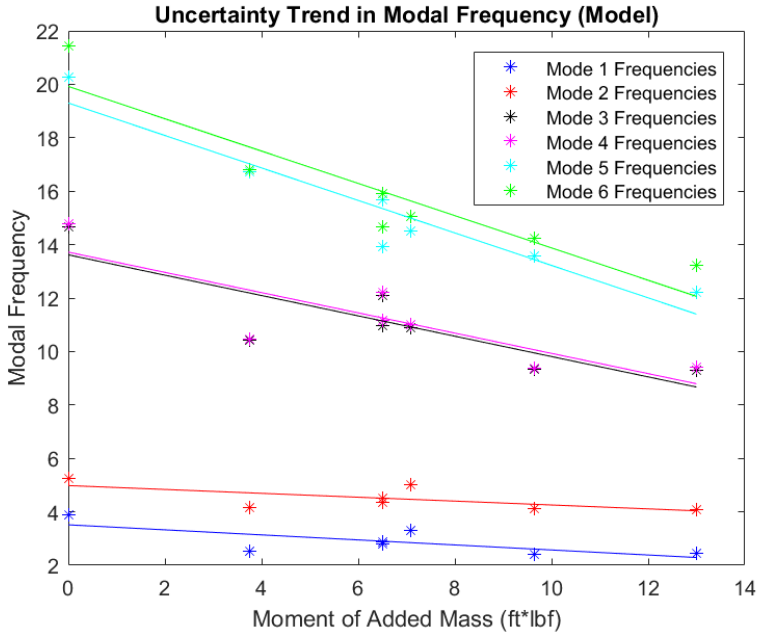

Figure A.20: Variance in Natural Frequency with Added Mass from FEA Model.

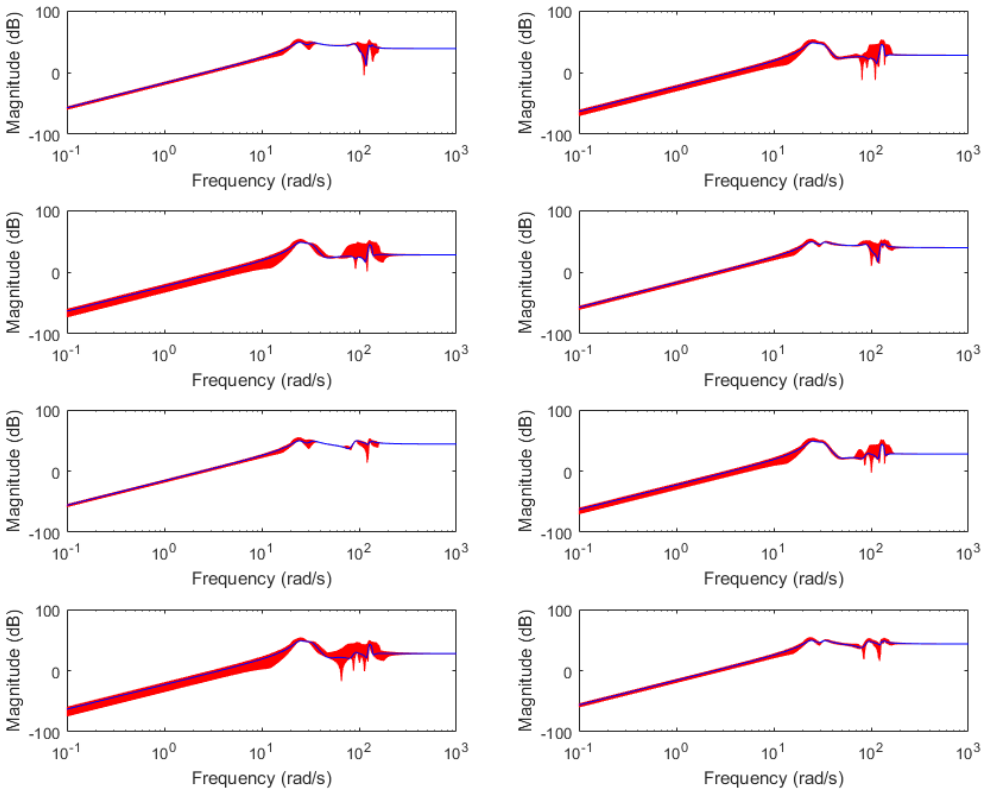

Figure A.21: Complete Modal Uncertainty Structure Bode Response.

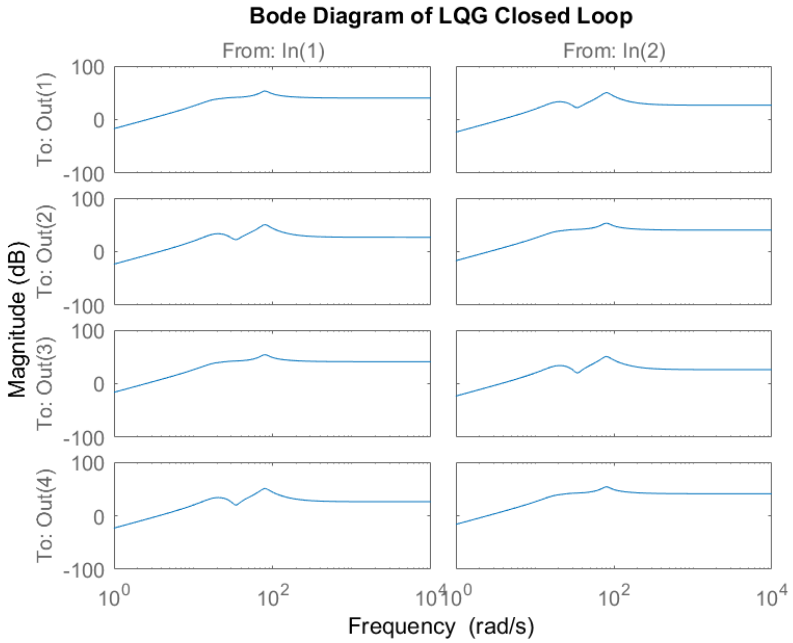

Figure A.22: Bode Response of Closed Loop LQG System.

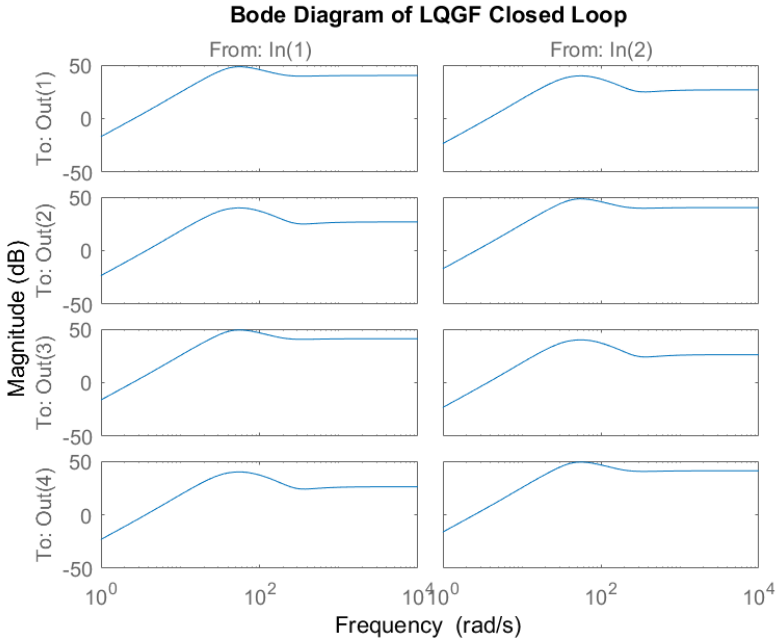

Figure A.23: Bode Response of Closed Loop LQG with High Frequency Rolloff System.

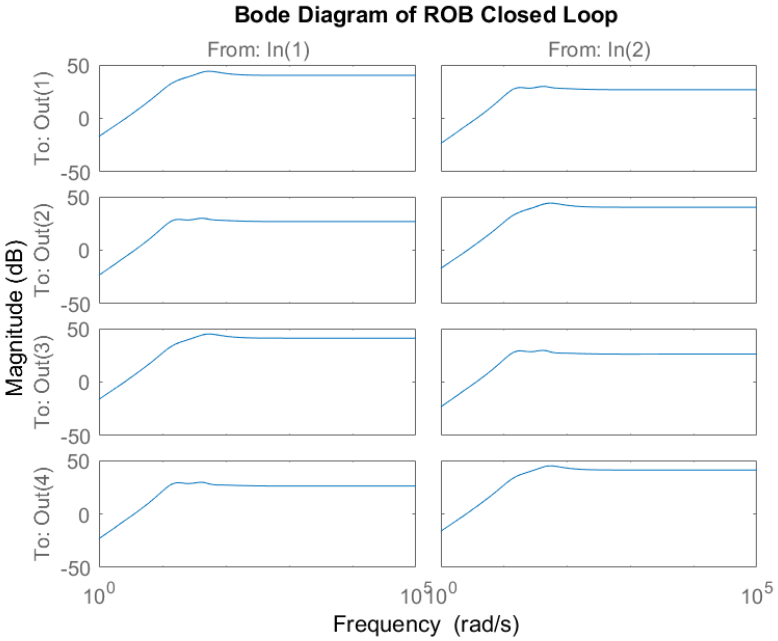

Figure A.24: Bode Response of Closed Loop Mixed Sensitivity System.

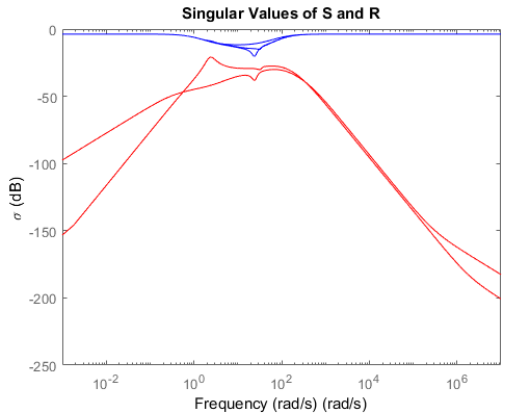

Figure A.25: Weighted Sensitivity and Control Sensitivity Functions in Mixed Sensitivity Design.

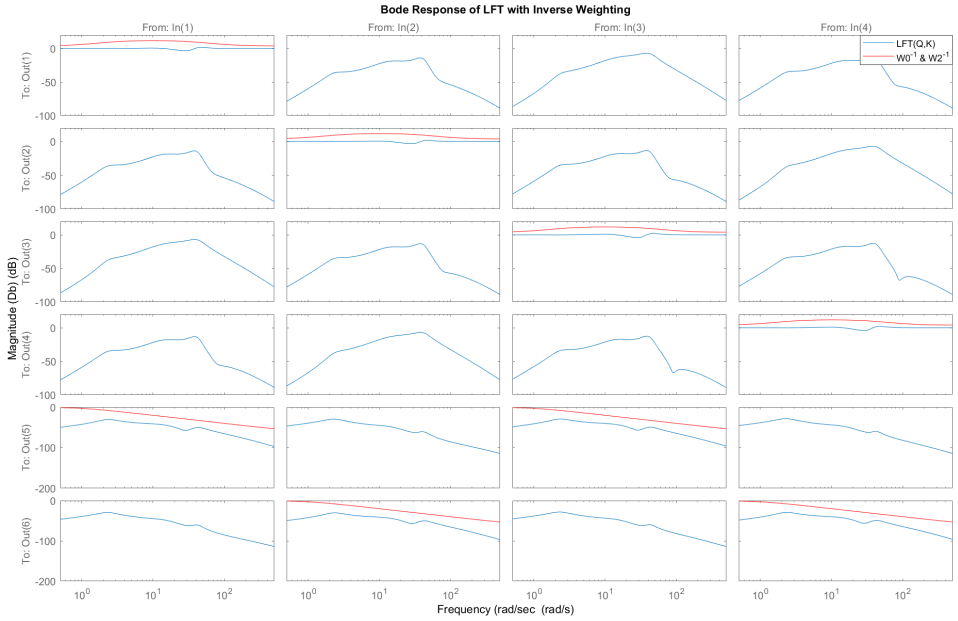

Figure A.26: Bode Response with Inverse Weighting Functions for Mixed Sensitivity Design.

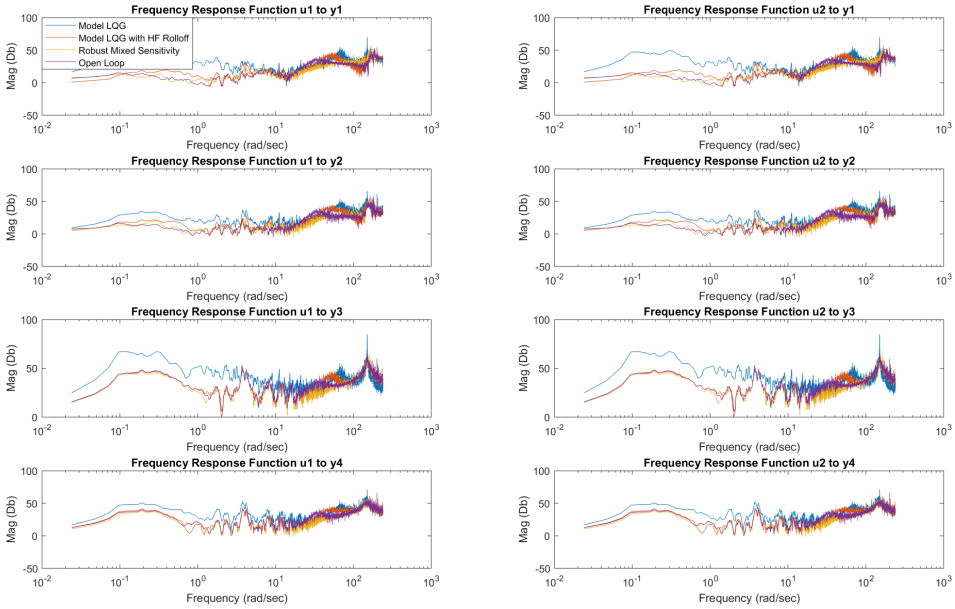

Figure A.27: Frequency Response Function from Experimental Data of Nominal System with Symmetric Sine Burst Input with Two Mode Controllers.

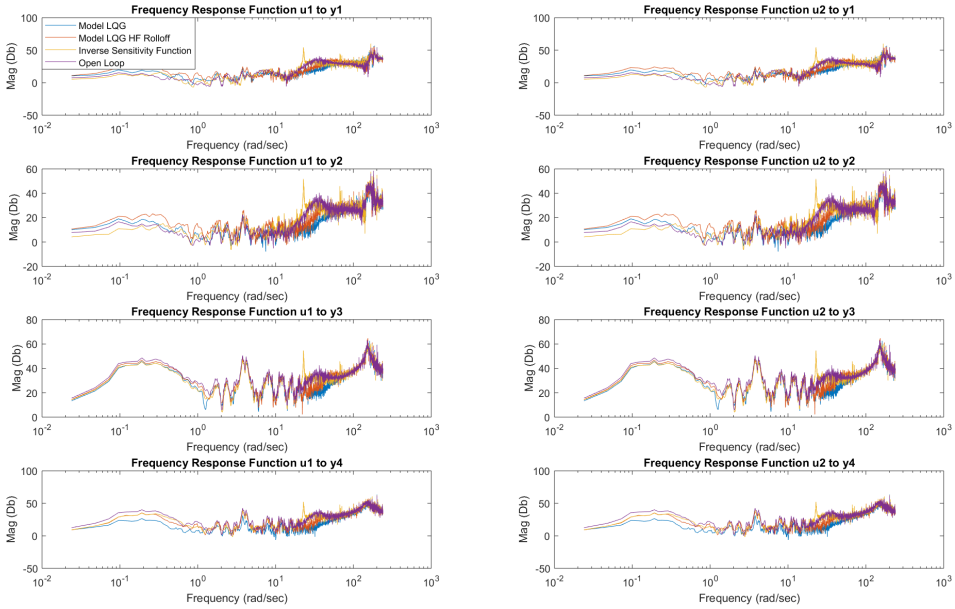

Figure A.28: Frequency Response Function from Experimental Data of Nominal System with Symmetric Sine Burst Input with Four Mode Controllers.

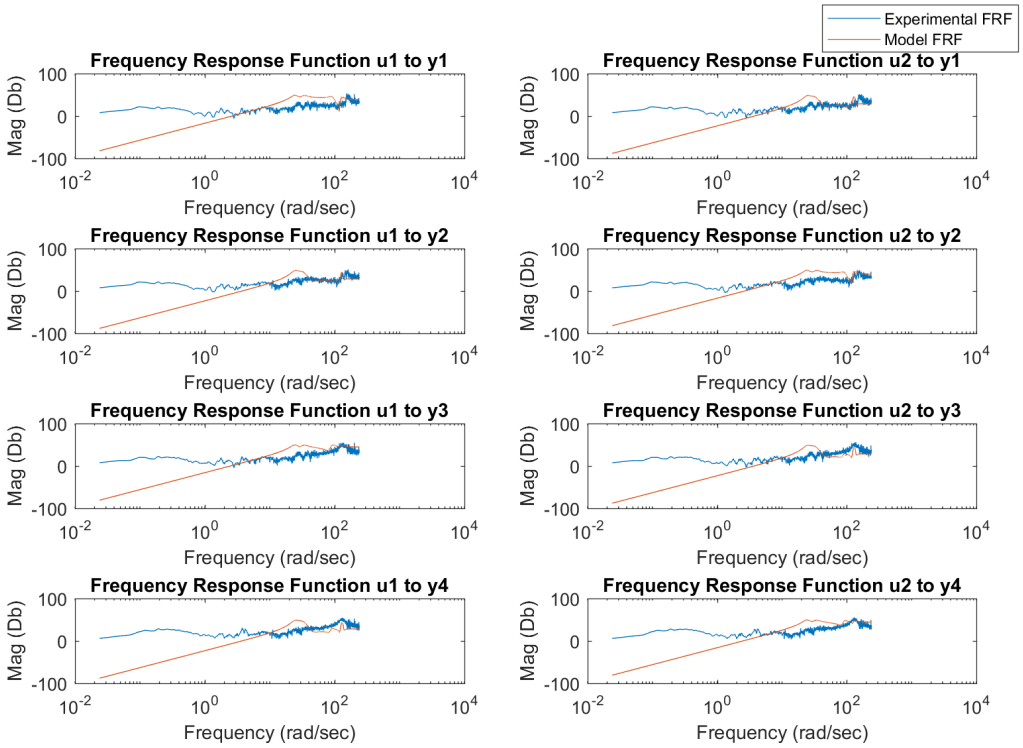

Figure A.29: Frequency Response Functions of Experimental Data of Nominal System with Asymmetric Sine Burst Input Compared to Model.

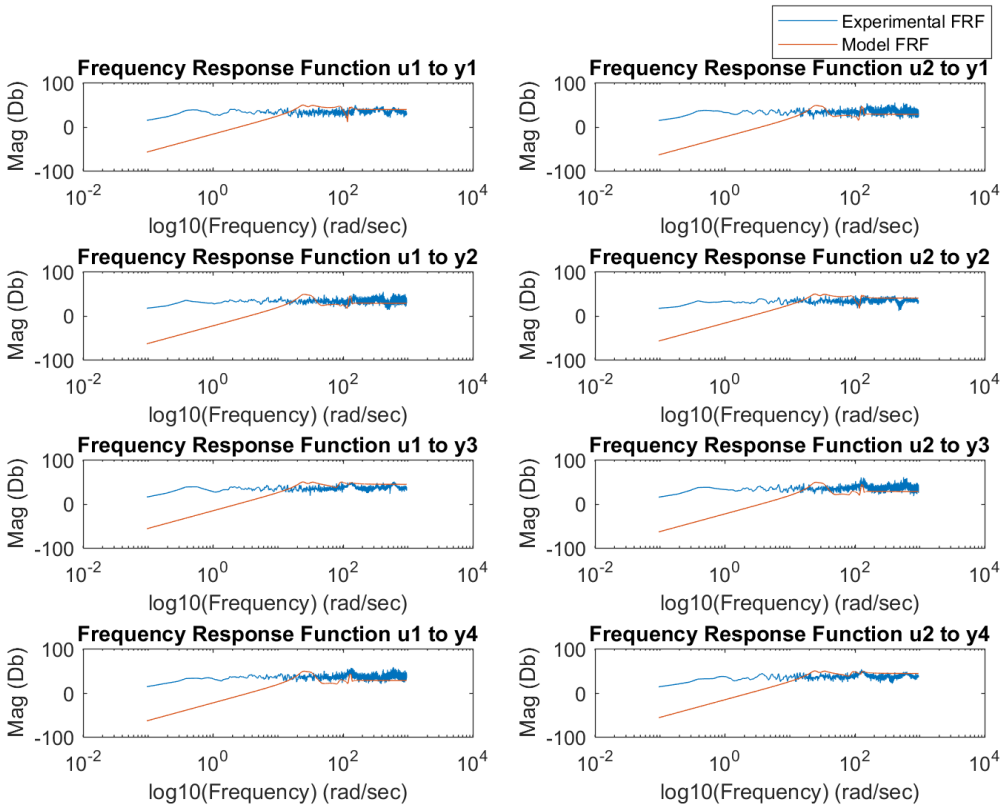

Figure A.30: Frequency Response Functions of Experimental Data of Nominal System with White Noise Input Compared to Model.

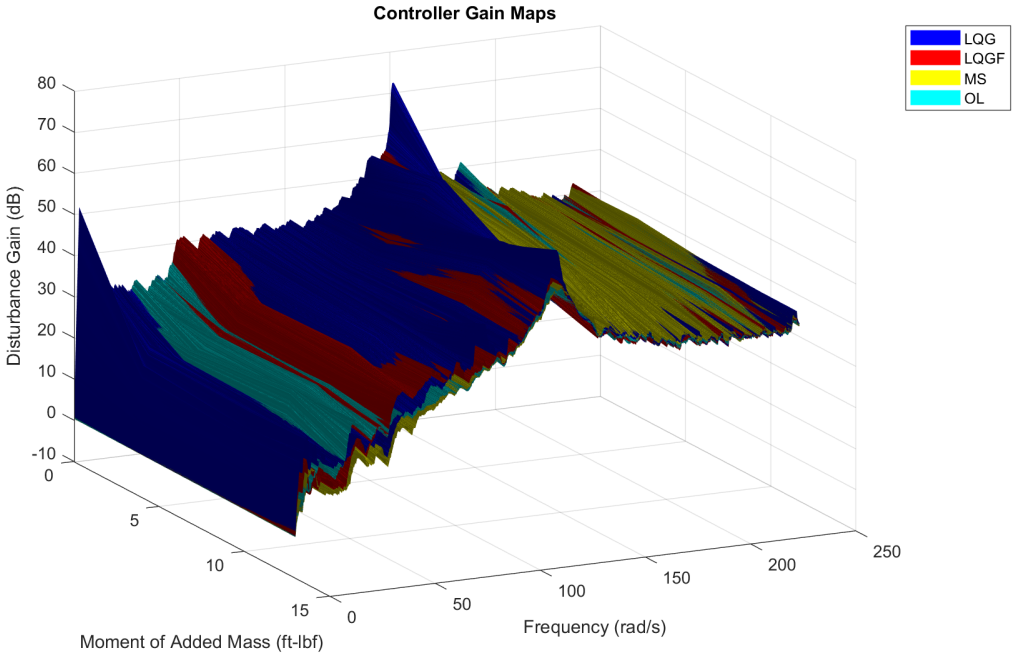

Figure A.31: Alternate Surface View of Disturbance Gain Maps for Each System.

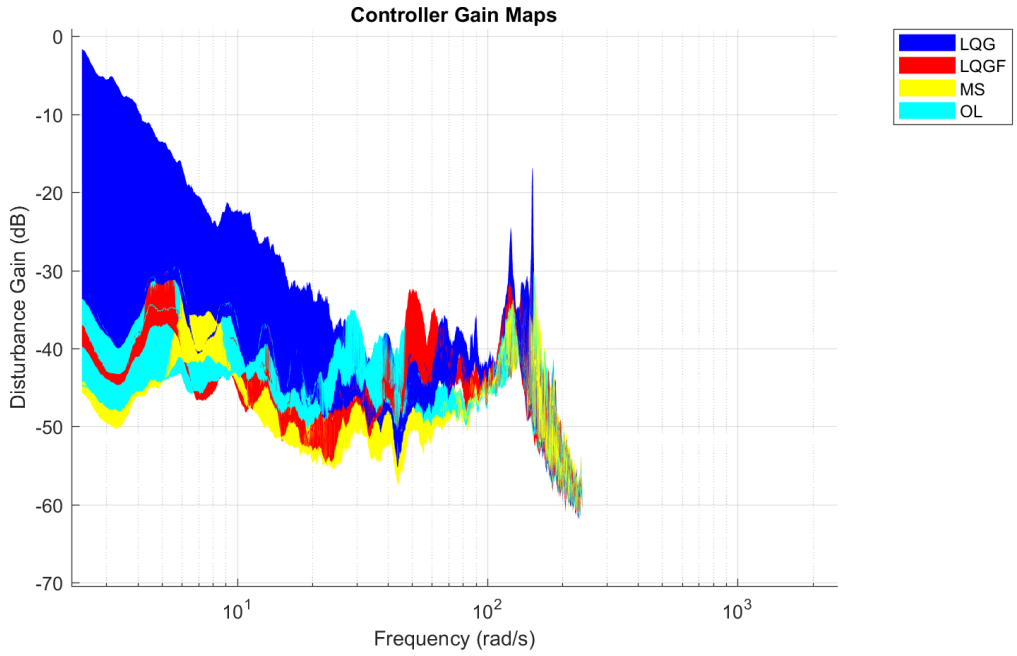

Figure A.32: Ranges of Frequency Responses for Closed Loop and Open Loop System (Gain of Displacement).

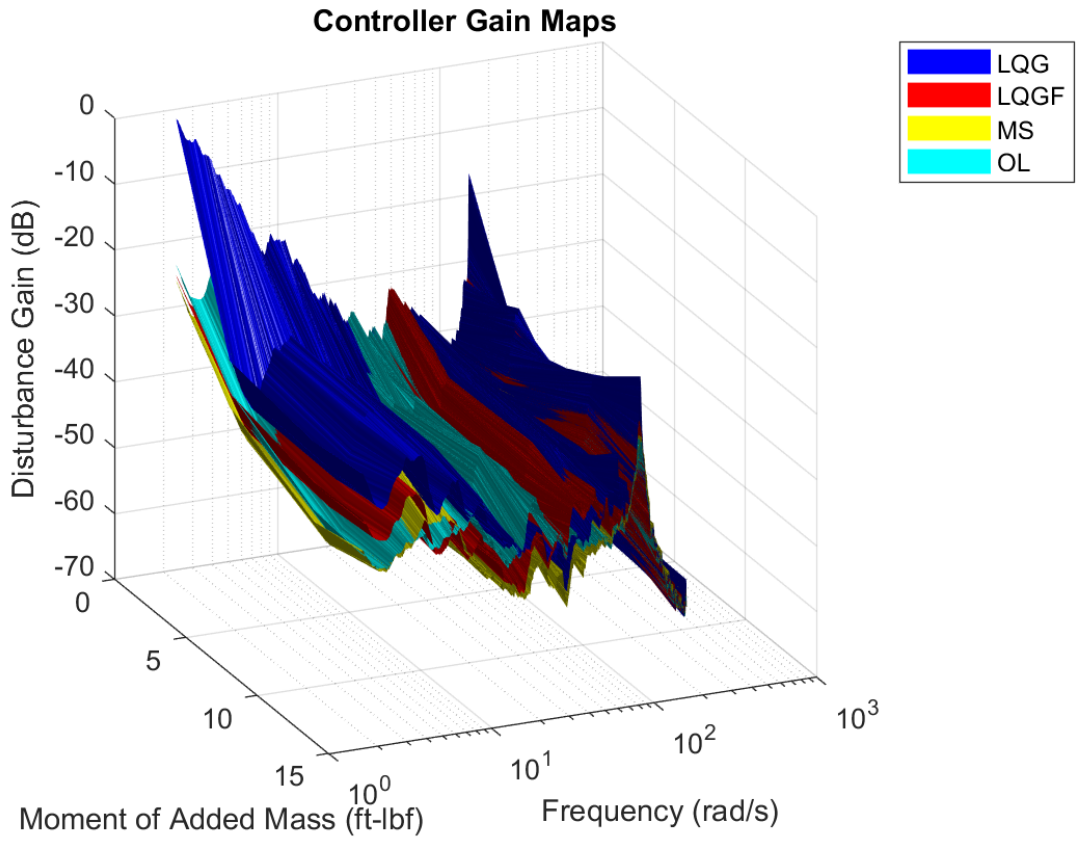

Figure A.33: Alternate Surface View of Disturbance Gain Maps for Each System (Gain of Displacement).

Appendix B

Additional Tables

Table B.1: List of hardware elements

Item	Manufacturer	Part Number	Quantity
Accelerometer	Analog Devices	ADXL203	4
Linear Direct Drive Motor With Encoder	Moticont	SDLM-025-095-01-05	4
Force Gauge	PCB	208A03	4
Actuator Calibration Force Gauge	Interface, Inc.	WMC-5	1
DC Power Supply	Power Designs, Inc.	TP330	1
DC Brush Motor Amplifier	Copley Controls Corp.	412CE	4
AC/DC EMI Filter	Schaffner	FN2070-12-06	1
External Power Supply	Artesyn Embedded Technologies	LCC600-48U-4P	1
Strain Gauge Conditioning Module	Vishay Precision Group	2120A	1
Signal Conditioner	PCB	442B119	1
Signal Channel Voltage Breakout Box	Agilent	US35375424 E1432-61600	1
Data Acquisition Card	National Instruments	PCI 6229	1
VHDCI 68 Pin Breakout Board	daqstuff.com	ASSY #400054 PCB #100456	2

Table B.2: DAQ Wiring Pinout

Analog Input Channel	Function	DAQ Slot Number	Pin Number
0	Accelerometer Signal 1	0	68
1	Accelerometer Signal 2	0	33
2	Accelerometer Signal 3	0	65
3	Accelerometer Signal 4	0	30
16	Force Gauge Signal 1	1	68
17	Force Gauge Signal 2	1	33
18	Force Gauge Signal 3	1	65
19	Force Gauge Signal 4	1	30
Encoder Input Channel	Function	DAQ Slot Number	Pin Number
0	Encoder Signal 1 (Channel A)	0	37
0	Encoder Signal 1 (Channel B)	0	45
0	Encoder Signal 1 (Return)	0	3
1	Encoder Signal 2 (Channel A)	0	42
1	Encoder Signal 2 (Channel B)	0	46
1	Encoder Signal 2 (Return)	0	41
Analog Output Channel	Function	DAQ Slot Number	Pin Number
0	Motor Output 1	0	22
1	Motor Output 2	0	21
2	Motor Output 3	1	22
3	Motor Output 4	1	21

Table B.3: R^2 Values for Actuator 1 calibration. Individual fits and averaged fits.

	Individual Fits			Averaged Fits		
Input Signal Amplitude	1Hz	5Hz	10Hz	1Hz	5Hz	10Hz
0.5V	0.650	0.646	0.635	0.626	0.635	0.629
1.0V	0.940	0.943	0.941	0.940	0.937	0.930
1.5V	0.958	0.974	0.973	0.958	0.974	0.971
2.0V	0.968	0.980	0.981	0.964	0.980	0.977
2.5V	0.974	0.983	0.984	0.967	0.983	0.983
3.0V	0.979	0.986	0.987	0.966	0.982	0.985
3.5V	0.986	0.990	0.990	0.974	0.984	0.985
4.0V	0.990	0.993	0.992	0.981	0.988	0.988
4.5V	0.993	0.995	0.994	0.991	0.991	0.991
5.0V	0.995	0.996	0.996	0.992	0.994	0.993

Table B.4: R^2 Values for Actuator 2 calibration. Individual fits and averaged fits.

	Individual Fits			Averaged Fits		
Input Signal Amplitude	1Hz	5Hz	10Hz	1Hz	5Hz	10Hz
0.5V	0.790	0.758	0.783	0.783	0.758	0.781
1.0V	0.946	0.956	0.953	0.946	0.940	0.925
1.5V	0.970	0.982	0.981	0.960	0.966	0.970
2.0V	0.975	0.984	0.984	0.973	0.984	0.984
2.5V	0.980	0.987	0.987	0.977	0.986	0.986
3.0V	0.983	0.990	0.990	0.976	0.985	0.985
3.5V	0.987	0.991	0.991	0.977	0.984	0.983
4.0V	0.990	0.993	0.993	0.984	0.986	0.985
4.5V	0.993	0.994	0.994	0.986	0.989	0.988
5.0V	0.995	0.995	0.994	0.991	0.992	0.991

Table B.5: R^2 Values for Actuator 3 calibration. Individual fits and averaged fits.

	Individual Fits			Averaged Fits		
Input Signal Amplitude	1Hz	5Hz	10Hz	1Hz	5Hz	10Hz
0.5V	0.732	0.914	0.909	0.690	0.908	0.908
1.0V	0.975	0.985	0.984	0.964	0.977	0.978
1.5V	0.989	0.991	0.991	0.975	0.981	0.983
2.0V	0.994	0.995	0.995	0.987	0.989	0.988
2.5V	0.996	0.996	0.996	0.992	0.992	0.992
3.0V	0.997	0.997	0.997	0.995	0.995	0.995
3.5V	0.998	0.998	0.997	0.997	0.997	0.996
4.0V	0.998	0.998	0.998	0.998	0.998	0.998
4.5V	0.998	0.998	0.998	0.998	0.998	0.998
5.0V	0.999	0.999	0.998	0.999	0.999	0.998

Table B.6: R^2 Values for Actuator 4 calibration. Individual fits and averaged fits.

	Individual Fits			Averaged Fits		
Input Signal Amplitude	1Hz	5Hz	10Hz	1Hz	5Hz	10Hz
0.5V	0.704	0.687	0.652	0.680	0.683	0.651
1.0V	0.942	0.965	0.963	0.939	0.965	0.963
1.5V	0.967	0.981	0.980	0.961	0.980	0.980
2.0V	0.980	0.987	0.986	0.969	0.981	0.983
2.5V	0.987	0.990	0.990	0.975	0.981	0.981
3.0V	0.991	0.994	0.993	0.982	0.985	0.984
3.5V	0.993	0.995	0.994	0.985	0.987	0.987
4.0V	0.995	0.995	0.995	0.989	0.990	0.990
4.5V	0.996	0.996	0.996	0.991	0.992	0.992
5.0V	0.996	0.997	0.996	0.993	0.994	0.993

Table B.7: Frequency Weighted H_∞ Norms (dB) for Two Mode Controller Designs (Symmetric Sine Burst Results)

	2-6Hz				2-16Hz				2-35Hz			
CFG	OL	LQG	LQGF	MS	OL	LQG	LQGF	MS	OL	LQG	LQGF	MS
0	37.31	35.63	32.67	31.57	41.30	47.28	43.67	41.41	59.94	81.03	60.02	61.22
1	26.13	28.53	26.02	20.69	42.04	42.96	41.99	42.32	54.40	59.07	55.29	54.55
2	27.92	25.78	28.55	27.97	47.26	49.76	49.23	47.74	51.83	59.56	55.44	52.70
3	26.71	24.77	26.79	19.14	45.49	49.27	47.49	45.34	52.05	61.52	54.82	53.88
4	26.88	33.91	27.41	19.80	42.72	45.69	45.96	42.45	54.16	74.81	58.86	55.28
5	19.99	22.21	22.38	16.76	40.49	46.82	41.72	41.14	53.11	55.66	53.81	53.62
6	34.40	36.10	31.49	29.42	45.53	47.16	47.44	44.85	53.77	69.58	55.37	54.85

Table B.8: Frequency Weighted H_∞ Norms (dB) for Two Mode Controller Designs (Asymmetric Sine Burst Results)

	2-6Hz				2-16Hz				2-35Hz			
CFG	OL	LQG	LQGF	MS	OL	LQG	LQGF	MS	OL	LQG	LQGF	MS
0	33.21	38.73	33.02	30.61	41.31	46.34	43.11	41.99	60.24	83.27	60.28	59.68
1	28.29	27.51	26.51	25.16	41.79	43.34	42.26	42.56	54.27	59.21	55.31	54.67
2	29.03	25.71	27.55	23.63	47.65	49.05	49.04	46.62	53.02	57.17	53.70	52.88
3	27.95	23.97	24.04	19.80	45.39	49.03	46.80	44.93	53.57	63.34	56.01	53.83
4	26.21	34.92	27.34	21.07	42.31	46.37	45.96	42.19	54.14	75.45	57.81	55.62
5	23.38	23.48	21.92	19.93	40.42	45.80	41.40	41.36	52.51	55.66	54.13	53.30
6	31.48	33.49	29.94	28.79	45.22	46.87	46.74	44.63	52.65	73.08	56.42	54.45

Table B.9: Frequency Weighted H_∞ Norms (dB) for Four Mode Controller Designs (Symmetric Sine Burst Results, Nominal Only)

	2-6Hz				2-16Hz				2-35Hz			
CFG	OL	LQG	LQGF	MS	OL	LQG	LQGF	MS	OL	LQG	LQGF	MS
0	37.31	30.67	32.50	47.84	41.30	40.78	41.86	47.84	59.94	59.49	61.34	58.48

Table B.10: Frequency Weighted H_∞ Norms (dB) for Four Mode Controller Designs (Asymmetric Sine Burst Results, Nominal Only)

	2-6Hz				2-16Hz				2-35Hz			
CFG	OL	LQG	LQGF	MS	OL	LQG	LQGF	MS	OL	LQG	LQGF	MS
0	33.21	30.50	32.88	47.52	41.31	40.56	42.20	47.52	60.24	59.51	61.27	57.11

Appendix C

Additional Derivations

C.1 Matrix Formulation for Modal Uncertainty Transfer Function

Beginning with equation 3.17, we can form an alternate derivation of Q which explicitly utilizes the diagonal nature of the modal components to create a matrix operation which expresses the modal components of the input to output channel tranfer function as a vector. We start by defining two additional diagonal matrices and a vector of ones.

$$[\bar{U}_r] = \begin{pmatrix} U_1 & 0 & \dots & 0 \\ 0 & U_2 & & 0 \\ \vdots & & \ddots & \vdots \\ 0 & 0 & \dots & U_r \end{pmatrix}$$

$$[\bar{V}_{i,r}] = \begin{pmatrix} v_{i,1} & 0 & \dots & 0 \\ 0 & v_{i,2} & & 0 \\ \vdots & & \ddots & \vdots \\ 0 & 0 & \dots & v_{i,r} \end{pmatrix}$$

$$[\bar{V}_{r,j}] = \begin{pmatrix} v_{1,j} & 0 & \dots & 0 \\ 0 & v_{2,j} & & 0 \\ \vdots & & \ddots & \vdots \\ 0 & 0 & \dots & v_{r,j} \end{pmatrix}$$

$$O = \begin{pmatrix} 1 \\ 1 \\ \vdots \\ 1 \end{pmatrix}$$

With these defined, we can define a vector of the modal components of a transfer function channel then apply the Woodbury Matrix Identity. We know that each matrix is diagonal and therefore invertible.

$$\begin{aligned}
P_{i,j} &= O^* \Bigg(([\bar{V}_{i,r}][\bar{V}_{r,j}] \cdot I \cdot s^2)((I \cdot s^2 + 2[\bar{Z}_r][\bar{\Omega}_r] + [\bar{\Omega}_r^2])... \\
&+ [\bar{U}_r](2[\bar{Z}_r][\bar{\Omega}_r] + 2[\bar{\Omega}_r^2])(I \cdot \delta))^{-1} \Bigg) O \\
&= O^* \left(A(C + UDV)^{-1} \right) O \\
&= O^* \left(A(C^{-1} - C^{-1}U(D^{-1} + VC^{-1}U)^{-1}VC^{-1}) \right) O \\
&= O^* \left(AC^{-1} - AC^{-1}U(D^{-1} + VC^{-1}U)^{-1}VC^{-1} \right) O \\
&= O^* \left(AC^{-1} - AC^{-1}UD(I + DVC^{-1}U)^{-1}VC^{-1} \right) O \\
&= O^*(([\bar{V}_{i,r}][\bar{V}_{r,j}] \cdot I \cdot s^2)(I \cdot s^2 + 2[\bar{Z}_r][\bar{\Omega}_r] + [\bar{\Omega}_r^2])^{-1} - ([\bar{V}_{i,j,r}] \cdot I \cdot s^2)(I \cdot s^2... \\
&+ 2[\bar{Z}_r][\bar{\Omega}_r] + [\bar{\Omega}_r^2])^{-1}[\bar{U}_r](2[\bar{Z}_r][\bar{\Omega}_r] + 2[\bar{\Omega}_r^2]) \Bigg(I + (2[\bar{Z}_r][\bar{\Omega}_r] + 2[\bar{\Omega}_r^2])(I \cdot \delta)(I \cdot s^2... \\
&+ 2[\bar{Z}_r][\bar{\Omega}_r] + [\bar{\Omega}_r^2])^{-1}[\bar{U}_r] \Bigg)^{-1} (I \cdot \delta)(I \cdot s^2 + 2[\bar{Z}_r][\bar{\Omega}_r] + [\bar{\Omega}_r^2])^{-1} O
\end{aligned}$$

Observing the above result and comparing with equation 3.18, we can explicitly define the Q quadrant matrices per input to output channel.

$$Q_{11} = (2[\bar{Z}_r][\bar{\Omega}_r] + [\bar{\Omega}_r^2])(I \cdot s^2 + 2[\bar{Z}_r][\bar{\Omega}_r] + [\bar{\Omega}_r^2])^{-1}[\bar{U}_r]$$

$$Q_{12}^i = \left((I \cdot s^2 + 2[\bar{Z}_r][\bar{\Omega}_r] + [\bar{\Omega}_r^2])^{-1} \cdot [\bar{V}_{r,j}]\right) O$$

$$Q_{21}^j = O^* \left(-([\bar{V}_{r,j}] \cdot I \cdot s^2)(I \cdot s^2 + 2[\bar{Z}_r][\bar{\Omega}_r] + [\bar{\Omega}_r^2])^{-1}[\bar{U}_r](2[\bar{Z}_r][\bar{\Omega}_r] + [\bar{\Omega}_r^2])\right)$$

$$Q_{22}^{i,j} = O^* \left(([\bar{V}_{r,j}] \cdot I \cdot s^2)(I \cdot s^2 + 2[\bar{Z}_r][\bar{\Omega}_r] + [\bar{\Omega}_r^2)^{-1} \cdot [\bar{V}_{i,r}]\right) O$$

Bibliography

[1] Analog Devices. *Dual Axis Accelerometer Evaluation Board*, 2004. Rev. 0.

[2] Analog Devices. *Precision ±1.7 g, ±5 g, ±18 g Single-/Dual-Axis iMEMS® Accelerometer*, 2018. Rev. F.

[3] Artesyn Embedded Technologies. *LCC600 Data Sheet*, March 2018.

[4] ATA Engineering, San Diego, CA. *IMAT, a suite of utilities for sharing data between MATLAB, analysis tools, and test software, Ver. 6.1.*, March 2016.

[5] K. Y. Billah and R. H. Scanlan. Resonance, tacoma narrows bridge failure, and undergraduate physics textbooks. *American Journal of Physics*, 1991.

[6] C. Briggs. Design and implementation of a flutter suppression experiment. *AIAA Atmospheric Flight Mechanics Conference, AIAA AVIATION Forum*, 2017.

[7] C. Briggs, D. C. Kammer, A. White, and D. Schwartz. Integration of structural uncertainty and robust control. *58th AIAA/ASCE/AHS/ASC Structures, Structural Dynamics, and Materials Conference*, 2017.

[8] R. W. Bunton and C. M. Denegri. Limit cycle oscillation characteristics of fighter aircraft. *Journal of Aircraft*, 37(5), 2000.

[9] Copley Controls Corp. *Models 412CE, 413CE, 421CE, 422CE, DC Brush Servo Amplifiers*.

[10] H. J. Cunningham, H. T. Batina, and R. M. Bennett. Modern wing flutter analysis by computational fluid dynamics methods. *Journal of Aircraft*, 25, 1988. No. 10.

[11] R. A. de Callafon, D. N. Miller, J. Zeng, and M. J. Brenner. Step-based experiment design and system identification for aeroelastic dynamic modeling. *AIAA Atmospheric Flight Mechanics Conference*, 2009.

[12] M. J. Dillsaver, C. E. S. Cesnik, and I. V. Kolmanovsky. Trajectory control of very flexible aircraft with gust disturbance. *AIAA Atmospheric Flight Mechanics (AFM) Conference*, 2013.

[13] J. Doyle, B. Francis, and A. Tannenbaum. *Feedback Control Theory*. MacMillan Publishing Company, 1990.

[14] J. C. Doyle, K. Glover, P. P. Khargonekar, and B. A. Francis. State-space solutions to standard h_2 and h_{infty} control problems. *IEEE Transactions on Automatic Control*, 1989.

[15] J. C. Doyle, A. Packard, and K. Zhou. Review of lfts, lmis, and μ. *Proceedings of the 30th Conference on Decision and Control*, 1991.

[16] D. J. Ewins. *Modal Testing: theory, practice and application.* Research Studies Press LTD, London, 2000.

[17] F. Fonte, S. Ricci, and P. Mantegazza. Gust load alleviation for a regional aircraft through a static output feedback. *Journal of Aircraft, Vol. 52, No. 5*, 2015.

[18] D. Göge, P. Lubrina, M. Böswald, and U. Füllekrug. Ground vibration testing of large aircraft - state-of-the-art and future perspectives. 2007.

[19] M. Green and D. J. N. Limebeer. *Linear Robust Control.* Prentice Hall, 1995.

[20] J. W. Helton and O. Merino. *Classical Control Using H-Infinity Methods: An Introduction to Design.* Society for Industrial and Applied Mathematics, 3600 University City Science Center, Philadelphia, PA 19104-2688, 1998.

[21] J. P. Hespanha. *Linear Systems Theory.* Princeton University Press, 41 William Street, Princeton, NJ 08540, 2009.

[22] Hewlett Packard. *HP E1432A 16 Channel 51.2 kSa/s Digitizer plus DSP User's Guide.*

[23] J. R. Hooker, A. W. Burner, and R. Valla. Static aeroelastic analysis of transonic wind tunnel models using finite element methods. *NASA Langley Research Center*, 1997.

[24] S. P. L. M. S. Inc. *Basic Dynamic Analysis User's Guide.*, 2016.

[25] S. P. L. M. S. Inc. *NX NASTRAN User's Guide.*, 2016.

[26] Interface. *Model WMC Miniature Sealed Stainless Steel Load Cell Capacities 5-500 lbf (22-2200N)*, April 2012.

[27] R. E. Kalman. A new approach to linear filtering and prediction problems. *ASME Transactions Journal of Basic Engineering*, 1960.

[28] J. Kautsky, N. K. Nichols, and P. Van Dooren. Robust pole assignment in linear state feedback. *International Journal of Control*, 41, 1985. No. 5.

[29] E. M. Kraft. After 40 years why hasn't the computer replaced the wind tunnel? *ITEA Journal*, 2010.

[30] H. Kwakernaak. Mixed sensitivity design. *15th Triennial World Congress*, 2002.

[31] N. A. J. Lieven, D. J. Ewins, N. M. M. Maia, and J. M. M. Silva. Modal analysis identification techniques. *Philosophical Transactions of the Royal Society of London. Series A: Mathematical, Physical and Engineering Sciences*, 2001.

[32] R. Lind and M. Brenner. Robust flutter margins of an f/a-18 aircraft from aeroelastic flight data. *Journal of Guidance, Control, and Dynamics*, 1997.

[33] L. Ljung. *System Identification: Theory for the User*. Prentice-Hall, Inc., Englewood Cliffs, NJ 07632, 1987.

[34] L. Ljung. *System Identification Toolbox for use with MATLAB*, January 2011.

[35] Moticont. *Linear Direct Drive Motor With Built-In Encoder*. Rev. 2.

[36] National Instruments. *DAQ M Series: M Series User Manual NI 622x, NI 625x, and NI 628x Multifunction I/O Modules and Devices*, 7 2016. Rev. 01.

[37] National Instruments. *Device Specifications NI 6229 M Series Data Acquisition: 16-Bit, 250 kS/s, 32 AI, 48 DIO, 4 AO*, June 2016. Rev. 01.

[38] PCB Piezotronics. *Model 208C03 ICP® Force Sensor Installation and Operating Manual*. Rev. G.

[39] PCB Piezotronics. *Series 440 Modular Signal Conditioners*.

[40] PCB Piezotronics. *ICP® Force Sensor*, 2016. Rev. J.

[41] Rigol. *Quick Guide: DS1000E, DS1000D Series Digital Oscilloscope*, June 2013.

[42] Rigol. *Data Sheet: DS1000E, DS1000D Series Digital Oscilloscope*, December 2015.

[43] J. J. Ryan, J. T. Bosworth, and J. J. Burken. Current and future research in active control of lightweight, flexible structures using the x-56 aircraft. *52nd Aerospace Sciences Meeting, AIAA SciTech Forum*, 2014.

[44] Schaffner. *Multi-stage Performance AC/DC EMI Filter*, 2017.

[45] D. K. Schmidt. Stability augmentation and active flutter suppression of a flexible flying-wing drone. *Journal of Guidance, Control, and Dynamics*, 39(6):409–422, 2016.

[46] I. The Mathworks. *Simulink Realtime User's Guide.*, 2018.

[47] J. Theis, H. Pfifer, and P. Seiler. Robust control design for active flutter suppression. *IAA Atmospheric Flight Mechanics Conference*, 2016.

[48] G. Zames and B. Francis. Feedback, minimax sensitivity, and optimal robustness. *IEEE Transactions on Automatic Control*, 1983.

[49] J. Zeng, R. A. de Callafon, and M. J. Brenner. Suppression of the aeroelastic/aeroservoelastic interaction using adaptive feedback control instead of notching fitlers. *AIAA Atmospheric Flight Mechanics Conference*, 2011.